

The Journal of Refractory Innovations

# bulletin

2020

16 Customized  
Refractory Solutions

42 Refractory Tubes With  
Innovative Liner Technology

50 Vibrational Determination  
of Gas Purging



RHI MAGNESITA



## Bulletin

The Journal of Refractory Innovations

2020

<b>Published by</b>	RHI Magnesita GmbH, Vienna, Austria
<b>Chief Editor</b>	Gerald Gelbmann
<b>Executive Editors</b>	Thomas Drnek, Christoph Eglsäer, Mateus Vargas Garzon, Thomas Mathew, Felipe Nonaka, Ravikumar Periyasamy, Diane Taylor, Heinz Telser, Karl-Michael Zettl
<b>Raw Materials Expert</b>	David Wappel
<b>Lingual Proofreader</b>	Barbara Wrathall-Pohl
<b>Technical Writers</b>	Sandra Königshofer, Clare McFarlane
<b>Proofreaders</b>	Michaela Hall, Sandra Königshofer, Clare McFarlane
<b>Project Manager</b>	Michaela Hall
<b>Photography, Graphics and Production</b>	Susanne Steinberger-Steinrisser
<b>Design and Typesetting</b>	Universal Druckerei GmbH, Leoben, Austria

**Contact** Michaela Hall  
RHI Magnesita GmbH, Technology Center  
Magnesitstrasse 2  
8700 Leoben, Austria

**E-mail** [bulletin@rhimaginesita.com](mailto:bulletin@rhimaginesita.com)

**Phone** +43 50213 5300

**Website** [rhimaginesita.com](http://rhimaginesita.com)

The products, processes, technologies, or tradenames in the Bulletin may be the subject of intellectual property rights held by RHI Magnesita N.V., its affiliates, or other companies.

The texts, photographs and graphic design contained in this publication are protected by copyright. Unless indicated otherwise, the related rights of use, especially the rights of reproduction, dissemination, provision and editing, are held exclusively by RHI Magnesita N.V. Usage of this publication shall only be permitted for personal information purposes. Any type of use going beyond that, especially reproduction, editing, other usage or commercial use is subject to explicit prior written approval by RHI Magnesita N.V.

**Cover picture:** The cover illustration shows a swarm of gas bubbles released from a hybrid plug migrating upwards through the water during water model investigations at RHI Magnesita's water modelling facility. Bubble size and size distribution as well as flow patterns and phenomena, like for example back-attack, are studied by different methods in order to develop purging plugs with enhanced properties for applications in steel and nonferrous metal metallurgy.

# RHI Magnesita Worldwide news

## Worldwide

### Spinosphere Technology Completes First Year of Installation and Patent Application Published

February 2020 represented a remarkable milestone for the Business Unit Cement & Lime because the first year of full campaigns with ANKRAL RX installations were completed and the patent application for RHI Magnesita's Spinosphere Technology was published. After the go-to-market in 2018, results of the first installations at several customers' sites could be seen during last winter's repairs. The ANKRAL RX bricks were installed in critical kiln zones, side by side with competitors' high-grade brands. Now having this comparison available, RHI Magnesita can proudly announce that the X-Series bricks performed exceptionally well. Therefore, the X-Series portfolio has been extended to cover the full product range with this innovative technology. The positive customer feedback and additional actions will push sales further. Currently, more than 4000 tonnes of orders are in hand for 2020 and this number will increase significantly. The journey also includes bringing the X-Series to all our production facilities.

## Europe

### Successful Transfer of ISO Products for Voestalpine Stahl Linz

In 2019, when RHI Magnesita decided to transfer the ISO production from Trieben (Austria) to Bonnybridge (Scotland), voestalpine Stahl Linz (Austria) was completely affected because all the isostatically pressed products were produced in Trieben. Although voestalpine Stahl Linz expressed doubts after this announcement, Sales and Technical Marketing convinced the customer to run pretrials and accredit the products from Bonnybridge. The five affected patterns were delivered in June 2019 and trials were carried out without any issues in July 2019, resulting in voestalpine Stahl Linz approving the Bonnybridge plant and a complete production switch by October/November 2019. Due to the good results, voestalpine Stahl Linz asked RHI Magnesita to prepare trials with SHP 2.0 and 2.1 stoppers from Bonnybridge at the beginning of 2020. The trial pieces were delivered at the end of February 2020 and the trials will take place as soon as possible. In the case of successful results, voestalpine Stahl Linz has already announced further trials with monotubes for CC4 caster, leading to potential new monthly business.

## Europe

### DELTEK A115 Trial Success in Poland

RHI Magnesita supplies numerous flow control materials to customers in Poland, including complete tundish linings as well as isostatically pressed materials such as ladle shrouds, stoppers, and submerged shrouds. At the end of last year, RHI Magnesita proposed a new tundish nozzle design, introducing a new isostatically pressed alumina main body material—DELTEK A115. The DELTEK A115 material was developed to provide a higher thermal shock resistance during poor preheat applications, while maintaining or even exceeding the expected wear resistance of the existing DELTEK alumina materials' portfolio. To date, the ongoing industrial trials in Poland have shown outstanding results, excellent thermal cycling, and an extremely low wear in the casting channel, which guarantees a safe casting process and high-quality steel for RHI Magnesita's customers.

# RHI Magnesita Worldwide news (continued)

## Europe

### Monotube Trials in TATA Port Talbot

During September 2019, RHI Magnesita supplied 50 monotubes to TATA Port Talbot (UK) for trial. The initial statement from the customer suggested, if the trials were successful, other isostatically pressed refractory products would be open for trials. Currently, TATA Port Talbot has two suppliers for monotubes, one for a preheated version and another for emergency cold start applications. The DELTEK D99N FREEFLOW design, supplied for trial, has the capability to satisfy both situations. During November 2019, all 50 trial monotubes showed a slag line wear rate that was comparable or better than the competition. As the Venturi preheat for the monotube doesn't exceed 700 °C, TATA also experiences occasional thermal shock incidents. However, thanks to the FREEFLOW bore, the RHI Magnesita products all showed excellent performance at start up. The TATA operators and staff who were internally following the trials commented on the exceptional initial trial performance of the products. Following this successful result, the customer has ordered additional monotubes for an industrial trial planned in 2020.

## China

### Bayuquan Plant Installs Industrial Robot

Aligning with RHI Magnesita's strategy to increase the automation and digitalization level, as well as reduce high labour costs and solve manpower shortage problems, the Bayuquan plant (China) took the step to install the first industrial robot in December 2019. The project will deliver manufacturing cost savings by reducing the labour costs and the payback period is approximately three years. In addition, success of the first robot will provide a learning experience and build the foundation for rolling out, step by step, automation and digitalization in the entire plant.

## USA

### Great Efficiency Boost With RHI Magnesita Gas Purging System Solution

Exchanging an existing plug closing system with RHI Magnesita's state-of-the-art SOC-H gas purging system solution has resulted in considerable improvements in gas purging efficiency. After deciding to convert the ladles to RHI Magnesita's SOC-H system, the customer in Alabama (USA) moved away from hot plug changes during operation. The new plug-block assemblies are installed together with the initial wear lining and at about halfway through the campaign when the slag line bricks are replaced. During this repair, the plug-block assemblies are changed to finish the ladle campaign without any hot plug changes necessary. The customer uses RHI Magnesita hybrid plugs and set assemblies with the double coating technology from RHI Magnesita's Urmitz plant (Germany).

## Europe

### First Cost per Saving Contract Signed for the BOF at AM Gijon

A higher level of product sophistication, (e.g., clean steel, interstitial-free, and ultra-low carbon steel grades), tighter restrictions on CO<sub>2</sub> emissions, unstable charging materials, and balanced agent/material sourcing require an optimized BOF process operation with an efficient bottom purging system. After signing the first cost per production (CPP) contract for BOFs within the Arcelor Mittal group

on the European market in January 2019, at Arcelor Mittal Gijon (Spain), the new business solution model—cost per saving (CPS)—was signed on 26 February 2020. With this, RHI Magnesita brings to the customer new and optimized refractory concepts, process improvements, tailor-made maintenance procedures, and the installation of the CIP—converter inert gas purging system.

The new CPS business model is focused on a win-win approach for customer and supplier, aiming for optimization of metallurgical, economic, and environmental process parameters. The obtained CO<sub>2</sub> emission savings and the associated increase in BOF process performance can further reduce the total cost of ownership (TCO) situation in addition to implementing tailor-made refractory concepts at the customer site. The CPS relates to defined key performance indicators (KPIs) such as yield, O<sub>2</sub> consumption, deoxidation agent consumption, phosphorus level, and reblowing rate. These KPIs are then quantified in a cost per tonne matrix and multiplied by the individual consumption per heat. The benefits and savings calculations are determined by comparing the existing standard consumptions (prior to CPP/CPS implementation), with those after implementation of the systems and procedures. After commissioning and coordinated modification actions, a tracking for each heat is initiated and summarized in a savings template on a monthly basis. For the saving verification itself, the aligned KPIs will always be referred to and compared with the last six campaigns using the standard BOF set up. The calculated savings are then shared between the customer and RHI Magnesita, fixed on a certain number of vessel campaigns. Finally, there are no CAPEX and investments required by the customer starting the CPS project with RHI Magnesita.

---

## China

### Successful Steel Business Development in China

With the strategy of being top service and solution provider, the China Steel team has developed a general contract business within the Guangxi Shenglong Project, which is the first “Ladle to Mould” package for the Business Unit China regarding quality steelmaking. The areas of health, safety, and environment, as well as refractory recycling are also deeply embedded in this project. This starts the new wave of developing RHI Magnesita in Southwest China where the steel industry is growing rapidly, not only in capacity but also regarding quality. It is a breakthrough on the Chinese Steel market and the start for RHI Magnesita to become a larger player in

this region. China’s newly expanded Steel team acted cross functionally with full passion and finally set a milestone for our group after months of hard work. Immediately after, the team successfully built a strategic, cooperative relationship and established a commercial contract with Guilin Pinggang Iron and Steel, who has the first Primetals EAF Quantum in China (the third one in the world) supported by the Italian Danieli high-tension production line of headless continuous casting and strapping rods, which takes less than 15 minutes from molten steel to finished product. Pinggang has contracted the entire line from EAF to mould to RHI Magnesita, including all the refractory materials, equipment, maintenance, and manpower. As a leader in the refractory industry, RHI Magnesita has provided Pinggang with in-depth experience and top technology in cooperation with TYASA, the world’s first EAF Quantum in Asia, and GPH Ispat, thereby making Pinggang a “technology aircraft carrier” in the industry.

---

## China

### Digitalization Hub in Shanghai

A digitalization Hub has been established in Shanghai (China) to enable RHI Magnesita achieve digital transformation. It will be supported by the booming artificial intelligence and Industry 4.0 technology in the region, as well as the talents gathered by Zhangjiang Artificial Intelligence Island, and through having technical support from our neighbours Microsoft, IBM, and Ali.

---

## China

### First 1:1 Scale Water Model for RHI Magnesita Built in Dalian

On 3 December 2019, RHI Magnesita’s first 1:1 scale water model facility was opened in Dalian (China). The project was designed to build a simulation platform for metallurgical processes by using actual products manufactured in the ISO Plant Dalian (IPD). It enables the flow behaviour of molten steel induced by the isostatically pressed ceramics to be evaluated, which is extremely beneficial for customers and product development. To date, the first water modelling experiment has been conducted for Angang Steel (China) and there are three other steel customers lined up. The water model will improve both customer service and product design.

# RHI Magnesita Worldwide news (continued)

---

## Worldwide

### INNOREG Successfully Started

Glass furnace regenerators are used to recover energy from combustion gases generated during furnace firing. In the past many factors were considered to maximize efficiency of this process and the optimized solution was applied to all regenerators equivalently. Three years ago, RHI Magnesita looked at the subject again and found that even better results could be achieved by adapting the regenerators to each individual customer. Thereby, new, additional checker brick formats with specific properties were developed to enable such tailor-made solutions. This new concept of customized regenerators was presented to the market, at the 2018 glasstec trade fair, under the name INNOREG.

The regenerator optimization focuses on two main topics. The first is increasing energy efficiency and here the newly developed TLW format, with an enlarged specific heat exchange surface, enables an improvement of up to 1%. For an average container glass furnace, this means an annual natural gas saving of around 90000 m<sup>3</sup>, which is associated with a CO<sub>2</sub> emission reduction of approximately 85000 m<sup>3</sup>. The second issue is regenerator clogging, where components of the exhaust gases can condense in the colder regenerator zones. They then accumulate on the checker bricks and can clog

the regenerator, so that its function is reduced, sometimes significantly. This is where the newly developed LCP format can help, with a larger channel width preventing clogging and making it easier to clean the regenerators. The wide INNOREG portfolio of the established and new checker shapes now enables individual regenerator optimization, considering the specific glass furnace functional parameters. However, it is not only the format selection that is optimized when the regenerators are individually adapted. The INNOREG concept also includes a material selection of the regenerator walls and the checker bricks, adapted to the thermal, mechanical, and chemical load in the different zones. Here, RHI Magnesita can rely on a broad portfolio of basic and nonbasic materials. After the usual start-up phase in the project business, three furnaces with the new formats were delivered in 2019 and this year at least 11 projects will be delivered. We see this as the beginning of a great success story.

---

## Oman

### Multiple Lifetime Records at Jindal Shadeed Iron & Steel LLC

Jindal Shadeed Iron & Steel LLC (JSIS) and RHI Magnesita continue the successful cooperation established in 2016 with the renewal of a five-year Full Line Service (FLS) contract in April 2019. RHI Magnesita exclusively supplies all technology, refractories, and services needed to produce 2.4 million tonnes of steel per year, namely products, machinery, logistics, and installation services along the entire customer value chain. JSIS and RHI Magnesita closely cooperate, with mutual benefit, as the following success stories clearly demonstrate.

The first is an EAF roof lifetime record where both the continuous R&D efforts and permanent trials at the customer led to significant improvements in the roof service life. In December 2019, testing of an improved prefabricated roof was completed and showed that newly developed sol-bonded, high-alumina monolithics, provide both the highest abrasion and thermal shock resistance. As a result, the service life increased from an average of 720 heats to a RHI Magnesita all-time record of 2095 heats (+290%). Further improvements of this result are already underway and will be tested soon.

A record was also achieved for the closed casting sequence duration on one of the two 8-strand combi caster machines where 37 consecutive heats were close cast, resulting in a liquid steel output of 7836 tonnes over 30 hours, with 100% strand availability. This was mainly possible due continuous improvements of the isostatically pressed products together with very stable casting conditions.

Additional records include the longest open cast sequence length of 71 heats (over 55 hours) and, in August 2020, the highest ever average ladle life in a month of 125 heats. It is interesting to note that this average ladle life is the highest ever in the history of JSIS, since the inception of the plant, and was achieved with a doloma barrel for both Al-killed and Si-killed steel (approximately 29% vacuum degasser treatment), which is fairly unique. RHI Magnesita is very grateful for the close collaboration with Jindal Shadedee, the trust, and the opportunity to be a long-term partner, as it provides the basis for continuous improvement.

### Russia

## One-year Successful Operation With INTERSTOP CIP Technology at Severstal (Cherepovets)

Severstal is one of the leading steel producers and has been continuously upgrading the production facilities along the process chain. In 2018 the decision was made to upgrade the existing three basic oxygen furnaces (BOF) with RHI Magnesita INTERSTOP converter inert gas purging (CIP) technology. The contract to implement the complete CIP technology package, together with the installation of eight multi hole plugs (MHP) and the whole BOF lining from RHI Magnesita was signed in September 2018. The first hot test at BOF No. 3 followed only two months later, in November 2018. The performance tests for all three BOFs were finished in May 2019, nine months later from signing the contract. The final acceptance certificate (FAC) was received in November 2019.

Besides the fast project realization, the metallurgical results are remarkable and have been achieved in two major steps. With the implementation of this system the customer's performance indicators have been improved, which was specified in the FAC. Three key performance indicators (KPI) show the performance improvement. Thus, oxygen activity has been reduced by 13%, the [C]x[O] product content by 24%, and FeO content by 17%.

Good results have been achieved by combining the customer's current processes with the CIP technology and by prior evaluation, analysis, and fine tuning of both the technology in use and the customer's processes. Finally, after about one-year operation with CIP oxygen activity has been reduced by 21%, the [C]x[O] product content by 29%, and FeO content by 21%. Due to these improvements the steel yield has been already increased from the very beginning of the project implementation. MHP which were continuously monitored, demonstrated high availability; their lifetime reached 4500 heats and show potential for even more.

This remarkable success story was only possible due to the extraordinary cooperation of all parties in this project, namely Severstal, NSK, and RHI Magnesita.

We would like to thank all personnel and management of the companies for the support during the project implementation, commissioning, and further continuous improvement.

### Worldwide

## New Plug Function Device Supports Standardized and Controlled Ladle Purging Plug Cleaning

In a modern steelmaking facility, high initial opening rates as well as a long service life of the ladle purging ceramics are important prerequisites for an efficient and stable production. These two parameters can optimally be influenced by a correctly performed purging plug service. The newly developed Plug Function Device (PFD) supports the operators at the ladle maintenance stand, in correctly performing plug cleaning by using the oxygen lance to the minimum required and maximum necessary extent. Using the PFD, reliable and reproducible results are achieved.

To properly carry out purging plug cleaning, an appropriate backpressure must be applied to the plug to be cleaned, in order to prevent infiltration of the purging plug channels. The plug test mode provides information if the purging plug has a sufficient flow rate for the next heat or if it is closed and has to be cleaned with the oxygen lance. For this purpose, compressed air or nitrogen is applied to the plug via the PFD. By using a different test mode, it is also possible to check the gas tightness of ladle pipework during maintenance. A gas-tight ladle piping is a prerequisite for successful gas purging and will directly result in cash savings by reducing purging medium loss.

After several successful field trials at customers in Asia, Europe, and the Near-Middle East, more than 10 PFDs have already been commissioned and beneficially integrated into the onsite purging plug maintenance procedure. Clear, measurement-based determination of the current condition of the plug and a record of all relevant data is leading to reproducible plug maintenance and thereby an increased work and operational safety. All customers have directly seen advantages in increased initial purging plug opening rates and lifetimes when the plug maintenance was carried out correctly with the support of PFD.

# RHI Magnesita Worldwide news (continued)

## Europe

### RHI Magnesita Establishes Digital Hub for 4.0 Projects

RHI Magnesita kick-started the 4<sup>th</sup> revolution of the refractories industry in February 2020. Thanks to intensive basic research and global, interdisciplinary development work, RHI Magnesita successfully developed the first systems for data-based process optimization at temperatures of 1200 °C and higher. The Digital Hub, which was established specifically for this purpose, will bring these concepts to market readiness. The company's three 4.0 initiatives are called Automated Process Optimization (APO), Quick (QCK), and Broadband Spectral Thermometer (BST).

APO receives all available data about the given production process, such as temperature changes, chemical processes, optical measurements, order cycles, and planned maintenance work. Based on this information, empirical values, and previous measurement results, APO uses artificial intelligence to make predictions about how refractory materials should be maintained and when they will have to be replaced. The area of application for APO basically knows no limits. But of course, just like with any data-based simulation, the better the data APO receives as input, the more precise the predictions. Therefore, two of the 4.0 initiatives at the Digital Hub deal with systems that can supply even higher quality input data for APO.

QCK is based on cutting-edge image processing technology and can take precise 3D scans of systems at operating temperature within a few seconds—even at temperatures above 1200 °C—and the measurement doesn't take any longer than snapping a photo. Up until now, laser technology has been used for this purpose, which takes significantly longer and provides a much lower resolution. Additional thermal information can be supplied by BST as it is capable of measuring the temperature continuously and has the potential to eliminate the discrete temperature measurements that are commonly used today. This will make it possible to adjust the temperature of a melt exactly, thereby preventing unnecessary heating.

## Europe

### Dolomite Resource Center Europe: Top Quality From Austria for Europe

RHI Magnesita is investing more than €40 million in the construction of its new Dolomite Resource Center Europe—the company's largest investment in Austria in the past 30 years. In the future, dolomite for the entire European market will be mined and processed at the Hochfilzen site in Tyrol before being transported by rail to sister plants in France. It's no coincidence that RHI Magnesita decided to invest extensively in the Hochfilzen site. A 20-person development team worked tirelessly to find the perfect location for the new Dolomite Resource Center Europe and Hochfilzen was selected due to the outstanding quality of the dolomite there. In order to be able to transfer the raw material for processing and then send it out into the world, it was also decided to invest in a sustainable transportation system.

## India

### Five-Year Total Refractory Management Contract With Tata Steel BSL

Tata Steel BSL Ltd., (India) awarded RHI Magnesita a five-year contract for the basic oxygen furnace (BOF) total refractory management, which includes refractory supply, process equipment, technology, and overall execution related to refractory performance. Situated in Angul, Odisha, and belonging to the Tata Steel Group, this plant is running at 4.4 million tonnes a year, of which 70% is produced through the BOF route.

## Worldwide

### Global Awards' Winners 2019

RHI Magnesita selected its Global Awards' winners for 2019 from a pool of 120 nominees. The Global Awards annually honour innovative and state-of-the-art projects developed by employees. The six finalists presented their projects in the three categories Out-of-the-Box, Sustainability, and Global Project and the winners were subsequently announced in January 2020. The Out-of-the-Box winner was the Golden Dragon project from Wang Lin and his team in China. By creating a cross-functional project team with a bottom-up approach, the team mapped opportunities to achieve significant cost reductions. Norberto Bellandi and his team from Argentina won the Sustainability award with the "Recycling of MGU" project. The team succeeded in making RHI Magnesita's RASA plant indispensable for the market with an unbeatable unique selling point: New magnesia carbon bricks containing up to 60% recycled raw material, where each tonne of recycled material used cuts up to three tonnes of CO<sub>2</sub> emissions. The Global Project Award was handed over to Martin Geith and his Austrian team for the New Coating Technology—Spinosphere project. This patented technology was developed by RHI Magnesita and revolutionized the cement refractory brick market. This new series, called ANKRAL RX, offers new levels of thermal shock resistance.

## India and USA

### Manishri Refractories and MORCO Acquisitions

RHI Magnesita has made two acquisitions—one in 2019 and another in the first half of 2020. One important acquisition was buying a plant from Manishri Refractories & Ceramics Pvt. Ltd., ("Manishri"). The purchased plant fits in with RHI Magnesita's short-term and mid-term growth strategy in India. The plant produces magnesia-carbon bricks, where there is huge potential in the Indian market and before the acquisition RHI Magnesita had no local supply source. This acquisition will help to reach new segments and further expand the footprint in India. The second acquisition was Refractories Co. Inc. (MORCO). The site is strategically located in the Midsouth of the United States, a region that is rapidly growing in importance for RHI Magnesita. It produces over 400 high-quality monolithic mixes, which serve a multitude of industries, including steel, cement, lime, and glass. The employees also have the expertise to provide refractory material for the petrochemical industry.

## India

### EAF Lifetime Record at JSPL Angul

JSPL Angul (India) achieved the highest ever EAF lifetime of 387 heats with RHI Magnesita supplies. There was the potential for approximately 25 more heats, but the furnace had to be closed due to shop logistics. The highest ever sequence in the tundish was also achieved on a single strand slab caster, where all the products were from the Bhiwandi plant (India) except for a tundish back up castable supplied by RHI Magnesita's Clasil plant in India.

## India

### Major Achievements at JSW Salem Steel Plant

RHI Magnesita had two major achievements at JSW Steel Ltd, Salem works (India). One was at the energy optimization furnace (EOF-I) where the highest ever heats of 1080 were achieved, against the guaranteed life of 800 heats. The second was in the 65-tonne steel ladle with the highest life of 150 heats, against a guaranteed life of 100 heats.

## India

### All-Time Lowest Refractory Consumption Figures at Sunflag Iron and Steel Company

**At Sunflag Iron and Steel Company Ltd., (India) RHI Magnesita achieved a straight furnace lifetime of 686 heats that amounted to 38416 tonnes of liquid steel (tls), without any intermittent repair and the all-time lowest consumption figures at 0.58 kg/tls for bricks and 2.5kg/tls for maintenance mixes. It also witnessed the first ever two metal zone ladle brick sets delivered from the Cuttack plant (India) performing on par with RHI Magnesita Chinese supplies. These two ladles were poised at 58 heats when the plant was closed due to the COVID-19 lockdown.**

# RHI Magnesita Worldwide news (continued)

## Europe

### RHI Magnesita Invests in “Digital Flagship Plant Radenthein”

RHI Magnesita is investing a total of €50 million in state-of-the-art infrastructure digitalization in Radenthein (Austria), to make it the most modern plant in the refractory industry. Among other areas, the investment includes new automation processes, process optimization, establishment of new infrastructure for robot units, a wireless LAN system to connect all machines and modern brick presses, as well as a high-performance tunnel kiln and a highly specialized shuttle kiln for customized products. With new technologies and systems, new job profiles are needed. Therefore, RHI Magnesita is also investing in the expansion of the local training facility and supports the Carinthian pilot project “Apprenticeship and Studies”. In doing so, RHI Magnesita secures its market leadership by educating the next generations of innovative, technology-astute employees. Another pilot project that is to be implemented in Radenthein, a first of its kind in the industry, is the Manufacturing Execution System (MES). MES is an intelligent and self-learning control system that is connected to all areas of the plant. Overall, the investments in Radenthein will boost the plant’s production capacity. As a business location, Austria is clearly a strategic decision and will pave the way for a more modern refractory industry in the long run. The Radenthein project will be put into operation by autumn 2021.

## Brazil

### Major Investment to Gear Up Operations in Brumado

RHI Magnesita is investing €30 million in the construction of a new rotary kiln to ramp up vertical integration of the mine in Brumado (Brazil). To be able to offer distinctive value-added products and emerge stronger from the current COVID-19 crisis, RHI Magnesita is committed to pursue its strategic growth plan. With this specific investment, RHI Magnesita will become the most competitive producer of dead burned magnesia in the world. The new state-of-the-art rotary kiln symbolizes RHI Magnesita’s future-orientated business strategy. With this investment, RHI Magnesita is able to offer a new range of higher value-added products to the market. The modern kiln will enhance production capacity and increase the efficiency of RHI Magnesita’s mining activities by processing different particle sizes and raw material grades that currently cannot be produced with the vertical shaft kiln installed in Brumado. In addition, production costs will be reduced significantly, and product quality will be increased. Production with the new kiln is expected to start in 2021. The investment in Brumado is in combination with a sustainability project that benefits the community in the region.

## Worldwide

### Optimizing and Integrating Production Processes With MES

Manufacturing Execution Systems (MES) are computerized systems that are installed to track and document manufacturing processes. RHI Magnesita works on applying MES to cover the shop floor requirements regarding production, detailed scheduling, quality, logistics, maintenance, and real-time performance management. RHI Magnesita’s plants in Radenthein (Austria) and Dalian (China) are serving as pilot plants for MES. In the long run, the company intends to integrate plants across Europe, Asia, and the Americas. MES allows RHI Magnesita to accelerate and smoothen manufacturing processes, improve efficiency and product quality, reduce costs, as well as respond quickly to shop floor innovation and optimization. The system runs through one single platform that controls and monitors all plants, with the target of complete visibility and control. For the implementation, RHI Magnesita is working with state-of-the-art industry practices combined with cutting-edge technology provided by RHI Magnesita’s partner Siemens. A global and integrated Manufacturing Execution System will serve as a key foundation of RHI Magnesita’s digitalization journey.

---

**Europe**

## Sustainability Rocks: The ANKRAL LC Series

When it comes to sustainability, RHI Magnesita is at the forefront of innovative developments. The ANKRAL low carbon technology is the first of its kind and serves as a perfect recycling solution. Compared to conventional products, the low carbon technology significantly lowers the CO<sub>2</sub> footprint of the cement industry. As the low carbon goal has been ambitiously researched within the cement industry, RHI Magnesita is fostering this innovative product to increase the use of recycled materials. In addition, stocks are secured in the long term by reducing cost-intensive recycled material procurement. The ANKRAL low carbon technology has already been used in pilot projects in Austria and Switzerland.

---

**Worldwide**

## Driving our Digital Transformation to 1200 °C and BEYOND

The BEYOND Project is one of RHI Magnesita's main projects to foster modernization with digitalization. RHI Magnesita is going above and BEYOND to optimize customer experience and enhance collaboration and operations in the plants, as improved digitalization advances RHI Magnesita's competitiveness on the market. In cooperation with Microsoft, we are creating the infrastructure and framework needed to become a cloud-first business. Consequently, RHI Magnesita and Microsoft are working on a Cloud Center of Excellence and a data platform that will be the core of all future digital services, analytical applications, and data analyses.

---

**China**

## Rotary Kiln Operating Successfully in Chizhou

The RHI Magnesita Chizhou site (China) includes an extensive dolomite mine and raw material production, as well as facilities for the manufacture of high-quality doloma-based finished products. Construction of the rotary kiln in the dolomite mine started officially in June 2019 and related projects for environmental protection were finished by March 2020. Currently, the kiln is in the production commissioning phase and from March until the end of November 33000 tonnes of qualified doloma sintered materials were produced. When the official operation is underway, the production capacity of doloma sintered material could reach 100000 tonnes per year, which will meet the supply of raw materials for the Chizhou brick plant and provide high-quality material for export.



# A letter from our editor



As the new Chief Editor of the RHI Magnesita Bulletin, it is a pleasure to introduce our latest edition. Published in a year that will be remembered for a global pandemic that has impacted in so many different ways on our professional and personal lives, I hope that you will find among the collection of ten diverse articles thought-provoking topics, innovative ideas, and examples of the customer-centric mindset that defines RHI Magnesita.

With the increasing complexity of electronic scrap, recycling processes have to deal with a much wider variety of metals in the feed. This metallurgical diversity requires customized refractory solutions and continuous lining optimization. In the first article an overview of the Aurubis Lünen recycling process is given as well as the various technical approaches RHI Magnesita used to supply the most appropriate refractory solution to fulfil the customer's requirements. This is followed by a description of the significant advantages provided by an impregnation technology for cement kiln bricks that combats damage caused by alkali-rich environments resulting from firing alternative fuels. An upgraded lining solution for the conical combustion chambers used in iron-ore pellet travelling grate induration machines is introduced in the third paper, which comprises a novel refractory grade as well as an optimized design with a fewer number of shapes.

RHI Magnesita is committed to developing data-based process optimization tools for our customers and the next article provides an example of how artificial intelligence has been successfully applied to predict the refractory lifetime of a RH degasser. In the fifth paper a new liner technology for isostatically pressed flow control products, such as ladle shrouds and submerged entry nozzles, is described and simulation results and industrial measurements are presented indicating the layer can reduce heat loss through the product wall, in addition to providing other benefits during the continuous steel casting process.

Gas purging, where inert gases are introduced into the steel melt, is an important tool in modern secondary metallurgy. To further understand the effect of different purging plug designs, vibration signals were recorded in a water model and, as detailed in the sixth article, found to be a means of quantifying gas purging behaviour. This is followed by the description of a methodology to measure the compressive creep behaviour of fired magnesita materials at elevated temperatures and a modelling approach that demonstrated good agreement with the experimental data.

In the last three papers of this edition the development of various novel testing approaches are reported, namely a corrosion test to quantify refractory wear mediated by gaseous sulphur oxides, a hot-temperature static test to examine raw material dissolution in metallurgical slags, and a new measurement technique to determine the bulk density of granular raw materials.

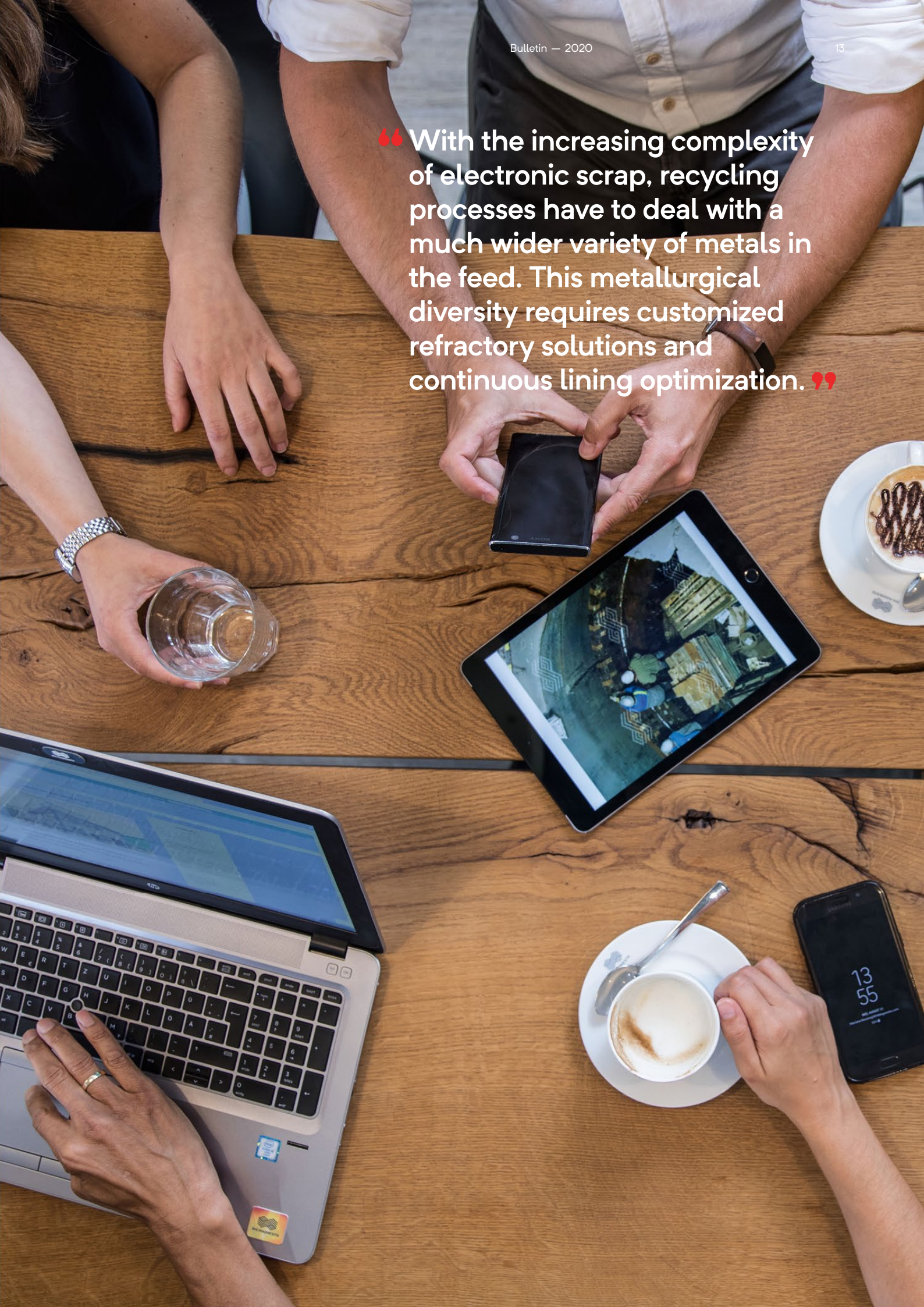
In closing, I would like to wholeheartedly thank all authors who contributed to the 2020 Bulletin as well as the editorial team. It is through their dedication that we are able to share with our valued readers how RHI Magnesita is the driving force of the refractory industry.

Yours sincerely

**Gerald Gelbmann**

Head R&D Europe, CIS and Turkey  
RHI Magnesita

“With the increasing complexity of electronic scrap, recycling processes have to deal with a much wider variety of metals in the feed. This metallurgical diversity requires customized refractory solutions and continuous lining optimization.”





RHI MAGNESITA

# Taking innovation to 1200 °C and beyond

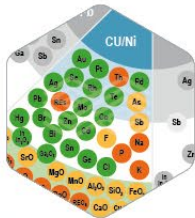
Refractory products withstand extreme temperatures, enabling the production of steel, cement, glass, and many more materials essential to daily life.

Find out more at  
[rhimagnesita.com](https://rhimagnesita.com)

Follow us



# Contents



**16**  
**Customized Refractory Solutions**



**42**  
**Refractory Tubes With Innovative Liner Technology**



**50**  
**Vibrational Determination of Gas Purging**

- 16 Customized Refractory Solutions** to Deal With Increasing Complexity in Copper Recycling
- 24 Impregnation Technology:** Alkali-Resistant Solutions With Performance Benefits
- 32 Development of an Upgraded Refractory Solution** for Traveling Grate Induration Machine Combustion Chambers
- 36 Refractory Lifetime Prognosis** for RH Degassers
- 42 Refractory Tubes With Innovative Liner Technology** for Flow Control and Clean Steel Applications
- 50 Vibrational Determination of Gas Purging** Regime and Efficiency in a Water Model and Validation by a High-Speed Camera
- 56 Compressive Creep Measurements of Fired Magnesia Bricks** at Elevated Temperatures Including Creep Law Parameter Identification and Evaluation by Finite Element Analysis
- 62 Development and Applicability of a New Corrosion Test** to Quantify Refractory Wear Due to Gaseous Sulphur Oxides Action
- 68 Dissolution Behaviour of Various MgO-Containing Raw Materials** in a Secondary Metallurgy Slag
- 74 Bulk Density Determination** of Granular Refractory Materials

## Subscriptions Service and Contributions



We encourage you, our customers and interested readers, to relay our comments, feedback, and suggestions to improve the publication quality.

Email  
[bulletin@rhimaginesita.com](mailto:bulletin@rhimaginesita.com)

Phone  
**+43 50213 5300**



where feasible, are separated. The reducing smelting is carried out in a top submerged lance type furnace— ISASMELT—using a submerged combustion lance supplied with oil, air, and oxygen. The main products of this process step are a black copper alloy with a Cu content of about 80%, which also collects Pb, Sn, Ni, PM and the PGMs, an iron silicate sand, and the so-called KRS oxide, a Zn-containing flue dust. In the following top blown rotary converter (TBRC) process the black copper is further refined to a Cu content of approx. 95%. Pb and Sn are collected in a slag and further processed in a tin-lead rotary furnace. In this reduction process a Pb-Sn alloy is obtained by the addition of carbon and metallic iron as a reductant. The converter copper is finally fire-refined to blister copper in an anode furnace, where complementary cooling scrap is added and cast into anodes for electrolytic refining to Cu cathodes. Ni is separated from the electrolyte as a NiSO<sub>4</sub> product and the anode slime is treated together with other material streams at the precious metal plant.

The multi-metal process requires various slag types in order to fulfil the metallurgical targets of the different process steps. Typical chemical compositions of different slag types used in the process are summarized in Table I.

**Table I.**

Examples of typical chemical compositions of slag types used in the KRS plus recycling process in wt.%.

	Al <sub>2</sub> O <sub>3</sub>	SiO <sub>2</sub>	FeO	CaO	MgO	Cu <sub>2</sub> O	PbO	SnO <sub>2</sub>	ZnO
Slag type A	3.0–5.0	20.0–25.0	45.0–50.0	3.0–5.0	0.5–1.0	0.8–1.0	2.0–3.0	1.5–3.0	6.0–9.0
Slag type B	12.0–15.0	20.0–25.0	45.0–50.0	3.0–5.0	0.5–1.0	0.8–1.0	< 0.5	< 0.5	4.0–5.0

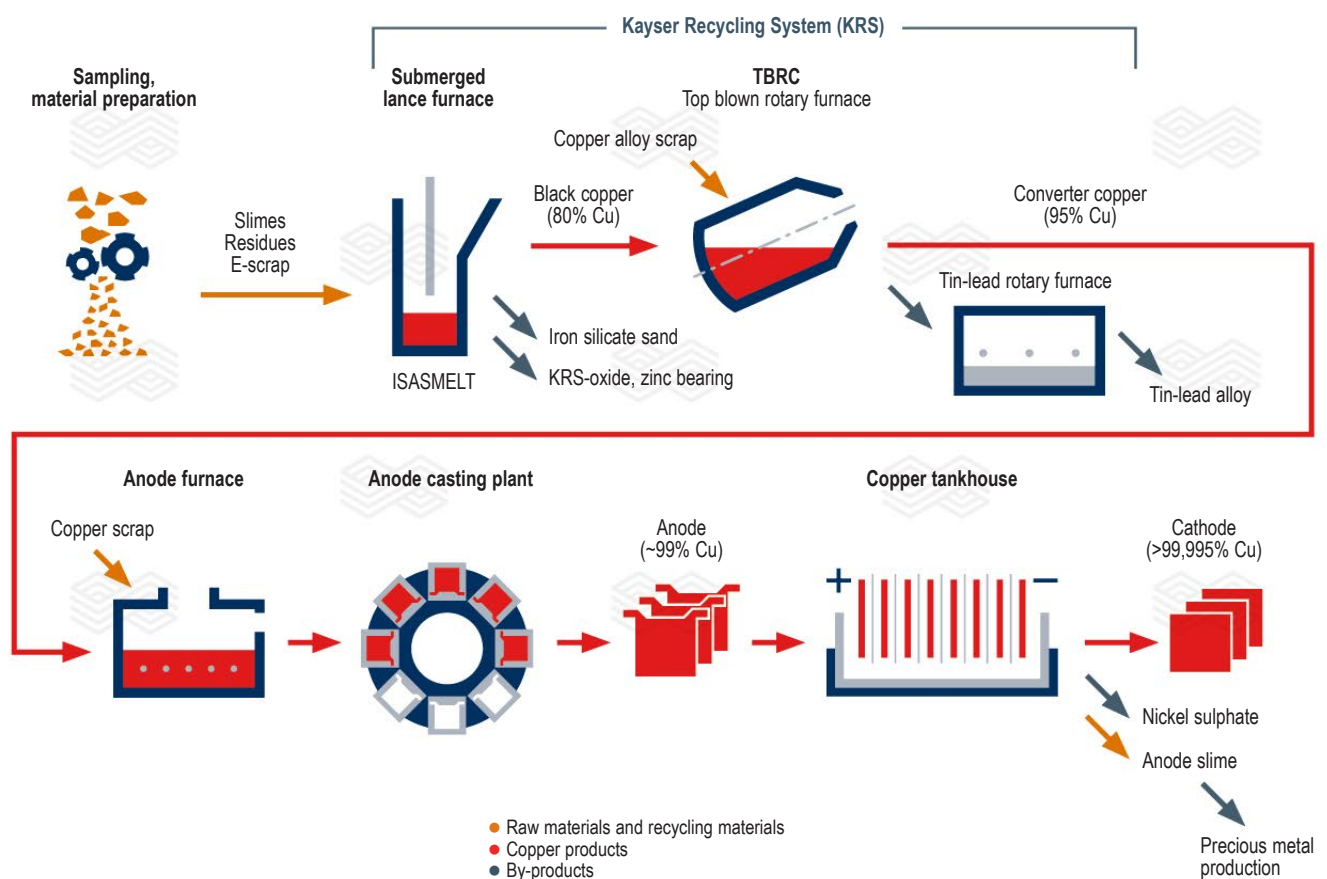
Generally, the used slag types are fayalite-based slags that differ in their amounts of Al, Pb, and Sn depending on the process conditions and slag requirements in the different process steps. Given that, the material selection of refractory materials needs to consider these variances in the slag composition in order to choose the most suitable solution and fulfil the expectations of customers in terms of service lifetime of the refractory lining.

### Refractory Linings in the Secondary Copper Industry

To choose the most appropriate refractory material for a given application the wear mechanisms need to be understood. For instance, knowledge of the chemical reaction behaviour of refractory materials with slags is important to ensure correct application of the products [5]. The more compatible the products are with slags, which are part of metallurgical processes, the less reaction will occur. Consequently, there will be lower wear on the refractory products as a result of corrosion.

**Figure 2.**

Flowsheet of the KRS plus process [3].



In the copper industry, a magnesia-chromite (MgCr) type refractory lining is most common due to its high resistance especially against fayalite-based slags. However, alumina-chromia (AlCr) type materials have been used in several applications as an alternative product in recent years [6]. Table II comprises the chemical and physical properties of two MgCr- and AlCr-based refractory material types typically used. The MgCr brick (brick A) is based on OXICROM material (magnesia-chromite co-clinker), sintered magnesia, and chrome ore. The alumina-chromia brick (brick B) is made of fused alumina and chromium oxide. Both brick grades have low apparent porosity while the cold crushing strength of the alumina-chromia brick is 2–3 times higher than the MgCr brand.

### Major Wear Mechanisms

The observed wear phenomena can generally be subdivided into continuous and discontinuous wear [5,7,8]. Continuous wear is characterized by continuous mass loss as a function of time due to chemical, thermal, and mechanical load (single loads or interrelated) [9]. In most cases, particularly for MgCr bricks, the most frequent continuous wear is corrosion of the refractory by dissolution in melts/slugs with additional hot erosion. Discontinuous wear is mainly characterized by mechanical failure caused by thermal/chemical load occurring discontinuously over time. It is associated with mass loss. Further discontinuous wear phenomena include (structural) spalling, thermal shock failures and bursting reactions (e.g., alkali, carbon, and forsterite) [9].

### Thermochemical Considerations

The chemical corrosion mechanisms of different refractory/slag systems can be evaluated by thermochemical calculations and often this chemical attack of slag is a critical factor for the refractory performance [10]. The slags from secondary copper production are fayalite-based slags but rather complex in their composition. Therefore, interaction of these slags with refractory materials and especially the solubility of  $\text{Al}_2\text{O}_3$  and MgO have not been studied intensively in the literature to date. For example, for AlCr bricks with increasing Zn content, lower solubility of  $\text{Al}_2\text{O}_3$  and thus less driving force for direct dissolution into the slag phase has been reported [11]. Once the slag becomes saturated with the refractory component, in this case  $\text{Al}_2\text{O}_3$ , anorthite will crystallize from the melt and stop

the dissolution process. One important parameter for process control is the oxygen partial pressure, which can have a significant effect on the refractory corrosion resistance by changing the ferric/ferrous ratio in the slag. It was concluded that for  $\text{Al}_2\text{O}_3$ -based refractories lower wear rates under oxidizing conditions can be expected while for MgO-based materials (strongly) reducing conditions would be desirable [12]. For MgO- $\text{Cr}_2\text{O}_3$  rebonded bricks the resistance to chemical corrosion decreased with increasing  $\text{Al}_2\text{O}_3$  and  $\text{Fe}_2\text{O}_3$  content [13,14].

To determine the driving force for direct dissolution of the process slag types A and B mentioned in Table I, the solubility of MgO and  $\text{Al}_2\text{O}_3$  was calculated with FactSage 7.0 using the counter diffusion method. The databases FactPS, FToxide, and FTmisc were used for the calculations. The MgO solubility was calculated with brick A refractory material and  $\text{Al}_2\text{O}_3$  with brick B in a temperature range from 1200–1300 °C and an oxygen partial pressure varying from  $10^{-10}$  to  $10^{-08}$  atm. The results for MgO and  $\text{Al}_2\text{O}_3$  are illustrated in Figure 3 and represent the average solubility for both slag types A and B in interaction with MgCr and AlCr brick types. In general, the solubility for MgO was less than for  $\text{Al}_2\text{O}_3$ . The MgO solubility was highly sensitive to changes in the process temperature and oxygen partial pressure while the  $\text{Al}_2\text{O}_3$  solubility was less sensitive to changes in these two process parameters. At 1200 °C and an oxygen partial pressure of  $10^{-10}$  atms the solubility of MgO was 2.8–2.9%. With a temperature increase of 100 °C to 1300 °C, the solubility changed drastically to 14.7–14.8%. Under more oxidizing conditions (oxygen partial pressure of  $10^{-08}$  atms) the solubility of MgO increased and ranged from 11.6 to 17.3% in the liquid slag phase. The solubility of  $\text{Al}_2\text{O}_3$  in both slags was similar and did not change significantly with the changes in the process slag type. At 1300 °C the solubility was quite stable over the investigated oxygen partial pressure range at a level of around 20%.

The calculations indicated that especially at a lower oxygen potential ( $p_{\text{O}_2}$ ) the solubility of MgO was much less than that of  $\text{Al}_2\text{O}_3$  for the investigated slag types. Based on the actual process slag composition and process parameters, the calculation can give a good indication for the tendency to direct the dissolution potential of certain refractory oxides in different process slag types. The refractory degradation rate is influenced by the concentration gradient. Figure 4 shows for example the concentration gradient in the refractory/slag system for  $\text{Al}_2\text{O}_3$  and MgO.

**Table II.**

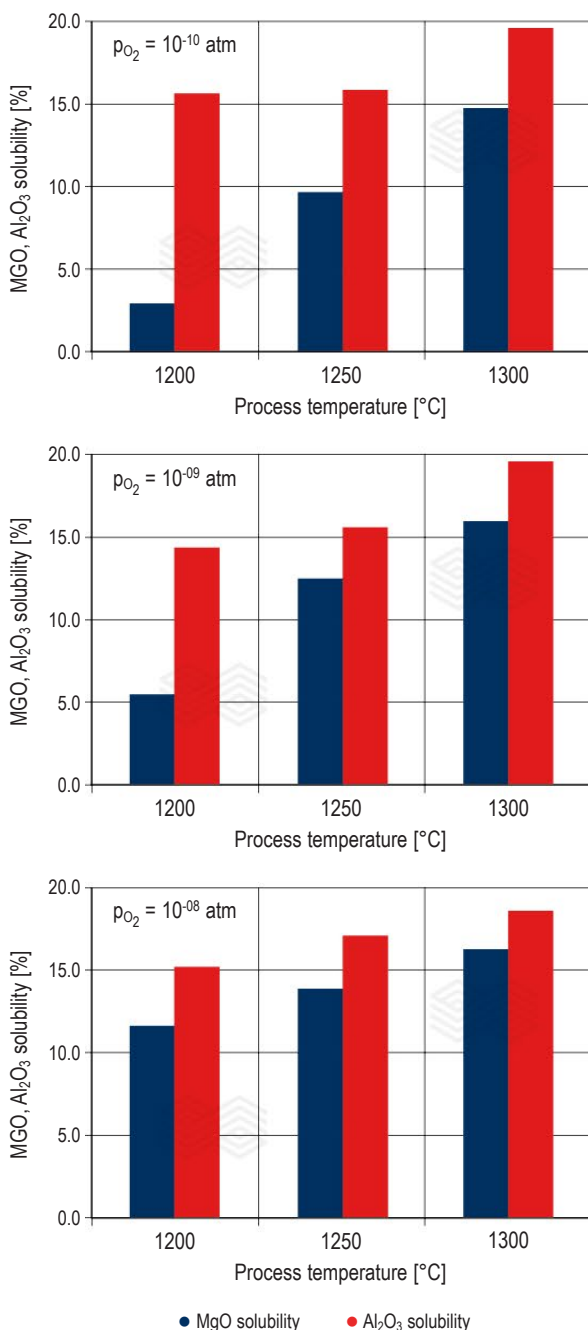
Physical and chemical properties of investigated MgCr- and AlCr-based refractory bricks used in the current investigation.

	Chemical composition (ISO 12677)								Physical properties	
	MgO	$\text{Al}_2\text{O}_3$	$\text{Cr}_2\text{O}_3$	$\text{Fe}_2\text{O}_3$	$\text{SiO}_2$	CaO	$\text{ZrO}_2$	$\text{P}_2\text{O}_5$	CCS (ISO 10059-1)	Apparent porosity (ISO 5017)
	[wt.%]	[wt.%]	[wt.%]	[wt.%]	[wt.%]	[wt.%]	[wt.%]	[wt.%]	[MPa]	[Vol.%]
Brick A Type MCr50 ISO 10081-2	59.5	6.0	19.0	13.5	0.5	1.3	–	–	70	17
Brick B Type ACr80/5 ISO 10081-4	–	79	10.7	0.3	3.0	–	5.0	1.1	155	15

This indicates that the direct dissolution rate for slag type B (12–15%  $\text{Al}_2\text{O}_3$ ) and AlCr brick B (max. solubility 14.8%) can be expected to be the lowest of the investigated refractory/slag systems as the slag is almost saturated with aluminium at low process temperatures ( $T = 1200\text{ }^\circ\text{C}$ ) and oxidizing conditions ( $p_{\text{O}_2} = 10^{-08}\text{ atm}$ ). In the case of reducing conditions ( $T = 1200\text{ }^\circ\text{C}$ ;  $p_{\text{O}_2} = 10^{-10}\text{ atm}$ ) the lowest corrosion rate can be expected for MgO-based grades (max. solubility 2.8% vs. approx. 1% MgO in both slag types). All investigated refractory/slag systems were highly sensitive to changes in the process temperature. An increase to  $1300\text{ }^\circ\text{C}$  changed the solubility of  $\text{Al}_2\text{O}_3$  up to 20% and up to 17% for MgO. Hence, the tendency to direct dissolution also increased.

**Figure 3.**

**Average maximum MgO and  $\text{Al}_2\text{O}_3$  solubility under equilibrium conditions in the liquid slag phase depending on temperature (1200–1300  $^\circ\text{C}$ ), oxygen partial pressure ( $10^{-10}$ – $10^{-08}\text{ atm}$ ), and process slag type (slag type A and slag type B).**



## Postmortem Analysis

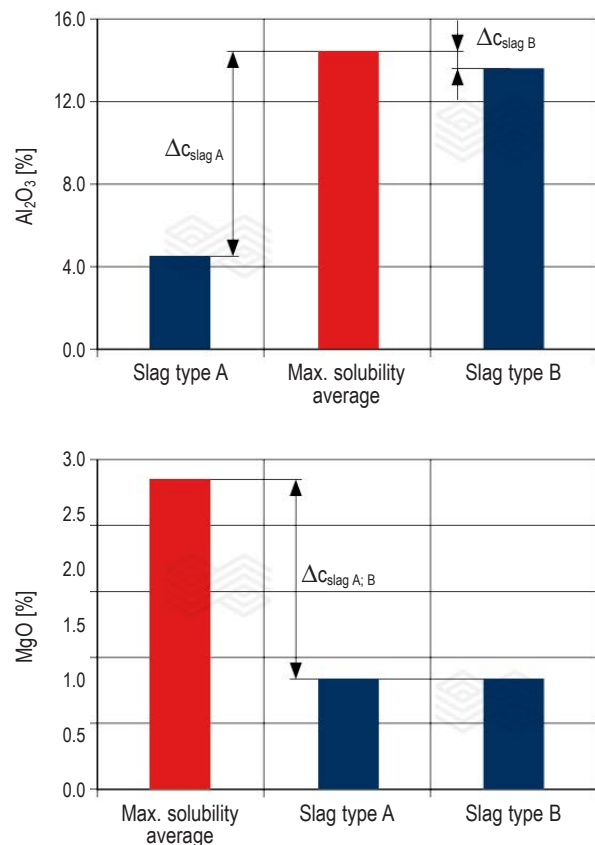
For the postmortem analysis three samples, namely one MgCr and two AlCr bricks, were collected after their service life in an Aurubis Lünen furnace.

## Analytical Procedure

Every single postmortem study starts with the visual inspection carried out on the brick cut section followed by the selection of samples for chemical analyses and mineralogical investigations. The chemical analyses were carried out using X-ray fluorescence analysis (Bruker S8 TIGER). The mineralogical investigations were performed on polished sections using a reflected light microscope, X-ray diffraction (Bruker D8 ADVANCE), and a scanning electron microscope (JEOL JSM-6460) combined with an energy-dispersive and wavelength-dispersive X-ray analyser.

**Figure 4.**

**Concentration gradient for slag types A and B for  $\text{Al}_2\text{O}_3$  of the AlCr brick type B ( $T = 1200\text{ }^\circ\text{C}$ ;  $p_{\text{O}_2} = 10^{-08}\text{ atm}$ ) and for MgO of the MgCr brick type B ( $T = 1200\text{ }^\circ\text{C}$ ;  $p_{\text{O}_2} = 10^{-10}\text{ atm}$ ).**



## Mineralogical Investigation of a MgCr Brick

### Macroscopic overview

The residual brick thickness of the used magnesia-chromite brick (Brick A) was about 70 mm. The immediate brick hot face was smooth and partially covered with spherical slag droplets (Figure 5). On the cut section of the refractory the macroscopically visible infiltration depth was up to approximately 20 mm from the hot face.

### Mineralogical investigation

The <1 mm thin slag coating on the immediate brick hot face consisted of (Zn)-Fe-Al-oxide of type hercynite ( $\text{FeAl}_2\text{O}_4$ ), Fe-(Zn)-silicate of type fayalite ( $\text{Fe}_2\text{SiO}_4$ ) and copper, tin, and iron enriched glassy phase (Figure 6a). Below the slag coating the refractory was infiltrated up to a depth of ~ 20 mm from the hot face. Within the infiltrated brick microstructure, corrosion of MgO from the OXICROM material due to chemical slag attack had taken place. In addition, sintered magnesia from the fines was corroded. The main reaction products determined include Mg-silicate forsterite ( $\text{Mg}_2\text{SiO}_4$ ) and Ca-Mg-silicate monticellite ( $\text{CaMgSiO}_4$ ). Chromite showed higher corrosion resistance against chemical slag attack (Figure 6b).

In the infiltrated brick microstructure Cu- and Pb-oxide were also determined. The degree of metal oxide infiltration generally depends on several parameters such as surface tension, boundary angle to the refractory oxide, metal density, bath level and size of brick pores,  $p_{\text{O}_2}$ , and temperature [6]. The viscosity has an additional influence on the infiltration depth. Particularly in the case of metal oxides such as CuO (mainly cuprite,  $\text{Cu}_2\text{O}$ ) and PbO, the wetting angle between the metal oxide and refractory is low, thus favouring deep-reaching infiltration of the refractory microstructure. Based on experimental work, it was found that the boundary angle between  $\text{Cu}_2\text{O}$  and periclase ( $\text{MgO}$ ) at 1200 °C is about 15 °C [6].

**Figure 5.**

Magnesia-chromite brick (Brick A). Smooth hot face partially covered with spherical slag droplets (S). Sample for mineralogical investigation (M).

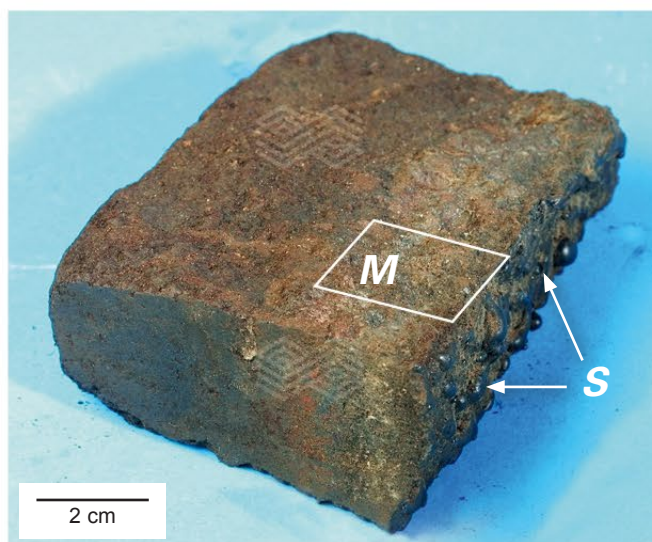
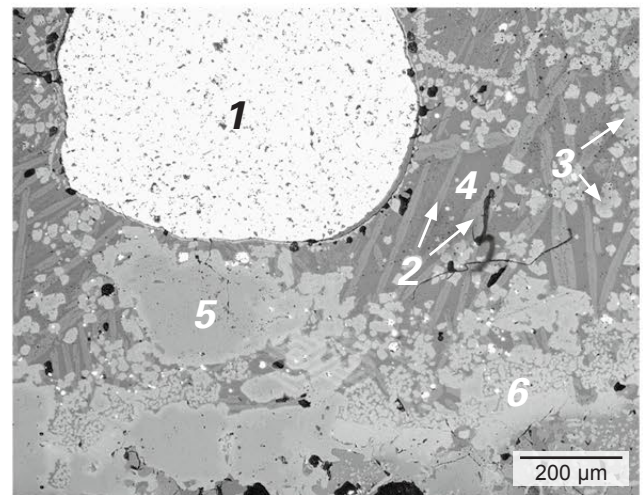
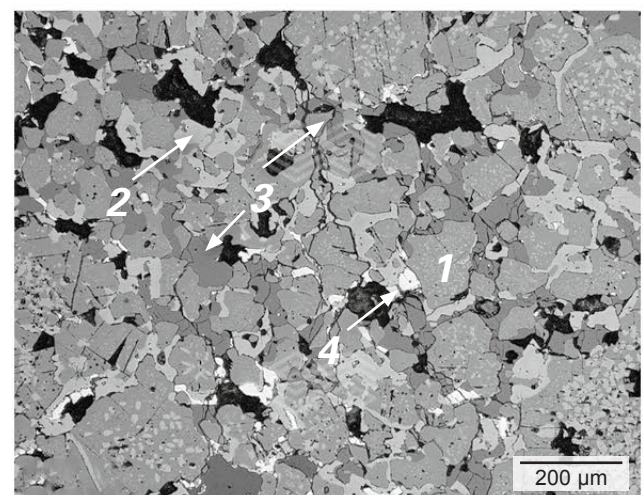


**Figure 6.**

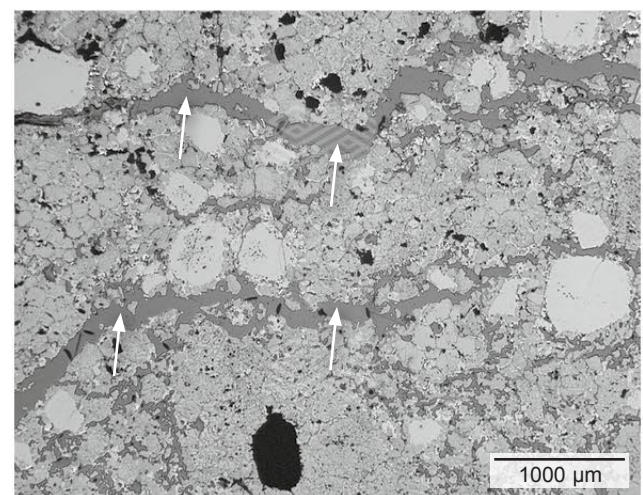
Mineralogical investigation by reflected light microscopy and scanning electron microscopy. (a) Slag coating. CuSnFe(Pb)-metal (1). Fe-(Zn)-silicate (2). Fe-Al-(Zn)-oxide (3). Glassy phase (4). Chromite “swimming” in the slag (5). Thin reaction layer (6). (b) Corroded microstructure (2 mm from hot side). Sintered magnesia (1). Chromite (2). Formation of forsterite and minor monticellite (3). Cu/Pb-oxide (4). (c) Formation of short running cracks through the microstructure (at approx. 5 mm from hot face).



(a) SEM-BSE



(b) Inc. light, dry



(c) Inc. light, dry

Additionally, with an infiltrated and partly softened brick microstructure there was formation of short running cracks (Figure 6c).

### Mineralogical Investigation of an AlCr Brick

#### Macroscopic overview and cut sections

Both collected samples represent bricks of type B. Figure 7a shows a residual thickness of approximately 290 mm; Figure 7b has a residual brick thickness of 110–150 mm. At the cold face of sample 1 the brick was partly broken. In both samples the immediate brick hot face was covered with a slag coating (Figure 7). On the cut section of the refractory the macroscopically visible infiltration depth of both samples was up to ~ 5 mm from the hot face. Cracks were visible on the cut surface of example 2, which were running parallel to the hot side.

#### Chemical composition

The chemical compositions of the hot side of sample 1 and 2 are shown in Table III. Particularly the infiltrated brick hot face (0–5 mm) was highly enriched with SiO<sub>2</sub> and Fe<sub>2</sub>O<sub>3</sub>. Elevated CuO, ZnO, CaO, Na<sub>2</sub>O, and MgO were determined.

**Table III.**

Chemical composition of the hot side in wt.% (alumina-chromite brick).

Sample		Na <sub>2</sub> O	MgO	Al <sub>2</sub> O <sub>3</sub>	SiO <sub>2</sub>	P <sub>2</sub> O <sub>5</sub>	CaO	Cr <sub>2</sub> O <sub>3</sub>	Fe <sub>2</sub> O <sub>3</sub>	ZrO <sub>2</sub>	ZnO	CuO
Sample 1	Hot side 0–5 mm	1.8	1.3	55.3	15.7	n.d.	1.5	5.1	12.9	3.6	1.6	1.2
Sample 2	Hot side 0–5 mm	3.8	1.4	36.0	17.2	1.4	2.4	6.0	22.6	2.1	5.0	2.1

n.d. = not detected

### Mineralogical investigation

According to the mineralogical investigation, the following microstructural changes can be summarized for both samples:

The immediate brick hot face was covered with a thin slag coating in sample 1 (Figure 7a) and a thick slag coating in sample 2 (Figure 7b), which was composed of Zn-Mg-(Mn)-Al-(Ti)-Fe-Cr-oxide of spinel type, Zn-Mn-Mg-Fe-silicate as well as phosphorus, lead, and (partly) barium enriched glassy phase (Figure 8b). Below the slag coating in the first 5 mm from the hot face the brick microstructure was degenerated. Mainly corrosion of the fused alumina component and formation of Fe- and Zn-oxide enriched alumina had taken place. The chrome-corundum matrix was infiltrated and recrystallized. The microstructure was infiltrated with phosphorus-containing Na-Al-Ca-K-Fe-silicate (Figure 8c).

At the interface between the infiltrated and noninfiltrated brick microstructure cracks had formed due to changed thermomechanical properties of the bricks (Figure 8d).

**Figure 7.**

Alumina-chromite bricks (Brick B). (a) Thin slag coating on the hot side (S). Brick partly broken at the cold side during removal (circle). (b) Thick slag coating on the hot side (S). Cracks running parallel to the hot side are visible (arrows). Samples for mineralogical investigation (M).



## Results/Conclusion

The Aurubis Lünen recycling process is designed to treat especially complex feed materials to obtain multi-metal recovery for Cu, Ni, Sn, Pb, Zn, PM, and PGMs. The thermochemical calculations with FactSage indicated that especially at lower oxygen potential the solubility of MgO was much lower than for Al<sub>2</sub>O<sub>3</sub> for the investigated slag types. Based on the actual process slag composition and process parameters under oxidizing conditions, the lowest direct dissolution rate for the refractory/slag system type B was observed.

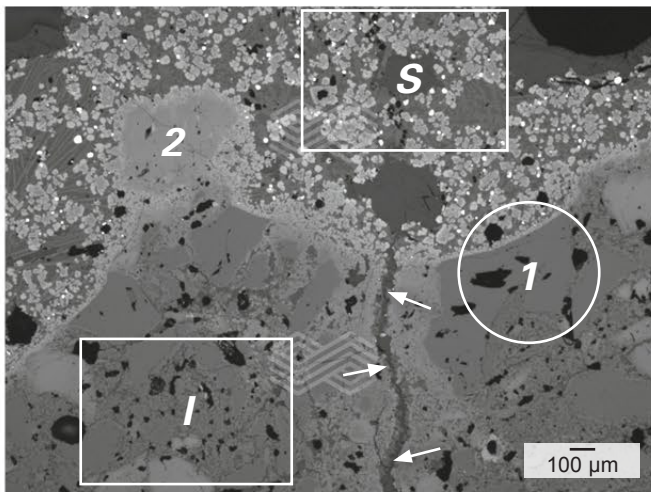
The introduced postmortem studies carried out on basic (magnesia-chromite) and the nonbasic (alumina-chromite) bricks demonstrated that as consequence of chemical attack by slag the infiltration and corrosion of the brick's inherent components led to a softening of the brick's microstructure, loss of flexibility, and brick strength.

This weakened microstructure was then susceptible to continuous wear by hot erosion. Additionally, due to the changed thermomechanical properties of the refractory, thermal shock led to crack formation primarily at the interface between the infiltrated and noninfiltrated brick area, and finally to discontinuous wear by spalling.

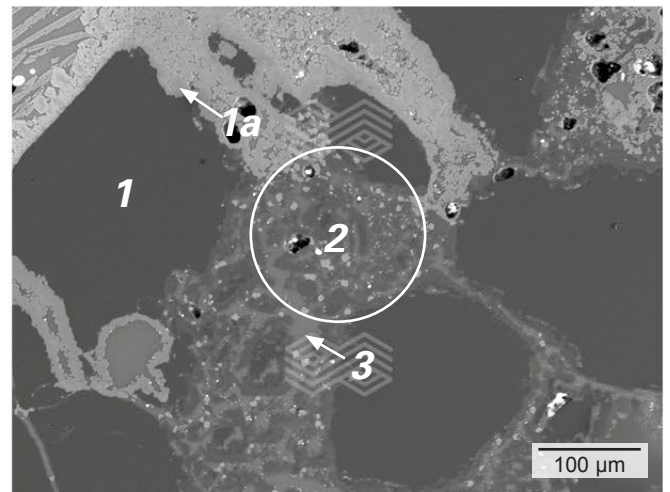
On the basis of the specific investigation results, combined with long-term service experience, the most appropriate choice for the furnace wear lining can be made. This is frequently supported by active collaborations with the customer, leading to tailor-made solutions for each client.

**Figure 8.**

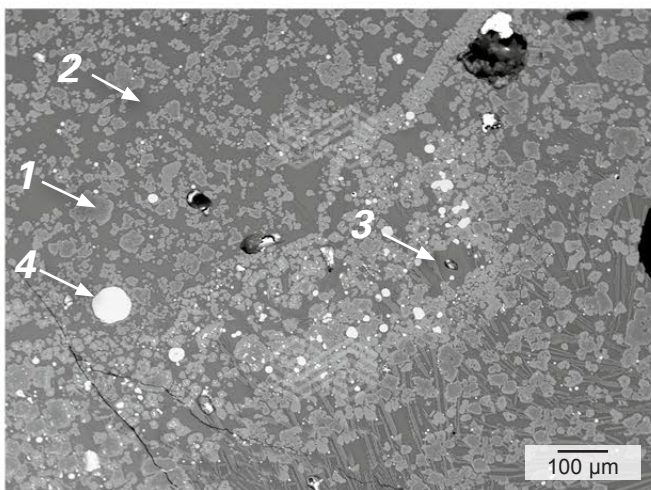
(a) Overview of the hot side. Slag coating/reaction layer (S). Infiltrated microstructure below (I). Corroded fused alumina (1). Chrome-corundum matrix (2). Vertical crack filled with slag (arrows). (b) Slag coating/reaction layer consists of Zn-Mg-(Mn)-Al-(Ti)-Fe-Cr-oxide of spinel type (1). Phosphorus, lead, and partly barium containing Zn-Mn-Al-Ca-Fe-silicate (glassy phase) (2). Zn-Mn-Mg-Fe-silicate (3). Cu-Ni-metal (4). (c) Immediate hot side. Corrosion of the fused alumina (1). Fe-Zn-aluminate (1a). Infiltrated and recrystallized chrome-corundum matrix (2). Infiltration of phosphorus-containing Na-Al-Ca-K-Fe-silicate (3). (d) At the interface between infiltrated (I) and noninfiltrated (O) brick microstructure crack formation can be observed (arrows).



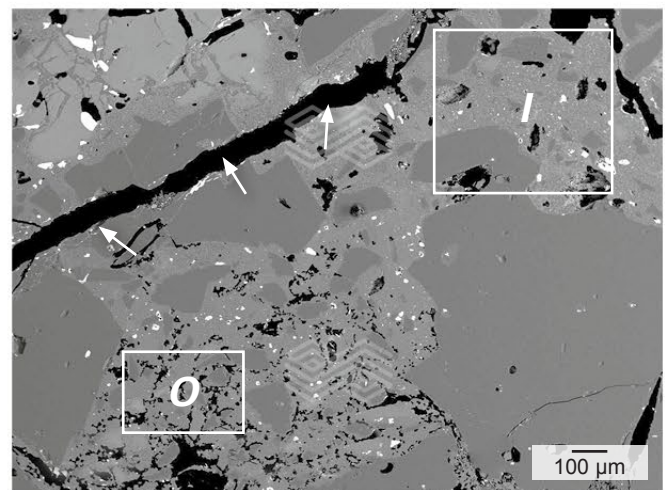
(a) Inc. light, dry



(c) SEM-BSE



(b) SEM-BSE



(d) SEM-BSE

## References

- [1] Reuter, M. et al. Metal recycling opportunities, limits, infrastructure. *UNEP International Resource Panel*, 2013, 30.
- [2] Shibata, E. Important roles of non-ferrous smelters for treatments of secondary raw materials. Presented at the Short Course Recycling, Copper 2016, Kobe, Japan, 2016.
- [3] <https://www.aurubis.com/products/recycling/technology>; accessed January 2018.
- [4] Davenport, W. G., King, M., Schleisinger, M. and Biswas, A. K. Extractive metallurgy of copper. Kidlington, Oxford, 4<sup>th</sup> Edition, 2002.
- [5] Routschka, G. Praxishandbuch Feuerfeste Werkstoffe, Vulkan-Verlag, Essen, 6. Auflage, 121.
- [6] Rigby, A. J. The use of alumina-chrome refractories in the high wear areas of anode refining vessels. Presented at the Copper 2013, Santiago de Chile, Chile, 497–505.
- [7] Gregurek, D., Reinharter, K., Majcenovic, C., Wenzl, C. and Spanring, A. Overview of wear phenomena in lead processing furnaces. *Journal of the European Ceramic Society*. 2015, 35, 1683–1698.
- [8] Harmuth, H. and Vollmann, S. Refractory corrosion by dissolution in slags – Challenges and trends of present fundamental research. *Iron and Steel Review*. 2014, 58, 4, 157–170.
- [9] Malfliet, A., Lotfian, S., Scheunis, L., Petkov, V., Pandelaers, L., Jones, P.T. and Blanpain, B. Degradation mechanisms and use of refractory linings in copper production processes: A critical review. *Journal of the European Ceramic Society*. 2014, 34, 849–876.
- [10] Kennedy, C.R. and Poeppel, R.B. Corrosion resistance of refractories exposed to molten acidic coal-ash slags. Presented at InterCeram, Lübeck, Germany, 1978.
- [11] Chen, L., Guo, M., Blanpain, B. and Malfliet, A. Investigation on the interactions between alumina-chrome refractories and ZnO-containing fayalite slags. *Journal of the European Ceramic Society*. 2017, 35, 2641–2650.
- [12] Zhang, S. and Lee, W. E. Use of phase diagrams in studies of refractories corrosion. *International Materials Reviews*. 2000, 45, 2, 41ff.
- [13] Tamaki, K. Wear of Chrome Brick in Secondary Refining Furnace. *Taikabutsu Overseas*. 1993, 13, 4.
- [14] Asano, K., Hayashi, K. and Horio, T. Reaction between refractories and some refining slags – influence of furnace atmosphere on corrosion of MgO-Cr<sub>2</sub>O<sub>3</sub> rebonded bricks. *Taikabutsu Overseas*. 1987, 7, 4, 3ff.

Originally published in World of Metallurgy – ERZMETALL 2/2018, reprinted with permission from the GDMB.

## Authors

Dean Gregurek, RHI Magnesita, Technology Center, Leoben, Austria.

Jürgen Schmidl, RHI Magnesita, Vienna, Austria.

Katja Reinharter, RHI Magnesita, Technology Center, Leoben, Austria.

Christian Majcenovic, RHI Magnesita, Technology Center, Leoben, Austria.

Alfred Spanring, RHI Magnesita, Vienna, Austria.

Stefan Schmidt, Aurubis AG, Lünen, Germany.

Jörn Böhlke, Aurubis AG, Lünen, Germany.

**Corresponding author:** Dean Gregurek, [dean.gregurek@rhimagnesita.com](mailto:dean.gregurek@rhimagnesita.com)



Roland Krischanitz and Susanne Jörg

# Impregnation Technology: Alkali-Resistant Solutions With Performance Benefits

In cement production, substitution of traditional fossil fuels by alternative fuels can have a significant impact on the operating conditions and refractory performance. The use of alkali-rich fuels or the substitution of sulphate-rich fuels by fuels lower in sulphate content, shifts the alkali/sulphate ratio towards more alkali-rich environments. Existing shaped refractory solutions for such conditions, based on SiC addition, increase the thermal conductivity of the lining and reach their limits in steam-rich environments caused by alternative fuels with a high moisture content. However, an alternative technology, based on impregnation with nanoparticle-sized silica sol, offers an alkali-resistant and coating-repellent brick solution without the above-mentioned drawbacks associated with SiC.

Conventional fuels usually have a certain sulphur content, for example petcoke contains up to 8 wt.%. The substitution with low sulphate containing AFs can result in a significant shift of the alkali sulphate ratio (ASR) towards an overload of alkalis, not only because of the introduction of alkali-rich fuels but also due to the lack of balancing sulphate from conventional fuels. This can lead to higher wear rates in sections of the cement pyro-process, lined with nonbasic refractory materials, due to so-called alkali attack. A widely used technology to increase alkali resistance is the addition of SiC, but there are certain disadvantages associated with this approach. This paper introduces the silica-sol impregnation technology as an alternative to SiC, which shows significant advantages such as no modification of the thermal conductivity, steam insensitivity, and excellent coating-repellent properties.

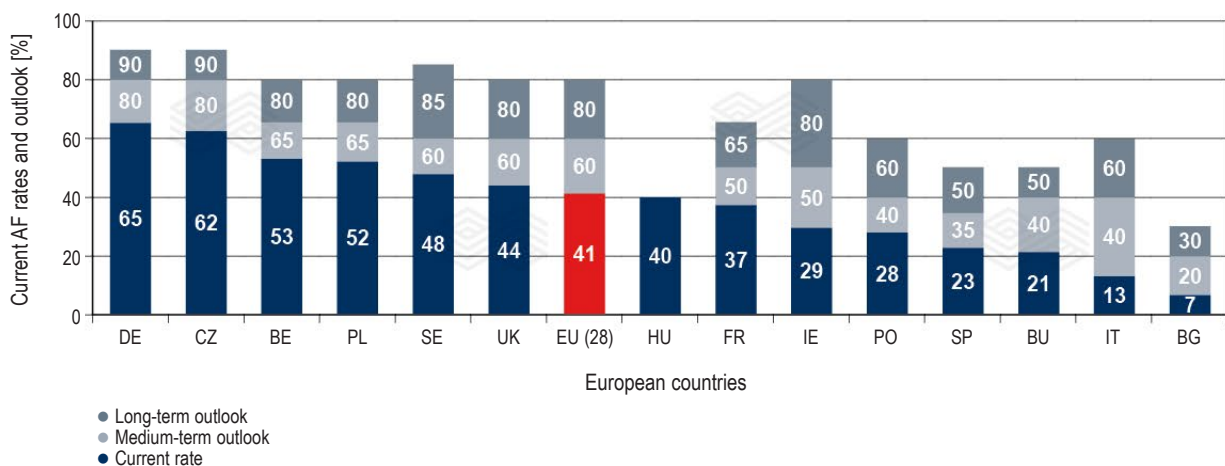
## Introduction

The substitution of fossil fuels by alternative fuels (AFs) is an ongoing practice, which has already progressed far in Central Europe, with mean substitution rates of up to 65% in Germany [1] and many kilns operating at levels of > 80%. Additionally, substitution rates vary quite dramatically between different countries in Europe (Figure 1) and it is an ongoing and extending practice in many regions of the world. The substitution of conventional, fossil-based fuels by AFs has also become very important in relation to CO<sub>2</sub> emission reductions, with the use of biomass-based fuels, which are considered to be CO<sub>2</sub> neutral, being targeted. Besides carbon-capture technologies and reducing the clinker factor, AFs are one of the main levers for the reduction of CO<sub>2</sub> emissions in cement production.

## Impregnation Technology—Advantages Compared to SiC

The addition of SiC is a well-known approach to improve the resistance of alumina refractories against alkali bursting. At the same time, the lining is also provided with coating-repellent properties. The reasons for this are the oxidation of SiC in the usually oxygen-rich kiln atmosphere and the formation of silicon dioxide. Silicon dioxide can absorb alkalis and forms a sealing at the hot face, which protects the refractory material from further alkali infiltration. This hot face sealing also results in coating-repellent properties since coating rings, often the result of excess amounts of alkali salts or sulphate in particular, are not able to firmly adhere to the surface and easily pull off due their own weight.

**Figure 1.** Use of AFs in selected European countries; current rates and outlook [1].



However, the effectiveness of these SiC-containing bricks is strongly dependent on the amount of SiC added. Often refractories with only a very low SiC content (up to 5%) are applied with limited effect. The reasons for keeping the SiC content as low as possible include the high raw material costs as well as the high thermal conductivity of SiC, leading to increased kiln shell temperatures and energy losses.

The impregnation technology provides an alternative approach to combat alkali damage and coating adherence without any of the drawbacks associated with SiC. During impregnation, the bricks are treated with a nanoparticle sized silica-sol solution under vacuum, which fills the pores. This impregnation is not just a superficial treatment, it fills the entire porosity of a brick. After drying silica remains in the structure and as with SiC bricks, improves the alkali resistance. The silica absorbs alkalis without the formation of harmful feldspatoidic minerals such as leucite, which leads to alkali bursting reactions. In operation, a hot face sealing is formed that inhibits further alkali salt infiltration and provides coating-repellent properties. Moreover, the deposition of silica in the pore structure in general reduces permeability, leading to an additional protection effect. Since the added silica is not part of the brick structure but just fills the open porosity, the brick integrity is not affected when it reacts with alkalis. This is different to SiC-containing bricks, where SiC is added in the formulation and is part of the brick structure. As a result, any alteration of the SiC (such as oxidation) affects the brick structure to a certain extent. Table I shows the main physical properties of silica-sol impregnated products in comparison to standard products. The impregnation treatment leads to a reduction of porosity as well as an increase in bulk density and cold crushing strength.

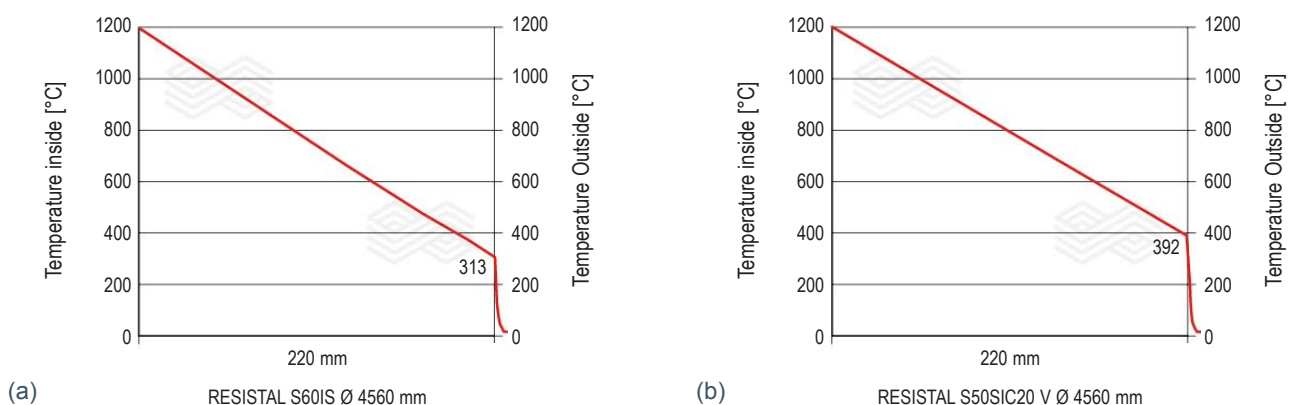
**Table I.**

Comparison of the physical properties of conventional and impregnated fireclay and alumina bricks.

	Fireclay		Fireclay		Andalusite		Fireclay/Bauxite		Bauxite	
	Conventional	Impregnated	Conventional	Impregnated	Conventional	Impregnated	Conventional	Impregnated	Conventional	Impregnated
BD [g/cm <sup>3</sup> ]	2.28	2.33	2.28	2.30	2.52	2.58	2.36	2.40	2.74	2.80
AP [%]	17.0	15.0	19.0	16.0	16.0	13.0	17.5	17.0	19.0	16.0
CCS [N/mm <sup>2</sup> ]	50	70	45	65	80	95	55	65	80	100
RuL Ta [°C]	1470	1470	1420	1420	1650	1650	1440	1440	1520	1520

**Figure 2.**

Heat transfer calculation of (a) silica-sol impregnated brick and (b) 20 wt.% SiC brick.



One of the benefits of the silica-sol impregnation technology is its low thermal conductivity since the impregnation process does not increase this property. While an impregnated andalusite-based product like RESISTAL S50IS has a thermal conductivity of 1.7 W/mK at 1200 °C, comparable to the standard product, a brick containing 10 wt.% SiC has a thermal conductivity of 2.5 W/mK at this temperature. At a SiC content of 20 wt.% the thermal conductivity increases to 3.0 W/mK, which is already at the same level as high-purity magnesia spinel bricks.

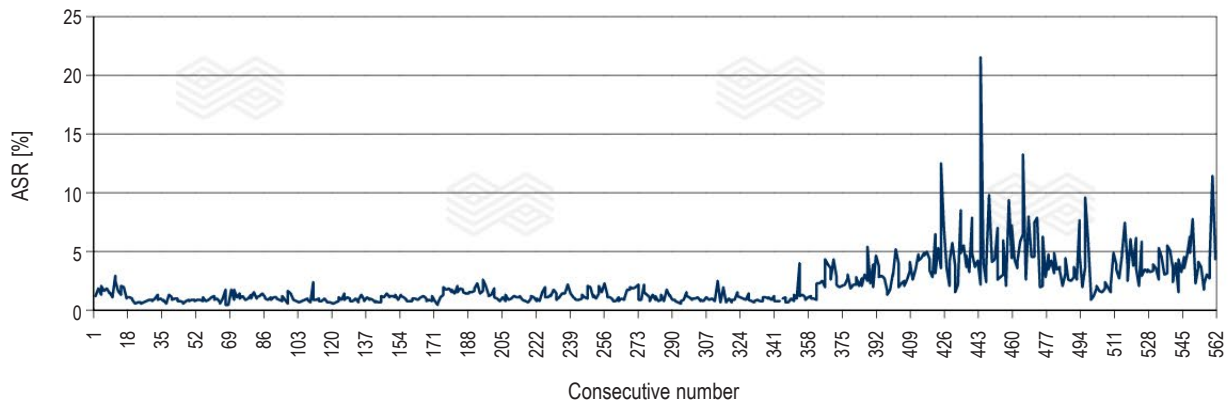
Heat transfer calculations assuming an inside kiln temperature of 1200 °C and a lining thickness of 220 mm result in a shell temperature of 313 °C for an impregnated brick (Figure 2a). This increases to 392 °C for a brick containing 20 wt.% SiC (Figure 2b) and slightly above 400 °C when the SiC content is 30 wt.%.

### Petcoke Substitution

As mentioned previously, changes in fuel type can have a significant impact on the operating conditions and refractory performance. Petcoke is a commonly used fuel because of its high calorific value and comparatively low cost, especially if it has a higher sulphate content. However, the implementation or substitution of this fuel has an important impact on process conditions, in particular on the ASR. The example in Figure 3 shows the impact of substituting petcoke with AFs with a much lower sulphate content. The ASR in the hot meal increased from a quite balanced ratio of about 1 to levels much higher than 5, resulting in a strong alkali overload and, accordingly, a change in wear mechanisms in certain areas.

**Figure 3.**

Change of ASR in hot meal before and after substitution of petcoke.



In the respective kiln this led to a significant reduction of refractory performance in the safety zone from 4 to 2 years (Figure 4). A postmortem investigation revealed the main wear mechanism was due to strong chemothermal load caused by alkali salt infiltration. The chemical investigation showed 11.65 wt.% potassium near the hot face and 4.95 wt.% further inside the brick (Table II). Accordingly, the ASR was >100 near the hot face and 1.16 in the middle of the brick. The severe alkali overload near the brick hot face resulted in the formation of leucite ( $\text{KAlSi}_2\text{O}_6$ ). The formation of this phase is known to cause a significant volume expansion of up to 36%, depending on the original phase composition. In addition, the thermal expansion of the other newly formed phases is significantly higher compared to the original components. For example the thermal expansion of nepheline ( $\text{NaSi}_2\text{O}_6$ ) is three times higher than that of mullite ( $\text{Al}_6\text{Si}_2\text{O}_{13}$ ). This can lead to crack formation in the bricks and spalling of the hot face brick parts, even in the case of minor thermal shocks.

Since the lifetime of the refractory lining had reduced from 4 to 2 years in the safety zone, in a discussion with the customer it was decided to install RESISTAL S60IS, a silica-sol impregnated andalusite brick.

**Figure 4.**

Sectioned fireclay bricks from the safety zone. C1 and C2 indicate where samples were taken for the analyses.

**Table II.**

Chemical and mineral phase analyses of a cement rotary kiln fireclay brick sample from running metre 70. On ignited sample (1050 °C) by X-ray fluorescence analysis (1), on original sample (2), total silicon content originating from  $\text{SiO}_2$  and SiC given as  $\text{SiO}_2$  (3), and ICP-OES optical emission spectroscopy by inductively coupled plasma (4).

General information			
Aggregate	Cement rotary kiln		
Installation area	Calcining zone		
Brick type	Fireclay brick		
Sampling	0–10 mm	45–65 mm	
Chemical analyses		Wt.%	Wt.%
Loss on ignition (1050 °C) (DIN 51081)		3.36	6.24
Determination by XRF <sup>1)</sup> (ISO 12677)			
MgO	0.31	0.43	
Al <sub>2</sub> O <sub>3</sub>	36.2	39.1	
SiO <sub>2</sub>	47.8	51.7	
P <sub>2</sub> O <sub>5</sub>	0.04	0.05	
CaO	0.38	0.30	
TiO <sub>2</sub>	0.86	0.92	
Fe <sub>2</sub> O <sub>3</sub>	1.71	1.94	
Determination by titration <sup>2)</sup>			
Chloride	1.77	4.01	
Determination by C-S elemental analysis <sup>2)</sup> (DIN 51085)			
Sulfur	0.03	0.03	
SO <sub>3</sub>	0.07	0.07	
Determination by ICP-OES <sup>2)3)</sup> (ISO 26845)			
K <sub>2</sub> O	11.65	4.95	
Na <sub>2</sub> O	0.20	0.30	
Phase analysis by x-ray diffraction <sup>2)</sup>			
Mineral phase	Formula	Wt.%	
Mullite	Al <sub>6</sub> Si <sub>2</sub> O <sub>13</sub>	10–50	
Leucite	KAlSi <sub>2</sub> O <sub>6</sub>	10–50	
Sylvite	KCl	10–50	
Andalusite	Al <sub>2</sub> (SiO <sub>4</sub> )O	5–10	
Quartz	SiO <sub>2</sub>	2–5	
Cristobalite	SiO <sub>2</sub>	2–5	
Potassium aluminium silicate	KAlSiO <sub>4</sub>	0.5–2	

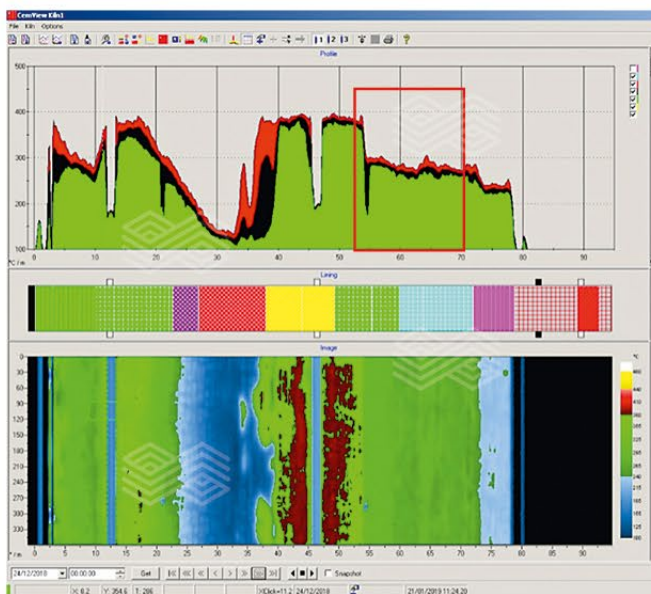
The kiln shell thermal scan (Figure 5) shows the installation in the safety zone in its third campaign, after more than 2.5 years in operation. The shell temperature in this area was in the range of 300 °C. This fits very well to the results of the theoretical heat transfer calculations (see Figure 2). The lifetime of previous installations has already been exceeded with RESISTAL S60IS and recent shell temperatures indicate that the lining is still in good condition.

### Sewage Sludge

The use of AFs with a high residual moisture can have unexpected results, which was experienced in another instance. In this case, the cement plant fired mechanically dewatered sewage sludge (MEKS) with a water content of 70%, where the material was fed into the inlet chamber. The kiln is a suspension preheater kiln with a 5.2-metre diameter, a length of 80 metres, and a daily capacity of 3000 tonnes. The brick sample investigated below (Figure 6) was taken from metre 7, measured from the kiln inlet, where unusually high wear was observed for this lining area after only 1 year of operation. The respective area was lined with mullite bricks with an addition of 10 wt.% SiC. The observed wear was most severe at the kiln inlet, resulting in a residual thicknesses of 150 mm (original thickness 220 mm). The wear became less significant with increasing distance from the inlet, reaching about a 190 mm residual thickness in the area 15 metres from the inlet.

**Figure 5.**

Thermal kiln shell scan of a rotary kiln (running metres on the x-axis, temperature on the y-axis). The location of the RESISTAL S60IS in the third year of operation is shown (red boxed area).



As previously described [2], the short lifetime of the mullite bricks with 10 wt.% SiC can be attributed to the combination of chemothermal load from the alkali salt infiltration and subsequent alkali bursting, as well as the deep-reaching degeneration of the brick structure caused by steam exposure. SiC is not resistant to steam and in the presence of water vapour, corrosion of SiC takes place. Therefore, it was recommended to use silica-sol impregnated products for this area, because of their alkali resistance and insensitivity to steam. The respective kiln area was lined with RESISTAL SK60CIS (now RESISTAL S60IS-IN). Figure 7 shows a sample from the respective area after 2 years in operation.

**Figure 6.**

Cross section of the used mullite-based brick sample containing 10 wt.% SiC taken 7 metres from the inlet. The sample showed a residual thickness of 170 mm. C1, C2, and C3 indicate samples for chemical analyses and A1, A2, and A3 indicate samples for mineralogical investigation.

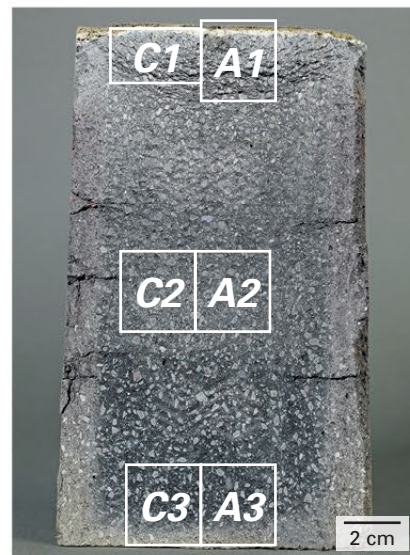


**Figure 7.**

Cross section of RESISTAL SK60CIS (now RESISTAL S60IS-IN) after 2 years in operation. C1 indicates sample for chemical and mineral phase analyses.



Table III.

Chemical and mineral phase analyses of a cement rotary kiln mullite-based brick sample containing 10 wt.% SiC from running metre 7. C1, C2, C3, and data sheet analysis of unused brick. On ignited sample (1050 °C) by X-ray fluorescence analysis (1), on original sample (2), total silicon content originating from SiO<sub>2</sub> and SiC given as SiO<sub>2</sub> (3), and ICP-OES optical emission spectroscopy by inductively coupled plasma (4).

General information				
Aggregate	Cement rotary kiln			
Installation area	Inlet zone			
Brick type	Mullite based with 10% SiC			
Position	7 meters from kiln inlet			
Sampling	5–20 mm from hot face	75–100 mm from hot face	145–170 mm from hot face	Data sheet
Chemical analysis	Wt.%	Wt.%	Wt.%	Wt.%
Loss on ignition (1050 °C) <sup>2)</sup> (DIN 51081)	0.23	0.00	-0.16	
Determination by XRF <sup>1)</sup> (ISO 12677)				
MgO	0.50	0.30	0.29	
Al <sub>2</sub> O <sub>3</sub>	51.91	54.53	54.38	57.00
SiO <sub>2</sub>	37.69 <sup>3)</sup>	40.14 <sup>3)</sup>	40.08 <sup>3)</sup>	28.50
P <sub>2</sub> O <sub>5</sub>	0.15	0.16	0.16	
CaO	0.44	0.46	0.48	
TiO <sub>2</sub>	2.11	2.20	2.22	2.50
Fe <sub>2</sub> O <sub>3</sub>	1.33	1.43	1.42	1.80
Determination by gas-volumetric analysis <sup>2)</sup>				
SiC	3.00	4.91	6.38	10.00
Determination by element-analysis <sup>2)</sup> (DIN 51085)				
SO <sub>3</sub>	0.05	0.05	0.37	
Total carbon content	1.09	1.92	2.10	
Residual carbon content	0.19	0.45	0.19	
Determination by ICP-OES <sup>2,4)</sup> (DIN 26845)				
Na <sub>2</sub> O	0.06	0.07	0.08	
K <sub>2</sub> O	3.21	0.02	0.00	
Determination by titration <sup>2)</sup> (DIN 26845)				
Chloride	0.00	0.00	0.00	
Phase analysis by x-ray diffraction <sup>2)</sup>				
Mineral phase	Formula	Wt.%	Wt.%	Wt.%
Mullite	Al <sub>6</sub> Si <sub>2</sub> O <sub>13</sub>	> 50.0	> 50.0	> 50.0
Corundum	Al <sub>2</sub> O <sub>3</sub>	10.0–50.0	10.0–50.0	5.0–10.0
Silicon carbide	SiC	2.0–5.0	2.0–5.0	5.0–10.0
Amorphous		5.0–10.0	5.0–10.0	5.0–10.0
Cristobalite	SiO <sub>2</sub>	0.5–2.0	5.0–10.0	2.0–5.0
Rutile	TiO <sub>2</sub>		0.5–2.0	0.5–2.0
Sillimanite	Al <sub>2</sub> SiO <sub>5</sub>	0.5–2.0	0.5–2.0	0.5–2.0
Quarz	SiO <sub>2</sub>		0.5–2.0	0.5–2.0
Leucite	KAISi <sub>2</sub> O <sub>6</sub>	10.0–50.0		

The result of the investigations (Table IV) revealed a strong supply of alkali salts; mainly potassium chloride with a strong potassium surplus. This finally led to the formation of leucite and the well-known alkali bursting effects.

Despite the consistently high chemothermal load, the lining life was doubled from 1 to 2 years. This can be attributed mainly to the application of the silica-sol impregnation technology instead of using SiC-containing bricks.

**Table IV.**

Chemical and mineral phase analyses of a cement rotary kiln andalusite-based brick sample. On ignited sample (1050 °C) by X-ray fluorescence analysis (1), on original sample (2), high temperature combustion infrared detection technique by LECO (3), calculated from the result of the sulphur determination (4), and ICP-OES optical emission spectroscopy by inductively coupled plasma (5).

General information		Cement rotary kiln	
Aggregate			
Brick type	RESISTAL SK60CIS (now RESISTAL S60IS-IN)	RESISTAL SK60CIS (now RESISTAL S60IS-IN)	
Sample number	3	Data sheet	
Installation area	Inlet zone		
Sampling	5–20mm		
Chemical analyses	Wt. %	Wt. %	
Loss on ignition (1050 °C) <sup>2)</sup> (DIN 26845)	2.91		
Determination by XRF <sup>1)</sup> (ISO 12677)			
MgO	0.29		
Al <sub>2</sub> O <sub>3</sub>	54.6	58.0	
SiO <sub>2</sub>	33.7	38.0	
P <sub>2</sub> O <sub>5</sub>	1.23	1.5	
CaO	0.08		
TiO <sub>2</sub>	0.37	0.5	
Fe <sub>2</sub> O <sub>3</sub>	0.33		
ZrO <sub>2</sub>	0.49		
Determination by titration <sup>2)</sup>			
Chloride	2.52		
Determination by ion-selective electrode <sup>2)</sup>			
Fluoride (DIN 51084)	0.03		
Determination by C-S elemental analysis <sup>2)</sup> (DIN 51085)			
Carbon	0.030		
Sulphur	0.001		
SO <sub>3</sub> <sup>4)</sup>	0.000		
Determination by ICP-OES <sup>2)5)</sup> (ISO 26845)			
Na <sub>2</sub> O	0.08		
K <sub>2</sub> O	5.46		
V <sub>2</sub> O <sub>5</sub>	0.01		
Phase analysis by x-ray diffraction <sup>2)</sup>			
Mineral phase	Formula	Wt. %	
Corundum, syn	Al <sub>2</sub> O <sub>3</sub>	> 50	
Mullite, syn	Al <sub>6</sub> Si <sub>2</sub> O <sub>13</sub>	10–50	
Leucite, syn	KAlSi <sub>2</sub> O <sub>6</sub>	10–50	
Andalusite	Al <sub>2</sub> (SiO <sub>4</sub> )O	10–50	
Sylvite	KCl	5–10	
Sanidine	K(Si <sub>3</sub> Al)O <sub>8</sub>	2–5	

### Cooler Installation

An interesting comparison of silica-sol impregnated and standard bricks could be made in a cooler installation in a plant where the mix-up of grades during installation impressively showed the superior performance of silica-sol impregnated products. The similar look of the impregnated bricks and the standard bricks resulted in a mixed installation as shown in Figure 8a. The darker appearing bricks represent the impregnated products and the brighter ones the standard bricks. Already after 16 months a first difference in behaviour could be detected. The standard bricks already showed the first signs of corrosion and prewear, while the impregnated bricks still had an original hot face. The difference was even more striking after 38 months (Figure 8b) as the standard bricks revealed strong prewear, whereas the impregnated products had retained their original thickness.

### Coating-Repellent Properties

The coating-repellent properties of silica-sol impregnated products have previously been described in detail [3]. Another well-documented reference [4] was achieved in a lime rotary kiln, used for pulp and paper applications, which was suffering from severe ring formation caused by excess levels of sulphur and the formation of spurrite. The customer experienced problems of heavy ring formation from running metre 5–27, particularly in the area after the burning zone. Usually, bricks based on andalusite were used in this area throughout the entire burning zone. The usual running time of the kiln was approximately 3–4 months, with a maximum of 7 months. After that time, the kiln had to be stopped to remove the ring formations. The remaining open diameter was partially reduced to 300–700 mm in the area of heavy coating rings. To extend the lining life and prevent coating formation RHI Magnesita suggested the installation of 5 running metres of RESISTAL SK60CIS (now RESISTAL S60IS-IN) in the critical area (from running metre 22–27) of the kiln.

Besides extending the typical campaign length of approximately 3–4 months, the following targets were requested regarding the brick performance:

- The maximum thickness of coating (ring formation) on the refractory side should not exceed 250 mm after 4 months. This relates to a remaining diameter of 2785 mm.
- The maximum coating thickness on the refractory side should be 500 mm after 8 months. This relates to a remaining diameter of 2285 mm.

An inspection of the lining and the situation inside the kiln took place after 7 months in operation, immediately after the kiln had been stopped. The lining area of RESISTAL SK60CIS (now RESISTAL S60IS-IN) showed only minor coating formation of a few cm (Figure 9). The kiln area lined with standard andalusite bricks showed severe coating formation (Figure 10).

With the application of silica-sol impregnated alumina bricks in a lime rotary kiln, not only the problems of ring formation could be solved according to the defined targets, but also the lifetime could be increased significantly. The operation period achieved was 7 months and the kiln was only stopped because of necessary maintenance not related to ring formation, ensuring smooth operation and higher productivity.

According to the customer, the kiln can now be operated for 11 months without problems in relation to heavy ring formation in the areas using the silica-sol impregnation technology.

**Figure 8.**

Cooler installation. (a) Mixed installation of standard (bright) and silica-sol impregnated alumina bricks (dark) and (b) lining after 38 months in operation with strong prewear of the standard alumina bricks.

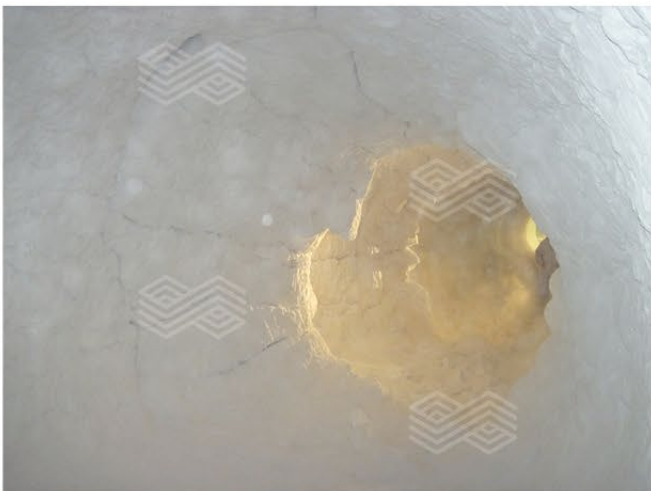


**Figure 9.**

RESISTAL SK60CIS (now RESISTAL S60IS-IN) bricks partially still visible under the thin coating layer.

**Figure 10.**

Severe ring formation in the adjacent area lined with standard andalusite bricks.



## Results/Conclusion

The impregnation of alumina bricks with silica sol significantly improves the alkali resistance and also prevents coating adherence. These properties are also known to be provided by SiC bricks; however, the advantage of silica-sol impregnation technology is that it does not increase the thermal conductivity associated with SiC addition, particularly for higher SiC contents of >10 wt.%. In addition, SiC is sensitive to steam, which can develop when firing AFs with a high moisture content. In contrast, the silica-sol impregnation technology is not affected by such environments. Therefore, it can be concluded that the impregnation technology offers the same benefits as SiC bricks without any of the disadvantages regarding shell temperature increases and/or reactivity with steam originating from certain AFs.

## References

- [1] de Beer, J., Cihlar, J., Hensin, I. and Zabeti, M. Status and prospects of coprocessing of waste in EU cement Plants, Date: April 26<sup>th</sup>, 2017.
- [2] Krischanitz, R., Jörg, S. and Fellner, M. Silicon Carbide Refractories – Not Always a Magic Bullet. *RHI Bulletin*. 2015, No. 2, 45–49.
- [3] Nievoll, J., Jörg, S., Dösinger, K. and Corpus, J. Sulphur, Spurrite and Rings – Always a Headache for the Cement Kiln Operator? *RHI Bulletin*. 2007, No. 2, 35–38.
- [4] Metzger, M. Internal Performance Reference and Case Study. 2013.

## Authors

Roland Krischanitz, RHI Magnesita, Vienna, Austria.

Susanne Jörg, RHI Magnesita, Technology Center, Leoben, Austria.

**Corresponding author:** Roland Krischanitz, roland.krischanitz@rhimagnesita.com



Erick J. Estrada O., Gerald Hebenstreit, Cesar Nader and René von der Heyde

# Development of an Upgraded Refractory Solution for Traveling Grate Induration Machine Combustion Chambers

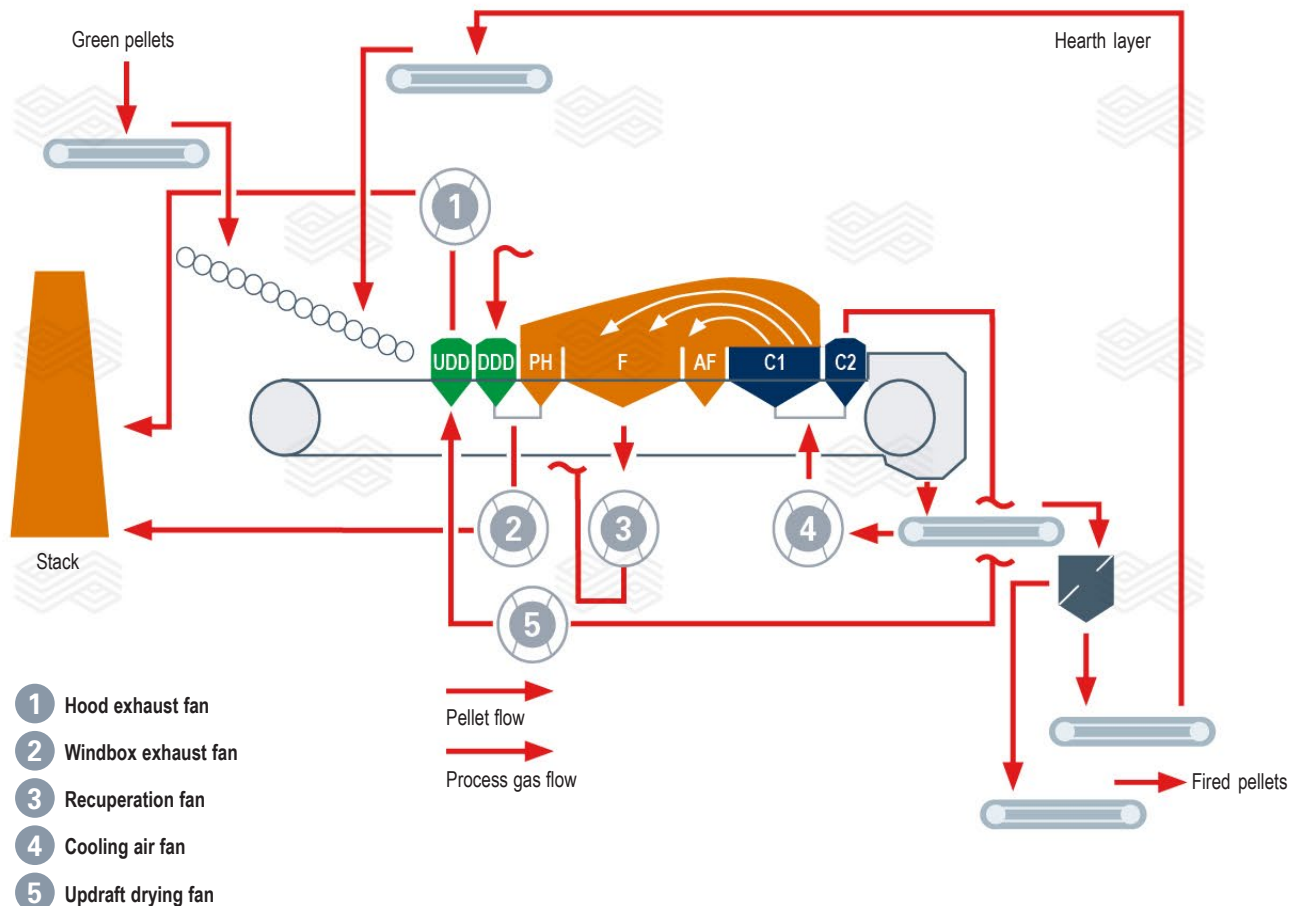
Iron ore pellets have become one of the most desired feeds for steelmaking processes. Due to their high iron content and excellent transportation properties, hardened pellets are a suitable high-purity, iron-rich feed material for direct reduced iron plants and blast furnaces. Although the available pellet induration technologies are slightly different, one of the best known is the traveling grate machine where state-of-the-art refractory lining concepts are required to withstand high temperatures in the firing zone areas, as well as resist extreme wear mechanisms and offer more reliable production processes. An upgraded lining concept for conical combustion chambers in the firing zone has been developed for induration machines with the objective of increasing performance and reducing shutdown periods; it comprises a novel refractory material grade and an optimized design that enables less complex installation with a fewer number of shapes.

## Introduction

For over a century, iron ore pelletizing processes have been emerging worldwide. Although there are different technologies available, the traveling grate machine is one of the most important and reliable equipment types for this production chain. Currently, the world's iron ore production exceeds 2100 million tonnes per year [1], demonstrating the remarkable importance of this process for downstream steel production. Once the iron ore extraction and concentration stages are complete, it is pelletized in a two-step process: Green pellet formation and induration [2]. In the first step, green pellets are generated from the very fine-grained raw material mixture on balling discs or drums, using a binding agent such as bentonite [3]. Subsequently, the green pellets are introduced into the traveling grate machine, where they are exposed to extremely high temperatures inside the firing zones (Figure 1).

Figure 1.

Traveling grate induration machine process flowsheet [4]. Abbreviations include updraft drying (UDD), downdraft drying (DDD), preheating (PH), firing (F), after-firing (AF), first cooling (C1), and second cooling (C2) zones.



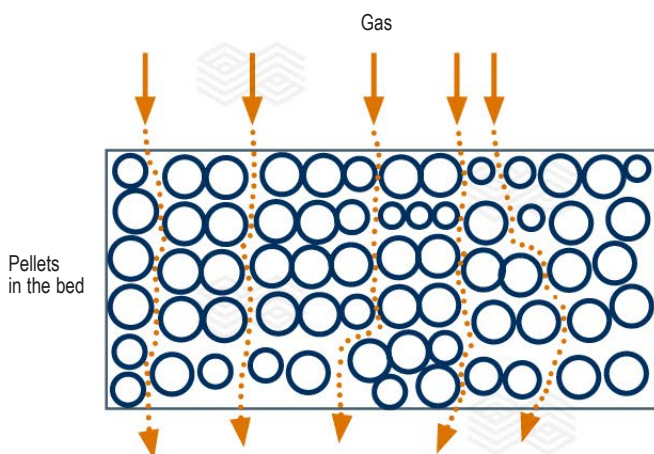
The furnace consists of grate cars on which the pellets are evenly distributed to form a multilayered bed. Horizontal movement of the cars then transports the pellets through various process stages, namely drying, preheating, firing, after-firing, and cooling. Processing gases pass through the pellet bed, resulting in iron-rich spherical balls with excellent mechanical resistance (Figure 2). As the pellets are then used in reduction processes, the mechanical resistance is an important property to cope with warehousing, transport, and high temperatures in the case of direct reduction shaft furnaces.

The most demanding areas inside the furnace are the firing and after-firing zones, where temperatures over 1400 °C can be reached, depending mainly on the equipment capacity, production rates, and fuel feeds. In these regions different refractory arrangements are used for the combustion chambers, side walls, baffle walls, and roof (Figure 3). For example, plastic mixes and fired bricks may be selected depending on the main design parameters such as the scheduled shutdown time, material and installation service budget, expected performance, and operating conditions.

**Combustion Chambers**

Most modern traveling grate furnaces have cylindrical shaped combustion chambers, primarily because natural gas is used as the main fuel type. For these cases, there are several arrangements and material technologies available with proven performance success. RHI Magnesita’s brands such as DURITAL E90 and DURITAL E92 are some of the best choices if the fired brick concept is selected. Furthermore, specialized technical and engineering teams are capable of developing customized solutions including specific shape designs, a reduced number of different shapes on stock, reduced mould requirements, and installation procedures.

**Figure 2.**  
Gas flow patterns through the pellet bed [2].

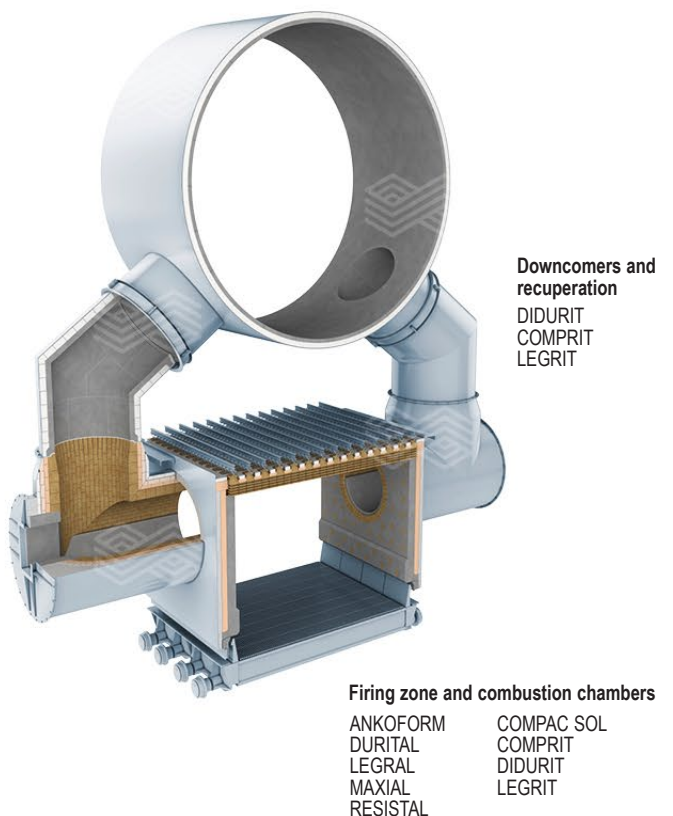


However, there are still a few furnaces that have conically shaped combustion chambers, an arrangement that may be linked to a technology development or even the fuel feed type. In the case of crude oil derivatives, conically shaped combustion chambers may be necessary to overcome fuel combustion residue adhesion to the refractory lining and to enable the scheduling of shorter cleaning times during operation. Additionally, in some cases iron ore dust may also travel from downcomers, generating severe build ups if no proper cleaning procedures are executed [5]. This condition may impact the overall refractory material performance, generating higher wear due to chemical attack of the refractory lining by clogged iron ore, including joint infiltration, among other common problems.

One of the main issues of conically shaped combustion chambers is the selection of the refractory installation method. Despite the possibility to use plastic, cast, or gunned mixes, higher performances are usually achieved with either bricks or precast materials. When selecting refractory materials, the available shutdown time and maintenance budget are primary factors to be taken into consideration.

Nowadays, owners of this type of furnace look for cost efficiency combined with high productivity and safety standards. Investment for refractory brick moulds can be significant, while precast materials require moulds that are usually cheaper and easier to produce. As heating schedules also vary, precast materials have become a suitable solution for this specific application.

**Figure 3.**  
Refractory lining examples for the firing zone.



## Development of a Tailor-Made Solution

In recent years, traveling grate owners have developed more reliable processes, including higher efficiency combined with cost effective actions. One of the main approaches to achieve such goals is optimizing the refractory lining. Therefore, an upgraded solution for conically shaped combustion chambers has been developed, including a novel refractory material and a design with fewer different shapes, having the main objective of achieving higher performance and lower shutdown times.

Multiple engineering hours were invested to develop a shape concept for conical combustion chambers. The goals included that each piece should weigh approximately 25 kg, thereby improving installation conditions for the service team, as well as an approximately 75% reduction in the overall number of different shapes, saving important costs regarding mould fabrication.

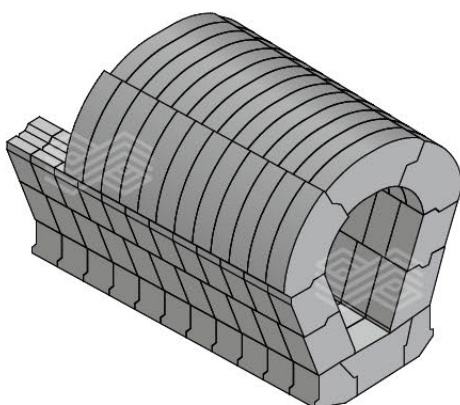
By combining RHI Magnesita's engineering team experience and currently available drawing software and 3D printing devices, it was possible to create a self-supporting combustion chamber refractory lining structure, with an upgraded centre of gravity concept, that should simplify on-site installation procedures (Figure 4).

When a precast refractory material is selected for any specific industrial use, it is possible to choose between drying or firing as the final heat treatment production step. Making the right refractory material selection for combustion chamber applications is extremely important to avoid unexpected failures due to the complex traveling grate machine configurations. For the presented case, a fired precast refractory material was developed, enabling guaranteed properties to be offered as the production occurs in a completely controlled environment.

The refractory industry continuously develops upgraded materials, offering all customers high-quality materials with operational safety. Specific combustion chamber applications are usually lined with high-alumina content materials, including fused alumina and fused mullite grain as the base raw materials.

**Figure 4.**

3D image of the developed shape concept.



Alternative complementary raw materials, such as spinel, have been widely investigated and discussed in recent years. There is evidence that MA-spinel may enhance mechanical properties such as the cold and hot modulus of rupture, as well as thermal shock resistance and slag corrosion resistance [6]. Previous RHI Magnesita research had shown that alumina MA-spinel precast materials may achieve excellent results when compared with typical fired fused mullite and sintered alumina bricks in terms of direct chemical attack by molten iron ore when evaluated using the rotary kiln slag test at 1650 °C. This test consisted of lining the furnace with the different brick types, heating the furnace until the desired temperature was achieved (i.e., 1650 °C), charging the furnace with 1.5 kg of slag material (i.e., iron ore), and rotating for 30 minutes. Subsequently, the residual slag was removed, the furnace was reheated, and then recharged with iron ore. This process was repeated for a total of 10 cycles before cutting and examining the bricks (Figure 5).

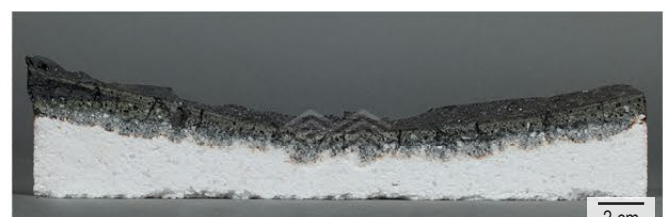
Traveling grate combustion chambers are constantly exposed to severe mechanical and chemical stresses during operation and the refractory lining is subjected to temperatures that may reach 1700 °C, in addition to chemical attack from the fuel and iron ore fines, abrasion from the gas flow, and thermal shock, among other factors. The developed ANKOFORM A93MAF-6 refractory material has MA-spinel and sintered alumina as the main raw materials, taking advantage of the enhanced properties provided by this microstructure to overcome such operational conditions. Precast pieces are produced using this low-cement castable, which after mixing is set in the required shape, cured, and finally fired in a tunnel kiln. Several tests were conducted to achieve an optimal formulation and firing schedule for this application.

**Figure 5.**

Comparison of (a) ANKOFORM MA-spinel precast material and (b) DURITAL E90 fired, fused mullite and sintered alumina brick grade after a rotary kiln slag test performed at 1650 °C using iron ore as the molten slag.



(a)



(b)

**Table I.**

Chemical and physical properties of ANKOFORM A93MAF-6.

Description	Temperature °C	Standard	Unit	Average Value
Al <sub>2</sub> O <sub>3</sub>	—	ISO 12677	%	93.00
SiO <sub>2</sub>	—	ISO 12677	%	0.10
CaO	—	ISO 12677	%	0.80
MgO	—	ISO 12677	%	5.60
Fe <sub>2</sub> O <sub>3</sub>	—	ISO 12677	%	0.10
Na <sub>2</sub> O	—	ISO 12677	%	0.20
Cold crushing strength	350	ISO 1927-6	N/mm <sup>2</sup>	160.00
Modulus of rupture	350	ISO 1927-6	N/mm <sup>2</sup>	10.00
Bulk density	350	ISO 1927-6	g/cm <sup>3</sup>	3.05
Open porosity	350	ISO 1927-6	%	16.00
Cold crushing strength	1350	—	N/mm <sup>2</sup>	110.00
Bulk density	1350	—	g/cm <sup>3</sup>	3.05
Open porosity	1350	—	%	16.00

ANKOFORM-A93MAF-6 has excellent mechanical properties as shown in Table I, which combined with the novel shape concept provides an alternative refractory solution for conical combustion chambers. In the future, it is planned to evaluate the benefits of this new development in an actual traveling grate iron ore induration machine.

## Conclusion

The various iron ore induration processes are constantly developing from a technical perspective, to improve plant safety, efficiency, and reliability. Recently, RHI Magnesita developed a novel refractory solution for conical shaped combustion chambers in traveling grate machines that provides safety improvements in terms of the weight of each refractory component, an important reduction in the number of different shaped pieces required, as well as a simpler installation procedure that should result in shorter shutdown times. In addition, the developed ANKOFORM-A93MAF-6 grade, based on MA-spinel and sintered alumina, has shown excellent mechanical properties after preliminary production trials and laboratory testing. To measure the gains of this new refractory development, further studies need to be conducted, including service trials to determine the on-site performance.

## References

- [1] World Steel Association. "World Steel in Figures 2020". 2020. pp. 20.
- [2] Vitoretti, F. and De Castro, J. Study of the Induration Phenomena in Single Pellet to Traveling Grate Furnace. *Journal of Materials Research and Technology*. 2013; 2(4). pp. 315–322.
- [3] de Moraes, S. L., Baptista de Lima, J. R. and Ribeiro, T. R. Iron Ore Pelletizing Process: An Overview. 2018. pp. 41–59.
- [4] Zhu, D., Pan, J., Lu, L. and Holmes, R. J. *Iron Ore Pelletization*. 2015. pp. 435–473.
- [5] Nader, C., Athayde, M., Marschall, H., Hebenstreit, G. and Wilhelmi, B. Refractory Applications in Iron Ore Pelletizing Plants—Travelling Grate Furnaces. *RHI Bulletin*. 2016. pp. 20–27.
- [6] Schacht, C. A. *Refractories Handbook*. 2004. pp. 215–258.

## Authors

Erick J. Estrada O., RHI Magnesita, Sogamoso, Colombia.  
 Gerald Hebenstreit, RHI Magnesita, Vienna, Austria.  
 Cesar Nader, RHI Magnesita, Belo Horizonte, Brazil.  
 René von der Heyde, RHI Magnesita, Mühlheim-Kärlich, Germany.  
**Corresponding author:** Erick J. Estrada O., erick.ospino@rhimagnesita.com



Andreas Viertauer, Nikolaus Mutsam, Franz Pernkopf, Andreas Gantner, Georg Grimm, Waltraud Winkler, Roman Rössler, Gregor Lammer, Alexander Ratz and Magnus Persson

# Refractory Lifetime Prognosis for RH Degassers

**This paper provides insights into the benefits of artificial intelligence (AI) applied for data analysis of a Ruhrstahl Heraeus (RH) degasser for secondary steelmaking. The main aim was to predict the refractory lifetime in the RH degasser by extracting information from the process parameters and model the impact on refractory material using machine learning techniques. The first step was to determine relevant process parameters by using feature selection methods. Those parameters were then used in a regression model to predict the wear of the degasser lining. In a second step, the process data was supplemented with the vessel shell temperatures, which were measured by an infrared (IR) based imaging system. The mathematical model for data processing and lifetime prognosis was designed to run in real time.**

## Introduction

In the steelmaking industry there is a demand for process optimization and predictability of the refractory lifetime, based on information recorded during the production process [1–3]. Recently, the volume of recorded data has been increasing dramatically. Therefore, machine learning is being exploited to determine useful information and the most influential parameters for modelling the production processes [4]. In this study, the aim was to predict the refractory lifetime based on data acquired during production. In total, 120 process parameters were preselected for building a statistical model to determine the influence on refractory wear.

The RH degasser vessel consists of two snorkels, connected to the vessel at the bottom, and the so-called off-take, mounted at the top (Figure 1). All parts are lined with different refractory grades [5,6]. The vacuum pump system is connected after the offtake. The vacuum treatment time is defined as the duration between submersion (dip in) and removal (dip out) of the snorkels into the melt, varying from 15–45 minutes, depending on the steel grade.

In addition to steel refining, the following operation modes of the RH degasser are:

- Vessel preheating.
- Holding the RH vessel under hot condition.
- Vessel internal deskulung with either an oxygen or natural gas burner.
- Snorkel maintenance (e.g., deskulung and gunning).

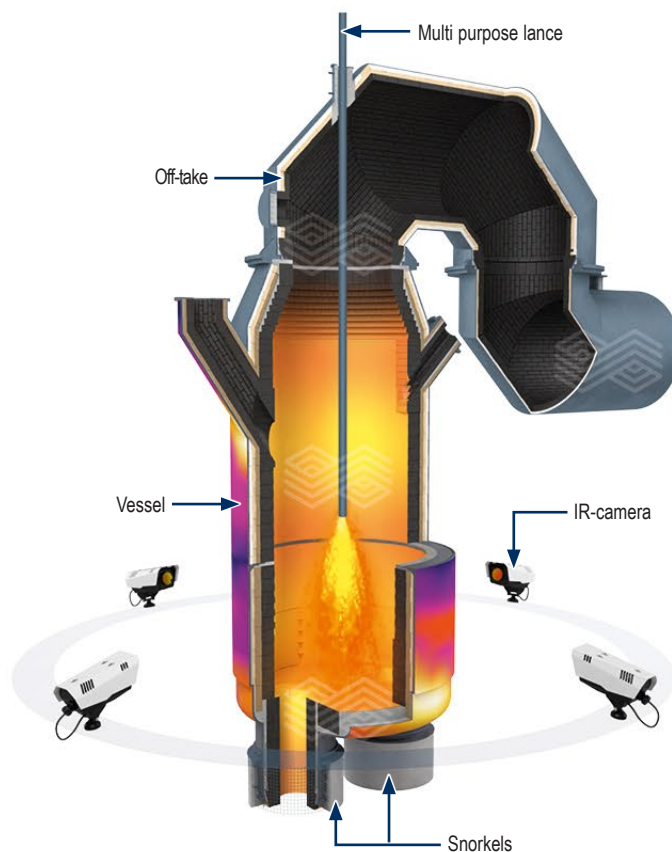
A significant number of papers have described the RH degasser process and lining configurations in more detail [7–10].

Currently, lifetime prognosis for the refractories is based on operational experience and close cooperation with the in-house refractory department and refractory supplier. Most steel plants experience unplanned shutdowns with uncoordinated sequence aborts, leading to low productivity at higher costs due to poor predictability of the refractory lifetime. The demand for RH-treated steel grades has been rising continuously for different reasons, which requires that the production runs stably with high plant availability. One of the main tasks to support this challenge is the monitoring of the refractory lifetime, which is especially important for the operation of a single-type RH degasser, as a vessel change takes at least several hours.

To gain a high and predictable refractory lifetime, the aim was to determine the main influencing factors for refractory wear and to build a statistical model for predicting the refractory condition. These arguments were the motivation for voestalpine Linz (Austria) to initiate this project on one of the four RH degassers.

**Figure 1.**

**Main parts of a RH-degasser during vessel preheating with IR-camera installation.**



## Data Processing

The data processing pipeline for predicting refractory wear is shown in Figure 2. It uses methods from machine learning to determine the conditions of the lining based on residual thickness measurements, steel shell temperature, and process parameters. The aim was to predict the wear and lifetime of the working lining. Furthermore, the most influential production parameters responsible for the wear of the lining could be determined. Understanding the influence and correlation of process parameters helps to identify causes for unwanted process anomalies and incidents.

As shown in Figure 2 there are three data sources used for the analysis.

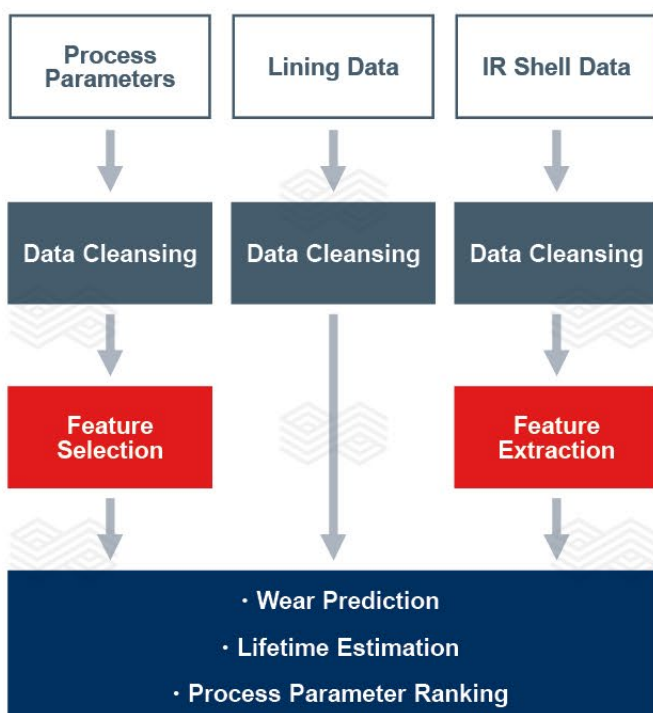
## Process Data

During each treatment, 120 preselected process parameters were recorded such as temperatures, consumptions, durations, chemical composition additions, and lift gas rates. As for the lining measurements, these process parameters require preprocessing and data cleansing. The most important process parameters for wear prediction were determined automatically through a feature selection stage as discussed below.

## Lining Data

The lining data provides the initial lining thickness and additional lining repair information. Furthermore, at the end of a vessel life campaign, the remaining lining thickness was measured manually as shown in Figure 3.

**Figure 2.**  
Processing pipeline for wear prediction.



These measurements represent the minimal lining thickness for each of the 20 brick layers and 8 segments per layer of the lower part of the vessel sidewall. Additionally, the bottom lining thickness was also measured. Several prediction models were created for areas with large wear rates, which are called hot spots (HS).

## Data for IR Vessel Shell Temperature

Four infrared (IR) cameras were installed for 24/7 online monitoring of the lower vessel shell temperature [11]. Figure 4 shows the lower vessel shell and temperature curves of four regions of interest over time. The aim was, in addition to preventing potential shell breaches, to model the relationship between the temperature changes during treatments and the thickness of the residual lining. This information provides a possibility to indirectly measure the current lining thickness. As an intuitive approach, the temperature gradient during a treatment was considered to determine the lining thickness. As shown in Figure 4, the gradients of the four temperature curves behaved differently than expected. This may have been caused by thermal radiation emitted by the hot steel in the ladle beneath and reflected on the vessel surface. Currently, this is subject of further research.

## Preprocessing and Cleansing

A regression model cannot be applied directly to data containing missing features. Furthermore, data samples which deviate extremely from the usual values, often referred to as outliers, can harm model training and therefore impair prediction accuracy. Hence, data

**Figure 3.**  
Sketch of the measurement procedure at the vessel wall.

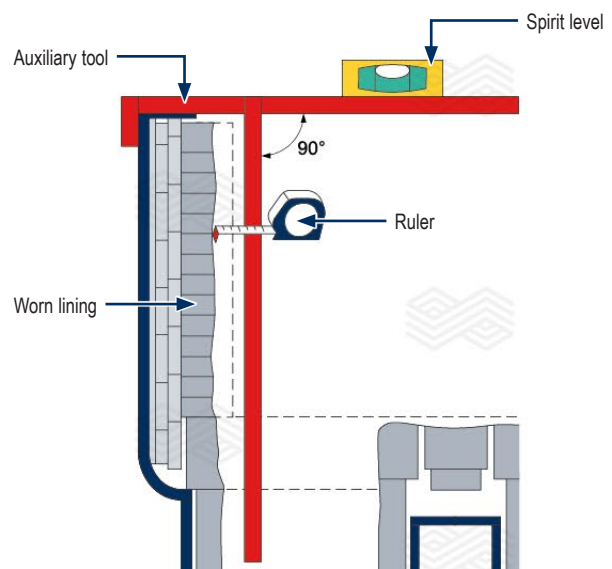
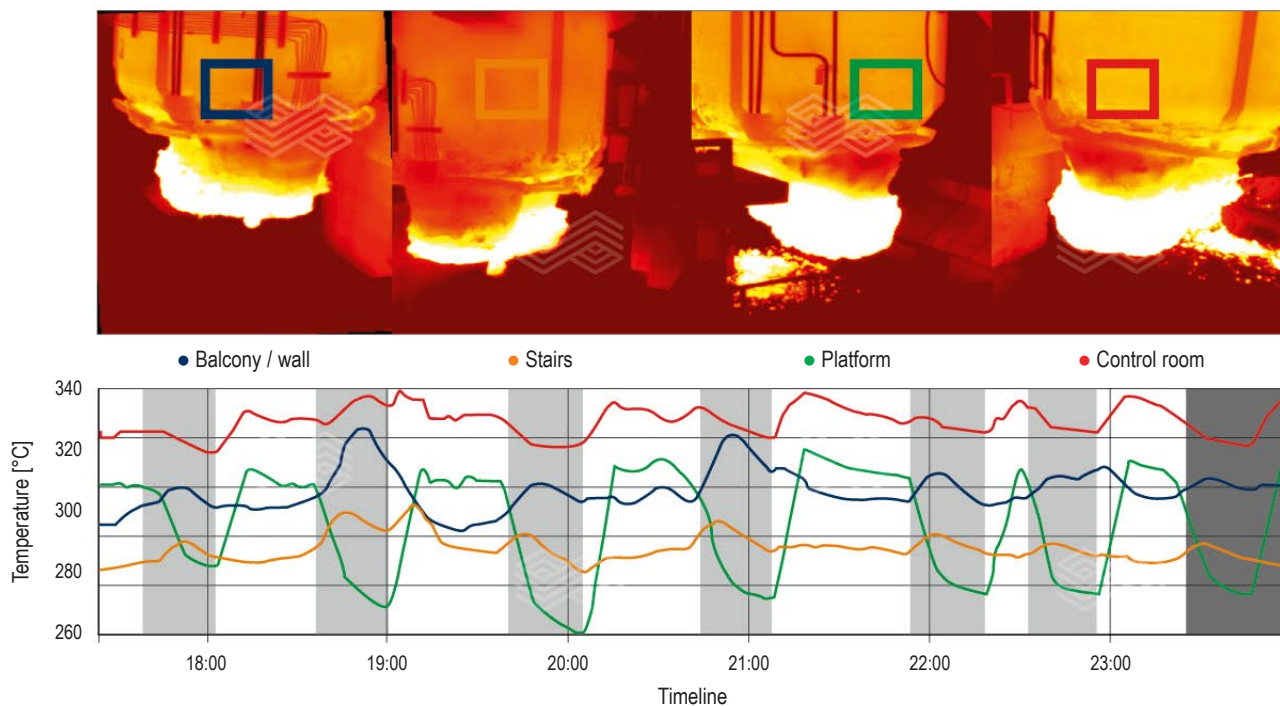


**Figure 4.**

IR images of the vessel shell and temperature evolution of the preselected areas, situated at approximately 90° intervals.



preprocessing and cleansing is necessary in many applications. This is especially important in cases of small data sets, where discarding incomplete samples or samples containing anomalies results in the loss of a significant portion of the available data. Replacing missing values with a guess or estimate is known as imputation—an excellent summary is provided in [12]. Applying imputation techniques completes the data set for any conventional regression method. Outlier detection and feature imputation must be treated with extreme care, so that important information is neither lost nor blurred. In this study, a combination of rule-based and nearest neighbour imputation was used to complete the available data. More details on data cleansing and imputation for this application are provided in [3].

### Refractory Modelling and Prediction

A statistical model for predicting the wear rate can be determined by regression analysis. In classical regression the target value  $t$  is continuous and the model input are the selected process parameters  $x$ . In this case, the target  $t$  was the maximum wear rate in the specified HS region, namely the maximum of the refractory wear of the HS normalized by the campaign length. The regression model was a function mapping from the input  $x$  to the target value  $t$  as  $t=f(x)$ . Furthermore, the aim was to exploit only the most influential process parameters  $x$  in the regression model. Therefore, these parameters were automatically determined by feature selection algorithms.

### Feature Selection

A sequential feature selection method was used, which was computationally efficient, but may result in a suboptimal feature subset of process parameters. Specifically, sequential forward floating selection (SFFS) was used [13]. This algorithm determines a feature subset which optimizes the evaluation criterion  $J$ . The cross-validated root mean square error (RMSE) of the regression model was used as the evaluation criterion  $J$ . The SFFS algorithm has the advantage that the floating mechanism enables the rejection of already selected features. This partly avoids nesting [13].

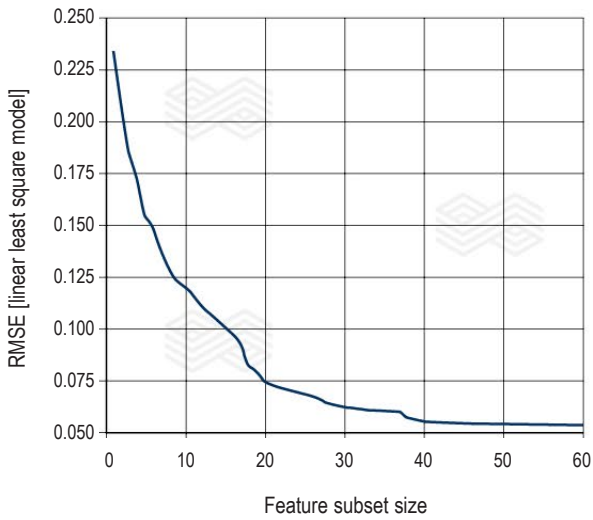
Figure 5 shows the cross-validated RMSE  $J$  of the regression model for a feature subset size from 1 up to 60 (x-axis). When using the best 10 features in the regression model, namely a feature subset size of 10, a RMSE lower than 0.125 was obtained for the wear rate. When using a feature subset size of ~40 parameters, the best regression performance was obtained.

In summary, feature selection provides a list of the most influential and helpful features for the regression model.

### Results and Discussion

For the lifetime prediction, 32 RH degasser campaigns were recorded over more than a year. The campaign length, namely the number of treatments, varied from 60 up to 200. In total, approximately 5000 data samples (i.e., treatments) were the basis and 14 selected features (process parameters) were used for the regression model. Results for the HS of the wall inlet are reported. A linear regression model was used for predicting the wear for each treatment.

**Figure 5.**  
Sequential forward floating selection (SFFS).



All reported regression results use 32-fold cross validation (CV), namely the regression model was trained on 31 campaigns and the model performance was reported on the remaining campaign. These 31 campaigns were also used for feature selection, where the feature subset was determined using the evaluation criterion  $J$ . Again,  $J$  is determined by 31-fold CV. This means that for the training data of each of the 32 folds, we obtain a feature subset.

Figure 6 shows the frequency of the selected features over all 32 folds.

The 14 features with the largest frequency in Figure 6 were used in the linear regression model, namely the features over the 32 folds were finally fixed to these 14 features (process parameters). Figure 7 shows the measured and the predicted wear for all 32 campaigns (x-axis) using the linear least squares (LS) regression model. The largest absolute prediction error for the wall inlet HS of the RH degasser was ~ 50 mm.

**Figure 6.**  
Frequency of selected features over 32 folds.

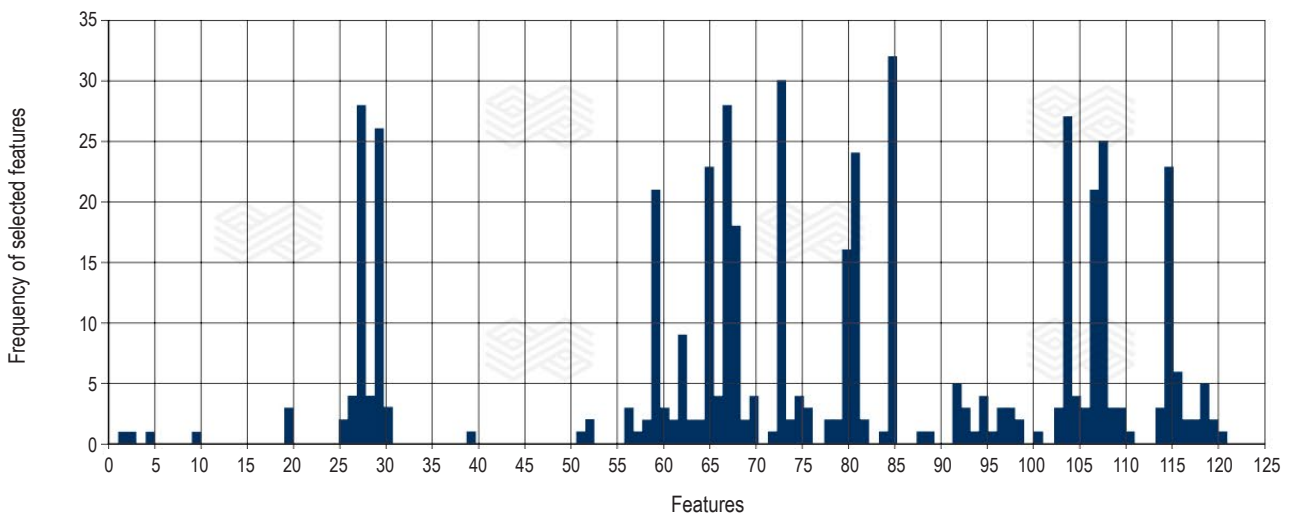


**Figure 7.**  
Measured and predicted wear in [mm] for 32 campaigns for the wall inlet HS, based on 14 process parameters.

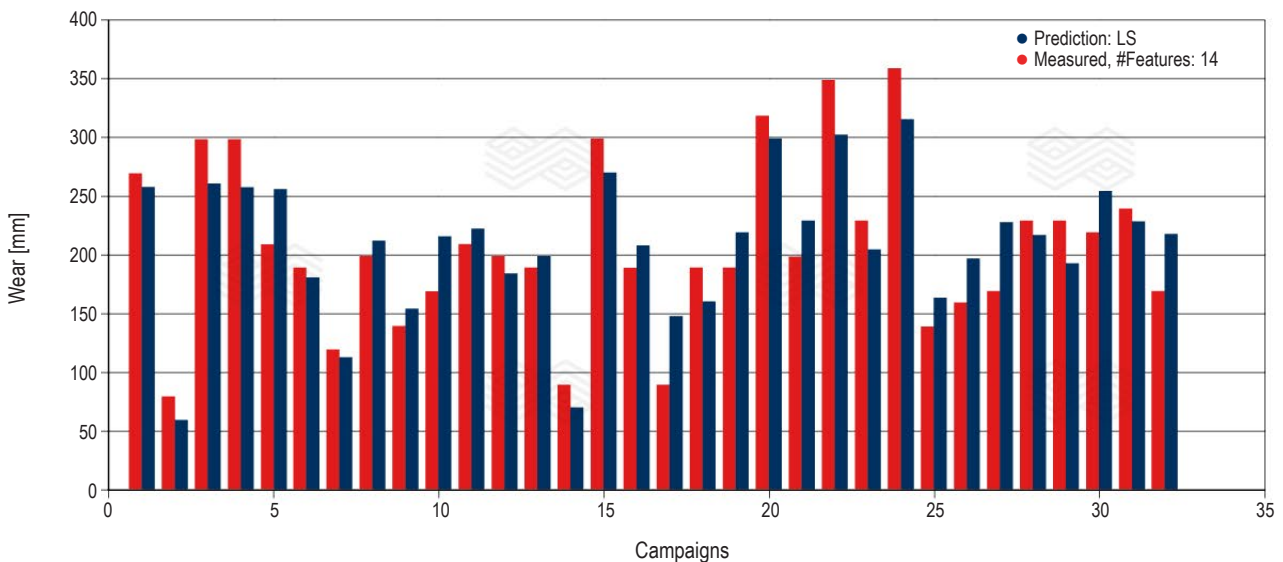


Figure 8 shows campaign number 4 as an example in more detail. In particular, the increase in wear is shown over the campaign length (number of treatments). The red mark is the measured wear at the end of the campaign. For this campaign, the regression model has an absolute error of ~43 mm.

### Online Lifetime Prediction

The developed regression model is used for online prediction of the refractory wear.

In particular, the process data is provided on a daily basis as input data for the lifetime prediction model, currently running as a local software client. Figure 9 shows an example of a prediction for a HS. The remaining brick length computed by the regression model (y-axis) at the current treatment 132 (x-axis) was ~170 mm. The original brick length was 350 mm. The grey line shows the prediction for future treatments. The intersection of the grey line with the minimum remaining brick length of 50 mm (red line) determines the number of remaining treatments, namely 93 additional treatments can be performed in this case.

**Figure 8.**  
Refractory wear over number of treatments for campaign number 4.

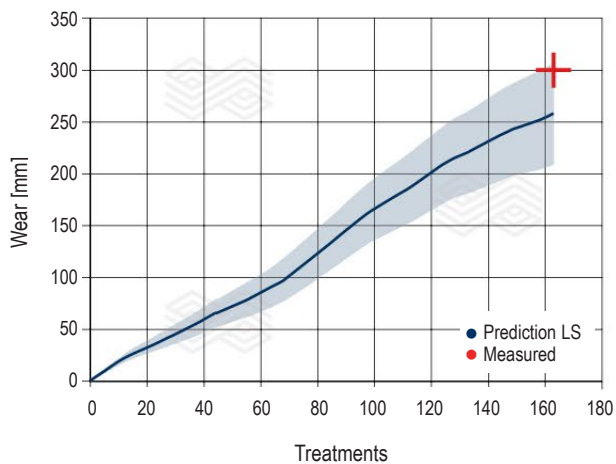


**Figure 9.**  
Prediction of the remaining brick length over the number of treatments.

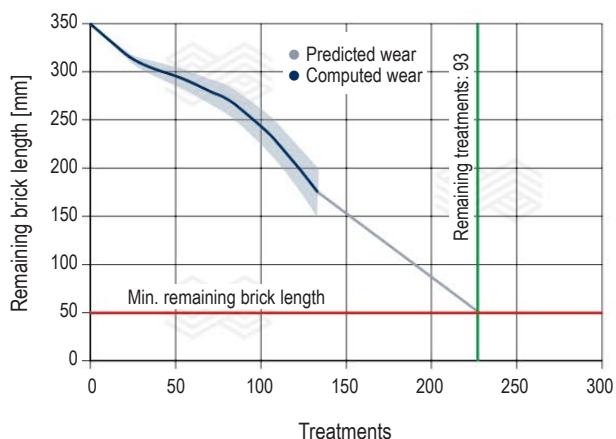


Figure 10 shows the flow of the process data which is sent by mail on a daily basis. This data is updated and processed in the so-called automated process optimization (APO) system. The updated lifetime prediction is sent as a daily report back to the customer.

The daily report includes statistical parameters of the current campaign as well as the prediction of the remaining brick length for several HSs of the RH degasser. After a finished campaign, the remaining lining thickness measurements for the bottom and wall of the lower vessel are also displayed in the report, together with overall campaign key values. An example of a campaign summary report is shown in Figure 11.

### Conclusion and Outlook

The refractory lifetime prognosis presented in this paper is currently based on the preselected process parameters of a RH degasser and the residual lining measurements taken after use. A third data source, the vessel shell temperature, was logged but not integrated into the model. Temperature and process data were recorded 24/7 over the whole campaign for the RH degasser number 3 at voestalpine Linz.

We demonstrated that a refractory wear model can be trained on the underlying data. Furthermore, reliable and automated wear prediction and the determination of the number of (remaining) treatments is possible with an accuracy better than 25 mm for most campaigns. The largest absolute prediction error for the wall inlet hot spot of the RH degasser was approximately 50 mm. A report including the predictions as well as the most important process parameters is provided to the customer on a daily basis. Modelling the relation between shell temperature and residual lining thickness should further improve the prediction accuracy and reliability and is the subject of ongoing research work.

We are grateful for the beneficial cooperation with voestalpine Linz GmbH. A part of the paper was published at the UNITECR 2019 [14].

**Figure 10.**  
Implementation overview of the online lifetime prediction using APO.

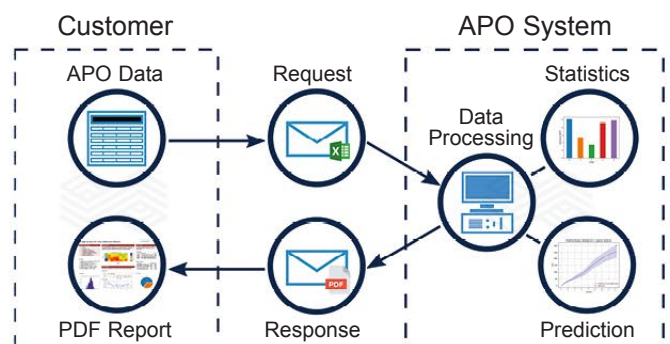
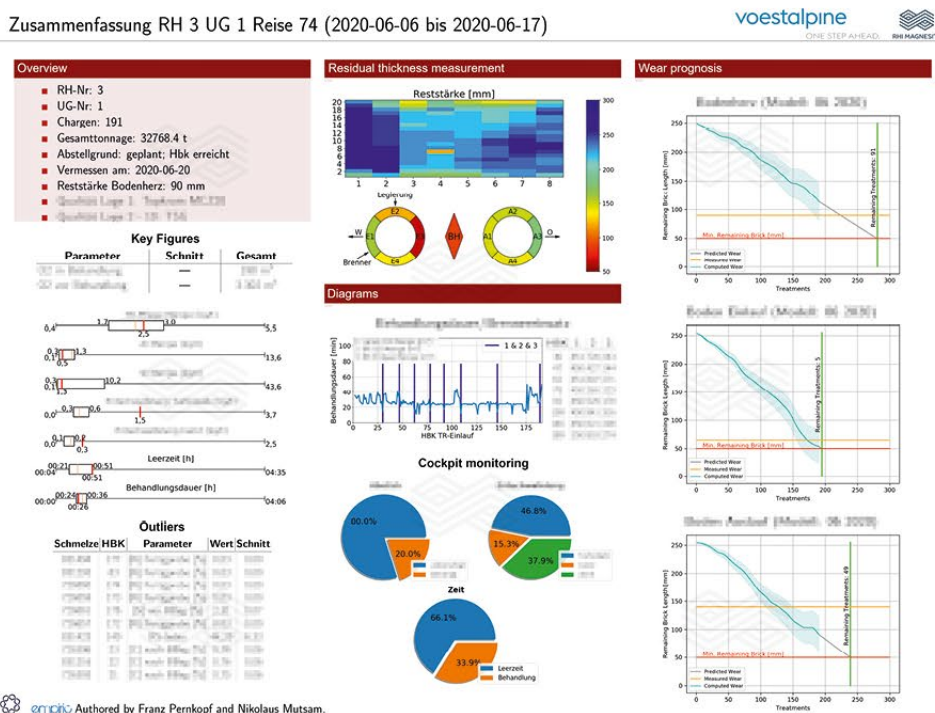


**Figure 11.**  
Campaign summary report.



## References

- Steiner, R., Lammer, G., Spiel, C. and Jandl, C. Refractories 4.0. *BHM*. 2017, 162, 11, 514–520.
- Lammer, G., Lanzemberger, R., Rom, A., Hanna, A., Forrer, M., Feuerstein, M., Pernkopf, F. and Mutsam, N. Advanced data mining for process optimizations and use of A.I. to predict refractory wear and to analyze refractory behaviour. Presented at AISTech 2017, Nashville, USA, May 2017, 1195–1207.
- Viertauer, A., Mutsam, N., Pernkopf, F., Gantner, A., Grimm, G., Winkler, W., Lammer, G. and Ratz, A. Refractory condition monitoring and lifetime prognosis for RH degasser. Presented at AISTech 2019, Pittsburgh, USA, May 2019, 1081–1087.
- Pending Patent. Method for determining the condition of a fire-resistant lining of a metallurgical melting vessel applications EP 2 789 960 A1.
- St-Jacques, A., and Heiligenbrunner, M., Improved concave lining design for the bottom of RH degassers. *RHI Bulletin*. 2013, 01, 41–44.
- Winkler, W., Exenberger, R., Grimm, G. and Gantner, A. Development of RH-degassing lining concepts at voestalpine Stahl Linz – an overview. Presented at the 14<sup>th</sup> Biennial Worldwide Congress UNITECR, Vienna, Austria, September 2015, Proceeding No. 272.
- Fruehan, R. J. Vacuum degassing of steel. iron and steel society. 1990, Warrendale, P.A.
- Pezza, A., Buehler, W.-A., Martinez Cerezo, J.-D. and Reising, M. Vacuum plant metallurgical results. *Stahl und Eisen*. 2018, 138, 1, 31–41.
- Gantner, A., Egger, M.-W. and Lehner, J. Experiences with the new secondary metallurgy No. 3 at voestalpine Stahl Linz. Presented at the 6<sup>th</sup> European Oxygen Steelmaking Conference, Stockholm, Sweden, September 2011, 384–392.
- Tembergen, D. Sekundärmetallurgische Prozess Technik, *Metallurgie der RH-Anlage*. VDEh Stahl Akademie, Krefeld, Germany, March 2014, 24–26.
- www.rhimagnesita.com/agellis/steel-making-solutions/Visir FurnaceSafe, accessed 03.02.2020.
- Maimon, O. and Rokach, L. Data mining and knowledge discovery handbook. *Springer US*, 2010, vol. 1.
- Pudil, P., Novovičová, J. and Kittler, J. Floating search methods in feature selection. *Pattern Recogn. Lett.* 15, 11 1994, 1119–1125.
- Viertauer, A., Mutsam, N., Pernkopf, F., Gantner, A., Grimm, G., Winkler, W., Lammer, G., Ratz, A. and Persson, M. Refractory lifetime prognosis for RH degassers. Presented at 16<sup>th</sup> Biennial Worldwide Congress UNITECR, Yokohama, Japan, October 2019, 155–157.

## Authors

Andreas Viertauer, RHI Magnesita, Vienna, Austria.  
 Nikolaus Mutsam, Mutsam Engineering, Graz, Austria.  
 Franz Pernkopf, Graz University of Technology, Graz, Austria.  
 Andreas Gantner, voestalpine Linz, Austria.  
 Georg Grimm, voestalpine Linz, Austria.  
 Waltraud Winkler, voestalpine Linz, Austria.  
 Roman Rössler, voestalpine Linz, Austria.  
 Gregor Lammer, RHI Magnesita, Vienna, Austria.  
 Alexander Ratz, RHI Magnesita, Vienna, Austria.  
 Magnus Persson, RHI Magnesita, Agellis, Lund, Sweden.  
**Corresponding author:** Gregor Lammer, [gregor.lammer@rhimagnesita.com](mailto:gregor.lammer@rhimagnesita.com)

Patrick Seitz, Yong Tang and Gerald Nitzl

# Refractory Tubes with Innovative Liner Technology for Flow Control and Clean Steel Applications

Ladle shrouds (LS) and submerged entry nozzles (SEN) are flow control products used in continuous casting which transfer the liquid steel from the ladle to the tundish and further to the mould. Due to the strongly different and quickly changing temperature conditions before and during steel casting, highly thermal shock resistant refractory materials are required which simultaneously save steel process energy. A new technology embeds a special liner into the refractory body inner surface to reduce the heat transfer through the LS/SEN wall. To better understand the function of this insulation layer a mathematical model was applied. Temperature measurements carried out in the steel plant were compared with the simulation results. The research results indicate potential heat loss reduction and performance improvements in the steelmaking process.

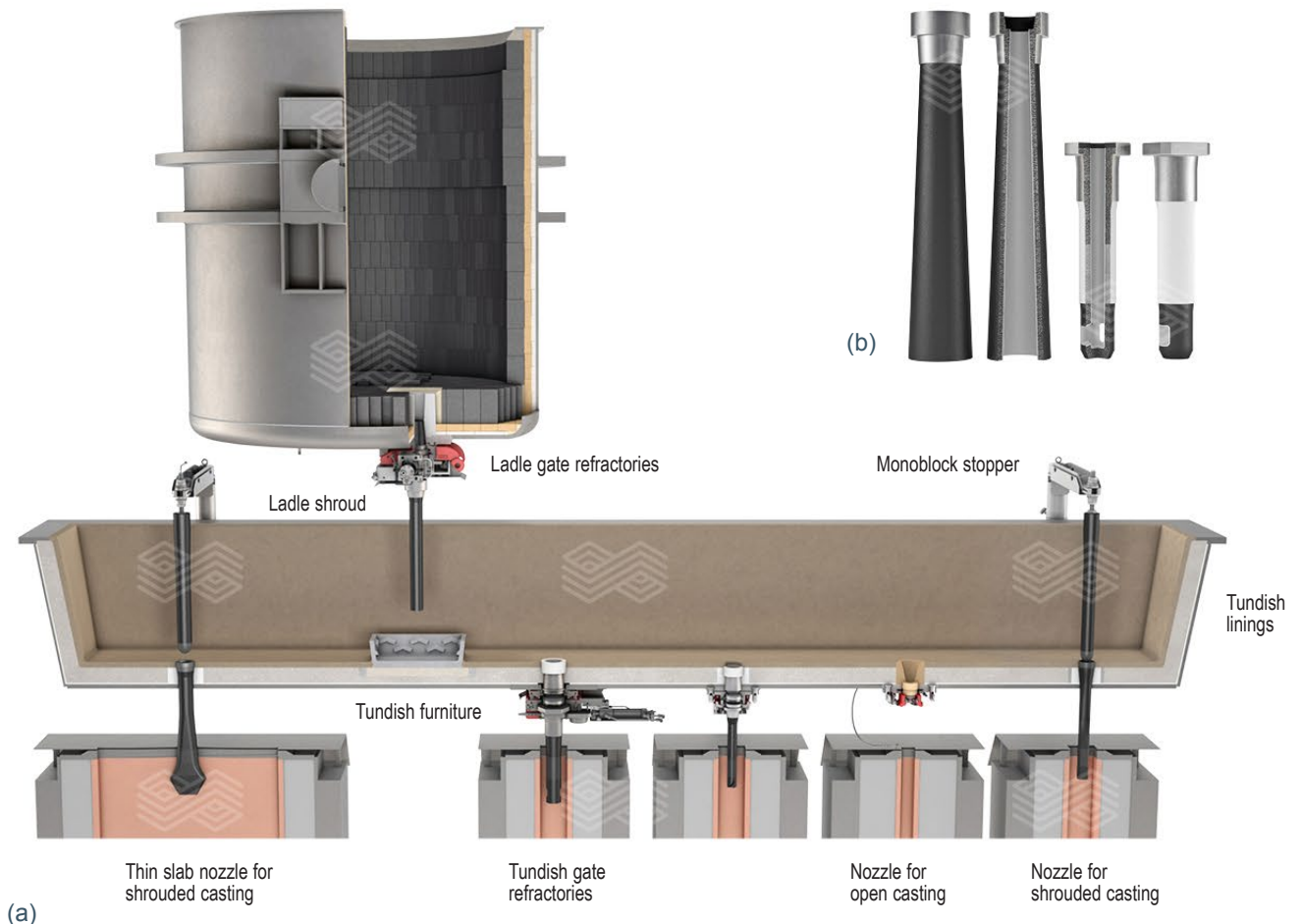
## Introduction

Flow control products such as ladle shrouds and submerged entry nozzles are used in the steel continuous casting process to transfer the molten steel from the ladle to the tundish and then into the mould, protecting the molten steel stream from reoxidation. Most flow control products are isostatically pressed (ISO) from carbon-bonded refractories, which need to resist high temperatures, corrosive attack of steel and slags, and high temperature gradients during the application.

Figure 1a illustrates the flow control products used in the steel continuous casting process, where the steel is transferred from the ladle to the mould. Figure 1b shows an example of a LS and SEN equipped with a liner material inside the product bore.

Figure 1.

(a) Isostatically pressed products for flow control applications and (b) ladle shroud and submerged entry nozzle showing the liner material inside.



For better thermal shock resistance the carbon content of flow control products is rather high, at 20-30 wt.%, which also results in a high thermal conductivity of these products. Consequently, some measures have been used to minimize the heat losses through the refractory walls. RHI Magnesita has developed special liner materials that are applied inside the product bore with improved insulating properties for LS and SEN to achieve this goal.

The development of this new liner technology includes two steps and the following advantages [1]:

#### New manufacturing process

- To produce well-defined liner thicknesses.
- To be able to manufacture non-parallel sections in nozzles (i.e., port section).
- Scalable process required for small and large geometries.
- More consistent wall thickness of liner compared to conventional decarburized layer.

#### Materials with customized properties [5–10]

- Carbon-free
- Anti-clogging
- Erosion-resistant
- Heat insulating

Figure 2 shows the liners of a LS (left) and SEN (right), (i.e., white coating). The LS requires a liner with a length of more than 1000 mm. The SEN has the liner on the nonparallel sections in the port area.

In order to study the insulating performance of this innovative liner, computational fluid dynamics (CFD) simulations and industrial measurements were performed.

#### CFD Simulations

According to the operating conditions, two-dimensional (2D) simulations were used for LS and SEN [2]. The 2D simulation for the thermal transfer investigation provides an accurate model since most heat losses are transferred through LS and SEN walls in a radial direction.

**Figure 2.**

Cut products showing the liner; see white coating in the bore.



The difficulties in obtaining accurate results for this type of simulation lie with the boundary conditions; namely exact thermal data of the materials during the casting process. All the material properties used in the simulation were measured or calculated under laboratory conditions which may be different from the real casting conditions.

For example, in practice the decarburized layer of a standard LS becomes thinner during the casting process, which influences the thermal insulation properties. The boundary conditions are also one important factor influencing the accuracy of modelling. The current simulation assumes ideal conditions such as the interfaces of the layers are in perfect contact; no infiltration in the refractory materials; the ladle shroud and submerged nozzle are fully filled with liquid; no gas is involved in the steel stream in the tube. Steady state calculation was used to obtain the thermal situation of the LS and SEN during the stable casting process.

#### Simulation of Ladle Shroud

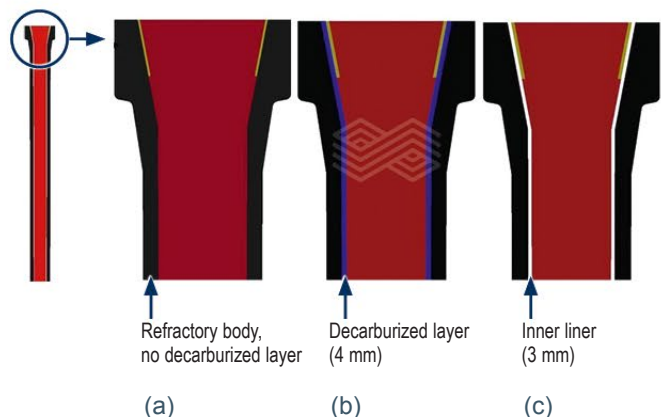
An axisymmetric domain was used for the 2D simulation of the LS shown in Figure 3. In application, the LS is used without any preheat while transferring molten steel from the ladle to the tundish. To achieve high thermal shock resistance, a decarburized layer is formed inside the LS during the production process. However, in many cases this decarburized layer is not stable during the application.

In extreme circumstances, this decarburized layer can be totally removed by the steel flow. Thus, in this simulation an extreme case without a decarburized layer was also considered (No decarburized). A stable decarburized layer (4 mm thick) and a stable liner (3 mm thick) were the other two simulation cases. The lower thermal conductivity and respectively higher insulation property of the liner compared to the decarburized layer enables a lower thickness.

The simulation uses conjugate heat transfer. Since the flow in the tube is highly turbulent, a very fine boundary layer was used to resolve the turbulent behaviour near the wall. The first row mesh size of the boundary layer was 0.2 mm.

**Figure 3.**

Ladle shroud geometry and simulation cases, (a) LS not insulated, (b) decarburized, and (c) liner.



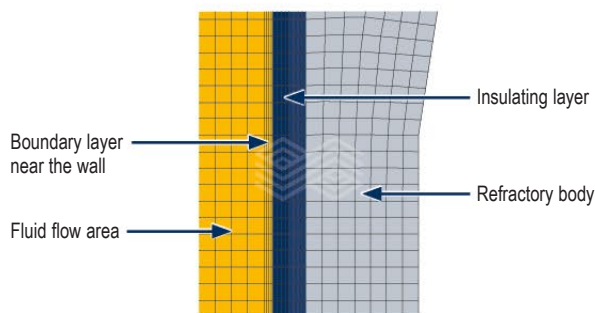
The mesh quality criteria  $y^+$  on the tube wall was less than the criteria value of 30, which ensured enough accurate heat transfer simulation between the turbulent flow and the tube inner surface wall. A standard  $k$ -epsilon turbulence model was applied. Figure 4 shows parts of the grids used in the domain. The mesh size of the grids was approximately 2 mm.

The boundary conditions for the LS are shown in Figure 5. The heat transfer coefficient (HTC) between the free air stream and the refractory wall was based on experience. The liquid steel temperature at the inlet was 1500 °C and the mass flow rate was 2 tonnes/min. 2<sup>nd</sup> order upwind was applied for the numerical discretisation. The absolute convergence check criteria were  $1 \times 10^{-05}$  for continuity, velocity, and turbulence solving.  $1 \times 10^{-08}$  was used for the energy convergence check.

Figure 6 shows the temperature profiles of the LS for the three different cases mentioned above. The results indicate that with the liner, the temperature of the LS outer wall surface is more than 100 °C lower compared to the standard LS with an evenly formed decarburized layer. The liner can keep the surface temperature more than 400 °C lower than the standard LS when the decarburized layer is totally removed. Essentially, the liner technology has more capability to prevent heat loss through the LS wall than the standard LS with the traditional decarburized layer method.

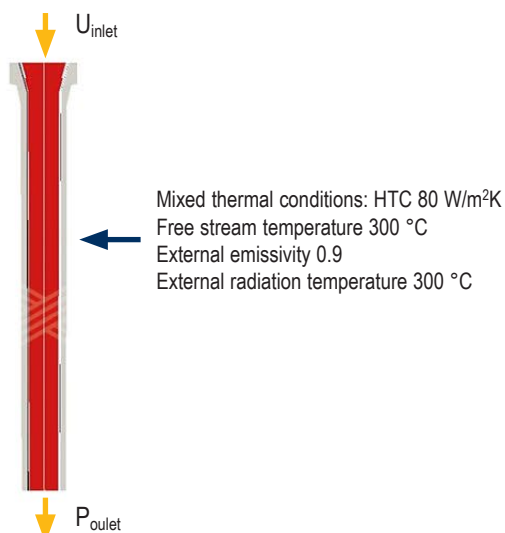
**Figure 4.**

Illustration of mesh used in the simulation.



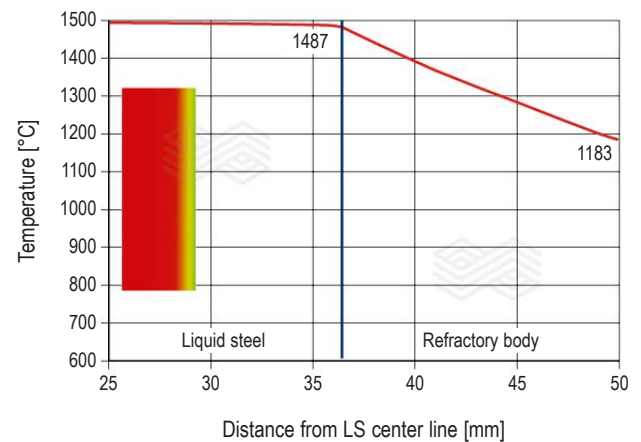
**Figure 5.**

Boundary conditions for LS simulation.

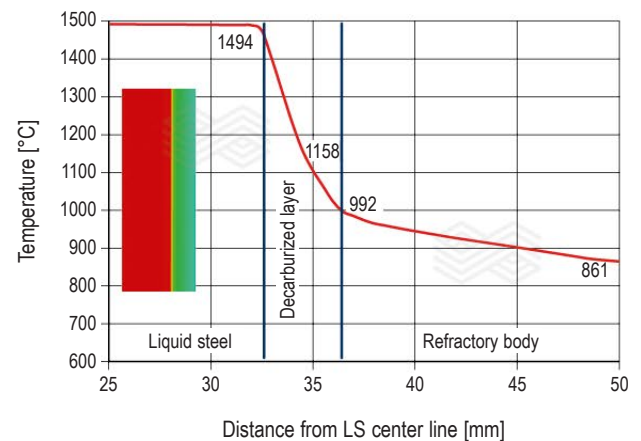


**Figure 6.**

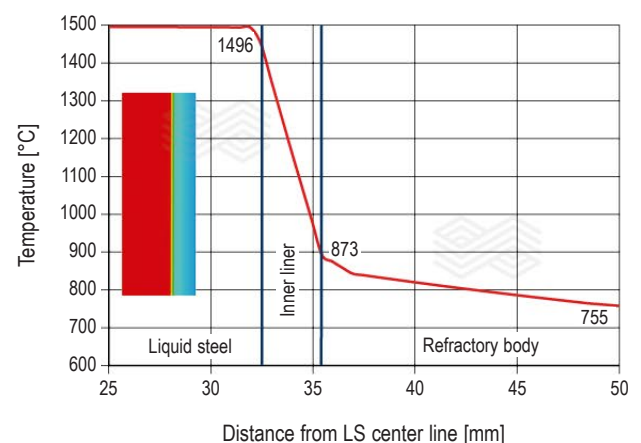
Temperature profile of LS. (a) No decarburized layer, only refractory body, (b) decarburized, and (c) liner.



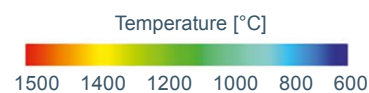
(a)



(b)



(c)



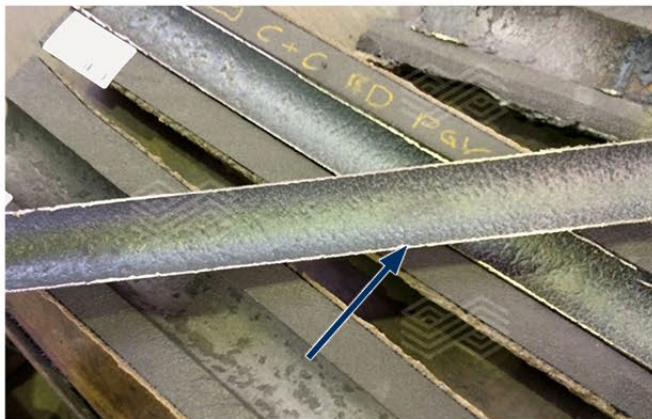
### Heat Losses in the Submerged Entry Nozzle

Another issue that can be observed during continuous casting is undesirable solidification of steel in the SEN. As shown in Figure 7, some solidification may occur during casting. This effect is mostly due to operational causes such as “cold steel”.

The worst-case scenario would be that the strand freezes completely during the start of casting. This phenomenon can also be observed within the sequence caused by badly stirred steel in the ladle. Such events usually cause high operational costs when the sequence needs to be aborted. In such cases, a SEN with liner improves operational safety by avoiding undesired solidifications of the liquid steel in the nozzle.

As there are often several different refractory materials used for the SEN production, the probability of cracking due to thermal shock can be avoided by using the liner. Furthermore, an improved and more homogenous insulating layer provides potential to improve the refractory materials used for the SEN wall such as the refractory wear resistance in the area of the mould flux.

**Figure 7.** Undesirable steel solidification in SENs. (a) Partial steel solidification in the bore and (b) total steel solidification (strand lost).



(a)



(b)

### Simulation of Submerged Entry Nozzle

The modelling setup for the SEN was similar to the LS. A 2D symmetric domain including a continuous casting mould (1560 x 200 mm) was used. The simulation's boundary conditions are shown in Figure 8.

As opposed to the LS, the outer wall surface of the SEN is normally coated with insulating fibre to avoid extra heat loss and protect the slag band material from thermal shock. Two simulation cases with and without a liner on the SEN inner surface (up to the end of the slag band) were carried out. Both cases considered the insulation fibre wrapped on the outer wall surface. The outer wall insulation was not considered under the meniscus level of the SEN since the insulating fibre was washed away during the long sequence casting process. The domains in the upper part of the SEN in the nonimmersed area of the two cases are shown in Figure 9.

**Figure 8.** SEN simulation boundary conditions.

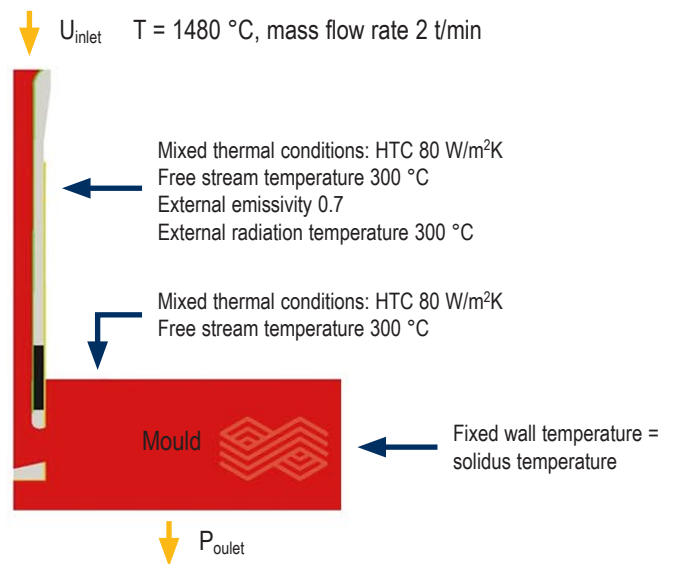
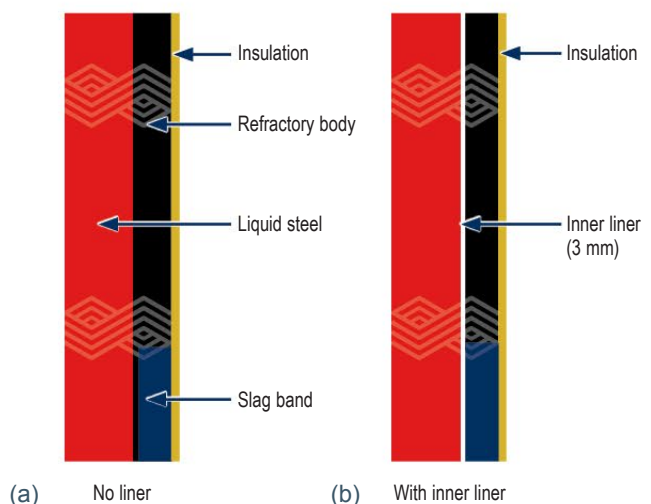


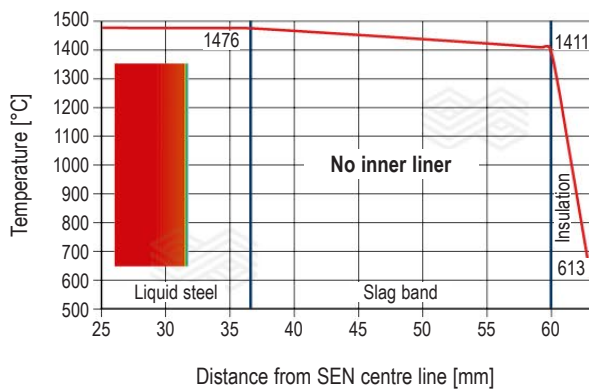
**Figure 9.** Simulation cases for upper part of the SEN. Nonimmersed area setup (a) without and (b) with liner.



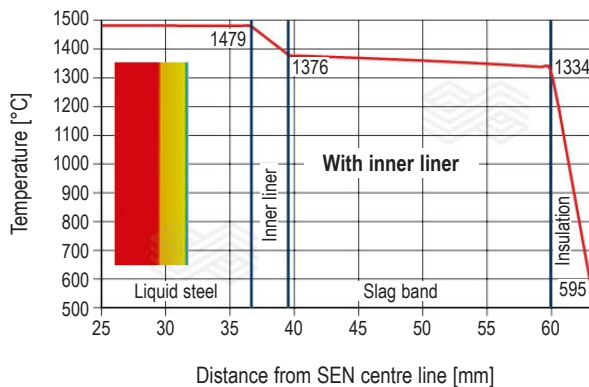
The simulation results comparing these two SEN cases are shown in Figure 10. The liner can reduce the temperature by about 20 °C on the SEN outer insulation surface. This small difference is due to the further insulating effect of the fibre coating on the outer side. When focused on the SEN outer wall temperature (before the insulation fibre), it is 1411 °C without liner and 1334 °C with liner. The temperature difference is about 70 °C. Nevertheless, the innovative liner technology can also help reduce the heat loss through the wall of the SEN.

Another interesting result was found in the temperature distribution near the continuous casting meniscus level. Figure 11 illustrates the temperature profile in the mould. The general thermal pattern is similar between these two cases. The only difference is near the SEN area at the meniscus level. As the liner can decrease the heat loss through the SEN wall, the temperature around the SEN area near the meniscus is lower when compared to the SEN without liner. This should be considered regarding the application of liner technology for the SEN. The lower temperature around the SEN near the meniscus level may increase the risk of mould flux bridging. One possible solution to avoid this bridging near the meniscus level is to apply the liner material only above the meniscus level.

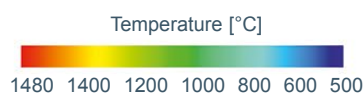
**Figure 10.**  
Temperature profile of the SEN (a) without and (b) with liner.



(a)



(b)



## Industrial Measurements

The LS and SEN products with and without liner were tested and compared in a steel plant. The measurements of the ladle shrouds and submerged entry nozzles surface temperature were carried out on site. The cast steel was stainless steel with a steel temperature in the ladle of about 1500 °C. The temperatures were measured differently. For the LS, a device using infrared technology was used, whereas a thermocouple was taken for the SEN to avoid the radiation impact of the fibre insulation during the measurement.

The measured positions were the middle area of the LS and the upper area of the SEN. Figure 12 demonstrates the temperature measurement on site for the LS (infrared technology) and SEN (thermocouple used).

**Figure 11.**  
The temperature distribution in the mould (a) without and (b) with liner material.

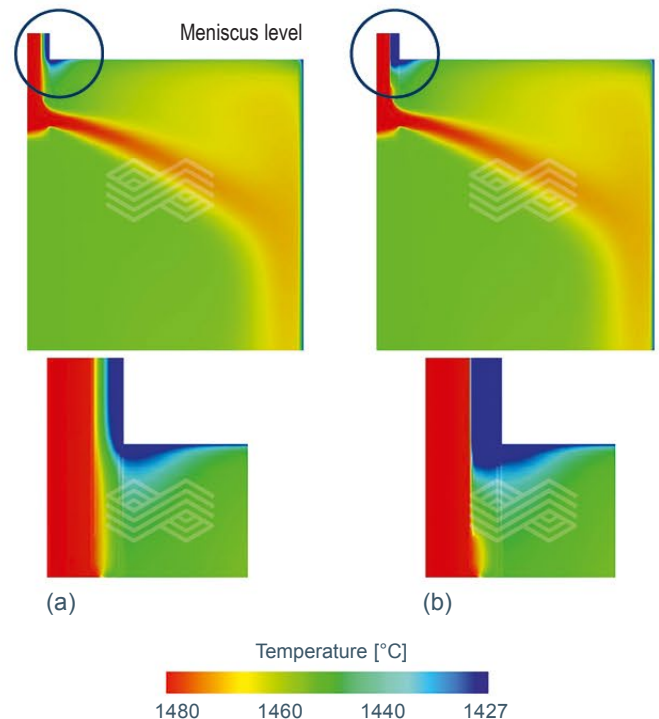


**Figure 12.**  
Surface temperature measurement of (a) LS and (b) SEN.



(a)

(b)

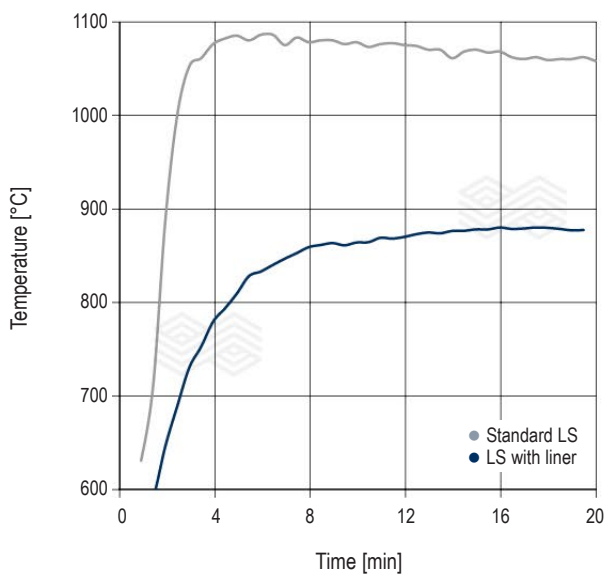
Figure 13 illustrates the LS surface temperature comparison between a standard LS without liner and a LS with liner under similar casting conditions. Also, the brightness of the LS outer surface was compared. The LS with liner was glimmering significantly less during casting and the brightness distribution was more homogenous compared to the standard LS, resulting in a more homogenous temperature distribution within the LS. When the trial prototypes were investigated after casting, no damage of the liner could be identified. Furthermore, the different temperature curves illustrated in Figure 13b show a significant difference in temperature increase indicating the LS with the liner is less exposed to risk of thermal shock due to the lower gradient of the curve. Furthermore, a temperature difference in the range of 200 °C was measured after the first minutes of casting.

**Figure 13.**

(a) Brightness difference between a standard LS (left) and a LS with liner. (b) Surface temperature of LS during casting with and without liner.



(a)



(b)

Both simulated and measured results show that the liner can reduce the temperature of the LS surface, indicating a decrease of heat loss through the wall. However, the LS surface temperature predicted by the simulation was 10–20% lower when compared to the measured value.

With the SEN, Figure 14 shows the surface temperature measured by the thermocouple in contact with the fibre insulation of the SEN during casting. The irregular pattern of the curves was caused by the connection and disconnection of the thermocouple due to fluctuation of the tundish and consequently the SEN.

Nevertheless, the results indicate that the liner can decrease the SEN outer surface temperature by around 100 °C although the decrease is smaller compared to the LS case. This conclusion also corresponds to the simulation results. The simulated results are also about 10–20% lower than the measured temperature data. Thermal conductivity and boundary conditions could be the reasons for this deviation.

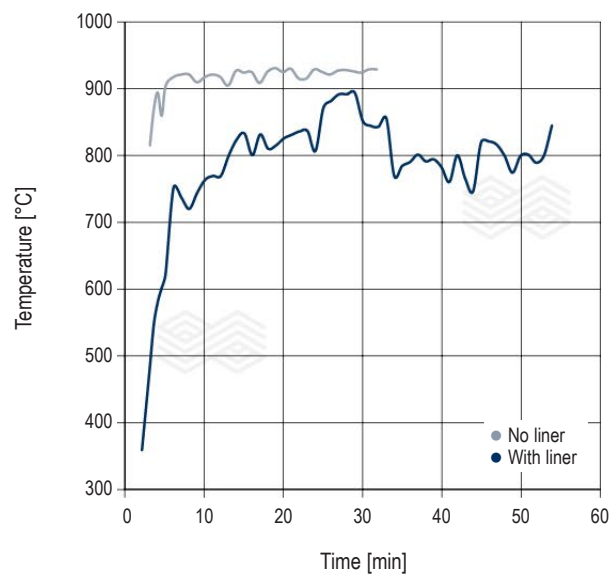
## Results/Conclusion

Newly developed liners for ladle shrouds and submerged entry nozzles used in continuous casting offer a wide range of technical, commercial, and economic benefits.

The field trial results showed that the liner was stable during casting and that the temperature distribution on the outer product surface was homogenous compared to the standard product. In addition, the liner did not show any damage after the casting process. Both simulations and measured results demonstrate that the liner can reduce the heat transfer through the LS and SEN walls.

**Figure 14.**

Surface temperature of SEN during casting with and without liner.



Based on production data of 2019 more than 10000 pieces have been produced (ladle shrouds, tundish, and sub entry nozzles) using the inner liner technology for six customers worldwide. A further five customers have been acquired for trials in 2020.

By using the liner technology, operational safety is improved by reducing the risk of strand losses due to undesired freezing of the strand. Furthermore, the inner liner technology can also be used for cold-start refractory tubes such as submerged entry shrouds. In addition, new developments of refractory materials to extend the refractory lifetime in critical areas are possible due to reduced heat flow and lowered risk of thermal shock at the start of casting.

From the energy saving perspective in the steel plant the potential for ladle and tundish shrouding with the innovative liner technology is theoretically in the order of 1–2 °C. The cost of energy is in the range of 0.03–0.10 €/t for 1 °C [3, 4]. This results in potential savings between 60–200 k€/million tonnes of steel cast.

Connecting material development and industrial application with novel simulation methods leads to a better understanding and will help to develop new refractory solutions for the continuous casting of steel.

## Acknowledgement

The authors are grateful to the steel plant SIJ Acroni d.o.o., Jesenice, Slovenia, for the support in the plant on this project.

## References

- [1] Nitzl, G., Seitz, P. and Tang, Y. Energy Saving Monolithic ISO Components for Flow Control and Clean Steel Application. Presented at the 59<sup>th</sup> International Colloquium on Refractories, Aachen, Germany, 2016, 210–213.
- [2] Tang Y., Hackl G., Nitzl, G., Seitz P. and Košir, A. Simulation and Industrial Measurement of Heat Transfer of Flow Control Products with Special Inner Liner. Presented at STEELSIM, Qingdao, China, August 2017.
- [3] Buhr, A., Bruckhausen, R. and Fandrich, R. The Steel Industry in Germany – Trends in Clean Steel Technology and Refractory Engineering, MARKETS&ECONOMY. *refractories WORLDFORUM*. 2016, 8.
- [4] Buhr, A. Energy Saving by Modern Raw Material Concepts, ALMATIS Kundenseminar Kaltenengers, 21 June 2016.
- [5] Akinari Sasaki, Katsumi Morikawa, Jyoki Yoshitomi High Durable Nozzle For Continuous Casting. Presented at EUROGRESS, Aachen, Germany, September 8<sup>th</sup> and 9<sup>th</sup>, 2010.
- [6] Tehovnik, F., Burja, J., Arh, B. and Knap, M. Submerged Entry Nozzle Clogging During Continuous Casting Of Al-Killed Steel, Published at METALURGIJA 54 (2015) 2, 371-374.
- [7] Svensson, J. K. S., Memarpour, A., Ekerot, S., Brabie, V. and Jönsson, P. G. Studies of New Coating Materials to Prevent Clogging of Submerged Entry Nozzle (SEN) During Continuous Casting of Al Killed Low Carbon Steels, *Ironmaking and Steelmaking*, 2017, 44, 2, 127.
- [8] Dorrer, P., Michelic, S. K., Kloesch, G., Reiter, J., Paul, A. and Bernhard, C. Study of Clogging Deposit Build-up in Al Killed and Ca-Treated High Sulfur Steels with Focus on the Steel/Refractory Interface. Presented at AISTech, 2017.
- [9] Dorrer, P., Michelic, S. K., Bernhard, C., Penz, A. and Rössler, R. Study on the Influence of FeTi-Addition on the Inclusion Population in Ti-Stabilized ULC Steels and Its Consequences for SEN-Clogging, published at steel research int. 2019, 90, 1800635.
- [10] Chen Tian, Jingkun Yu, Endong Jin, Tianpeng Wen, Danbin Jia, Zhenli Liu, Paixian Fu, Lei Yuan. Effect of Interfacial Reaction Behaviour on the Clogging of SEN in the Continuous Casting of Bearing Steel Containing Rare Earth Elements, *Journal of Alloys and Compounds*, 792, 5, 2019, 1–7.

## Authors

Patrick Seitz, RHI Magnesita, Technology Center, Leoben, Austria.

Yong Tang, RHI Magnesita, Technology Center, Leoben, Austria.

Gerald Nitzl, RHI Magnesita, Vienna, Austria.

**Corresponding author:** Patrick Seitz, Patrick-Paul.Seitz@rhimagnesita.com





## Tailor-made tundish-to-mould solutions INTERSTOP Robotics

The operation of Flow Control related products in the steel industry is still very challenging in terms of people's safety and process reliability. The interaction with the production facilities exposes the operator to significant risks.

For this reason, we developed a fully automated solution for a monotube change designed to be handled by a robot. The robot enables the monotube to be changed automatically during casting. Furthermore, a preheating station as well as a powder lance tool ensure a reliable and holistic solution for our customers.

Curious to find out more details?  
Visit [rhimagnesia.com/interstop/automation-robotic](https://rhimagnesia.com/interstop/automation-robotic)

Follow us



RHI MAGNESITA

Bernd Trummer, Christian Manhart and Wolfgang Fellner

# Vibrational Determination of Gas Purging Regime and Efficiency in a Water Model and Validation by a High-Speed Camera

**Gas purging is an important tool in modern secondary metallurgy. Inert gases are introduced into the steel melt through purging plugs. Although significant process know-how has been accumulated over the years, only little is known about the effect of different purging plug designs on the purging behaviour. Vibration detection may offer a method of studying this influence allowing characterization of the purging behaviour of different plug designs on a quantitative basis. In this paper, the results of such a vibration investigation of a slot plug and a porous plug installed in a water model are presented. Clear differences between these two plug designs regarding the purging behaviour were detected and quantified.**

## Introduction

Inert gas purging is a prerequisite for state-of-the-art secondary metallurgy in steelmaking and has to support several process steps in ladle metallurgy with diverging process requirements [1]. Water model investigations have shown that slot and segment plugs have the best performance under high flow rates whereas porous plugs are very efficient for soft bubbling. Hybrid plugs are suitable for high as well as low flow rates [2].

All this knowledge has been gained in water model investigations, in industrial practice by visual examination, and via high-speed camera photos, as so far no alternative methods have been available to determine or even quantify the gas purging regime and efficiency reliably. Current industrial technology is using the gas flow rate as a control factor, which works very well for process control in established processes in steel mills. However, apart from obvious weaknesses like hidden leaks in the gas supply, there is also a general problem with this approach. The gas flow rate is not directly linked to the decisive physical phenomena of bubble size, bubble shape, number of bubbles, and frequency of bubble generation. Hence, no quantitative description of the actual purging process is possible. Consequently, no quantitative comparison of different purging plug designs is possible, hindering the controlling, recording, and evaluation of existing purging applications as well as the development of new and improved purging plug designs.

In recent years, the use of vibrational analysis in gas purging has been increasingly investigated [3]. It was shown that vibration signals were suitable for quantifying the purging in a gas stirred vessel even though some of the relationships were still unclear [4,5].

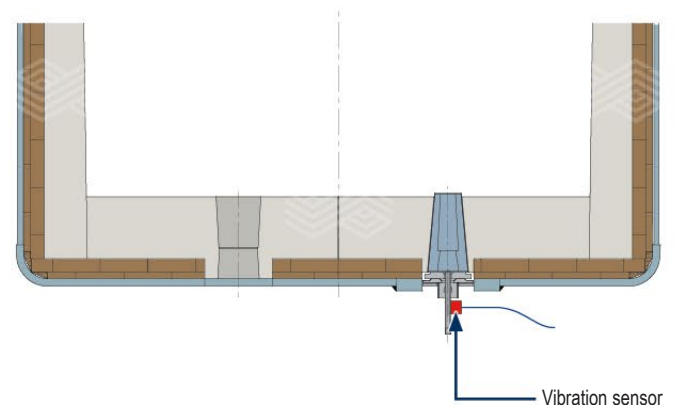
Corresponding patents [6] of companies working in this area suggest that industrial applications have also been considered for this vibration technology or have already been established [7] on a commercial basis. In all of these investigations, vibrational measurements were carried out by accelerometers mounted to the vessel walls determining vessel wall vibrations (e.g., ladle or water model) caused by the highly turbulent movement of the melt inside the vessel. So far, no investigations have been carried out to study vibrational patterns generated by the detachment of gas bubbles from the plug surface and the subsequent falling back of the melt onto the plug surface. Known for a long time to study back-attack effects [8], this method also seems to be very promising for a quantitative characterization of gas purging efficiency, especially for low gas flow rates. In such a setup, the accelerometer is not mounted to the vessel wall but to the connecting pipe of the purging plug.

This study presents the results of investigations on the vibrational patterns generated by slot and porous plugs in a water model at different flow rates and compares and validates vibrational patterns with visual examinations and high-speed camera photos.

## The Plug Vibration Detection Method

A new method for purging plug vibration detection and analysis has been developed based on vibrations generated by the bubble formation at the purging plug surface [9]. A schematic drawing showing the experimental setup of this method is given in Figure 1.

**Figure 1.**  
Schematic drawing of a steel vessel with purging plug and vibration sensor.



For this method, a vibration sensor is mounted to the connecting pipe of a purging plug, detecting mechanical waves running from the plug surface through the plug to the sensor. These mechanical waves are generated by the impact of the melt on the plug surface after the gas bubbles have detached from the plug surface and the melt falls back. For the vibration signal the normalized amplitude over the time is recorded in a vibration spectra, an example is given in Figure 2.

The acceleration  $x[t]$  is computed with the discrete Fourier transformation  $X[f]$  in a frequency spectrum [10].

$$X[f] = \sum_{t=0}^{N-1} x[t] e^{-j \frac{2\pi t}{N} f} \quad t = 0, 1, 2, \dots, (N - 1)$$

From the frequency spectra  $X[f]$  the bubble index component  $BI_n$  is calculated. This is done by summing over the frequency amplitudes  $X[f]$  within a predefined frequency range [a, b].

$$BI_n = \sum_{f=a_n}^{b_n} X[f] \quad n = 1, 2, \dots$$

**Figure 2.** Example of a vibration spectrum. The normalized acceleration  $x[t]$  in dependency of the time  $t$  is shown.

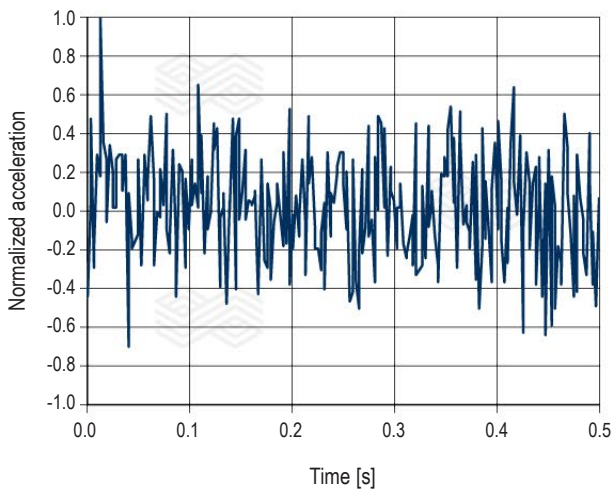
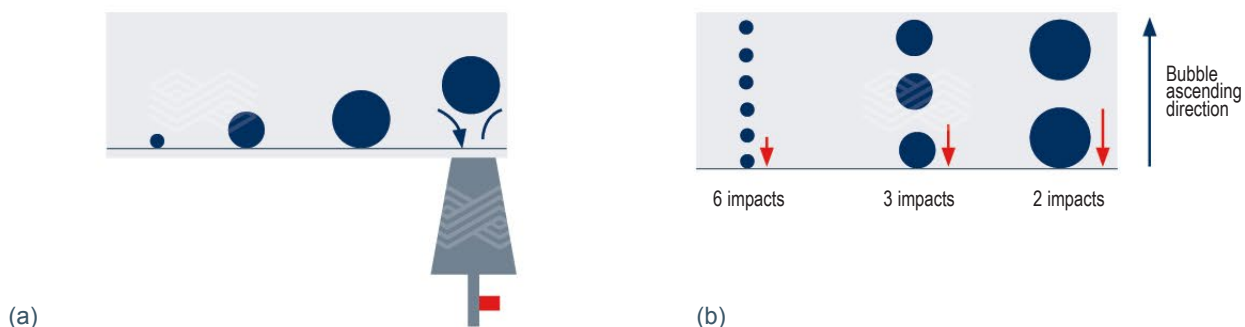


**Figure 3:** (a) Formation, growth, detachment of the bubble, and subsequent impact on plug surface and (b) influence of bubble size on number of impacts.



For a bubble distribution analysis procedure, the range of the frequency spectra  $X[f]$  is divided into a number of sub-ranges from low frequency values to high values. The frequency definitions are based on the plug type. In Table I an example of three frequency ranges of the bubble index  $BI_n$  calculation is shown. The sum of all three bubble indices for high, medium, and low frequency range is always 100%.

**Table I.** Example of bubble index  $BI_n$  frequency ranges.

Bubble index $BI_n$	Frequency Range $f_a, f_b$	
	$f_a$ [Hz]	$f_b$ [Hz]
$BI_1$	0	1000
$BI_2$	1000	2000
$BI_3$	2000	3000

The computed bubble index  $BI_n$  can be correlated with the gas flow through the purging plug and is used to characterize different types of purging plugs.

The basic idea behind this method is the following: When small bubbles are generated, a very high number of bubbles is necessary to consume the supplied gas volume. Small bubbles form faster and detach from the plug surface giving way to new bubbles. This process creates impacts at the plug surface with a very high frequency. In contrast, large bubbles consume the provided gas volume rather fast and only a small number of large bubbles evolve. These large bubbles form relatively slowly and detach from the plug surface and vibrations with a relatively low frequency are generated. At a given flow rate, the higher the cumulative amplitudes within the selected frequency range, the more impacts at the plug surface occur. This means a higher number of detaching bubbles from the plug surface. Hence, the amplitude of these frequency spectra can be correlated to the number of bubbles which formed. Vibrations within the highest/medium/lowest frequency band represent the content of small/medium/large bubbles as demonstrated in Figure 3.

**Table II.**

Geometric and physical characteristics of the slot and porous plugs examined in the water model investigation.

	Slot plug	Small porous plug	Large porous plug
Slot number	24		
Slot dimensions [mm]	16x0.25		
Porous part [mm]		Round, 120 mm cross section	Round, 210 mm cross section
Open porosity [vol.%]	12	27	27
Bulk density [g/cm <sup>3</sup> ]	3.1	2.6	2.6
Raw material basis	Al <sub>2</sub> O <sub>3</sub>	MgO	MgO

### Experimental Procedure

A slot plug with 24 slots (slot dimensions: 16 mm long and 250  $\mu\text{m}$  wide) and two round porous plugs of different sizes (one with a cross section of 120 mm and the second with a cross section of 210 mm) were installed in a water model. Details of the plug characteristics are given in Table II. The 1000-litre capacity water modelling tank was 1000 mm high. The plugs were fed with compressed air at ambient temperature by an INTERSTOP Inert Gas Purging System provided by RHI Magnesita. This system allows a precise adjustment and constant mass flow in the range of 0–1000 l/min. A digital high-speed camera was used to take images of the bubble plume during the water model experiments.

A vibration sensor (PCB Piezotronics 352C33, frequency range 0.5 to 10 kHz) was mounted to the connecting pipe of the plugs and vibration signals were recorded and processed by a conventional personal computer.

### Water Modelling Results

#### Slot plug

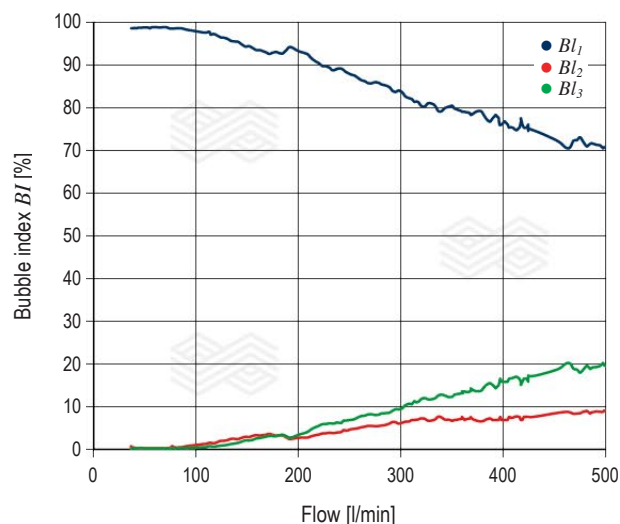
A typical graph of a slot plug showing the variation of the bubble index versus the flow rate is given in Figure 4. The blue line depicts the bubble index  $BI$  for low frequencies, which is typical for large bubbles. The  $BI$  for high frequencies, typical for small bubbles is given in green and the  $BI$  for the medium frequency range representing midsized bubbles is shown in red. Slot plugs generate vibrations predominantly in the low frequency range as shown by the blue line. At low flow rates almost all of the vibrations detected are in the low frequency range.

With rising flow rates, medium and high frequency portions increasingly occur. However, up to 500 l/min over 70% of all vibrations were detected in the low frequency range.

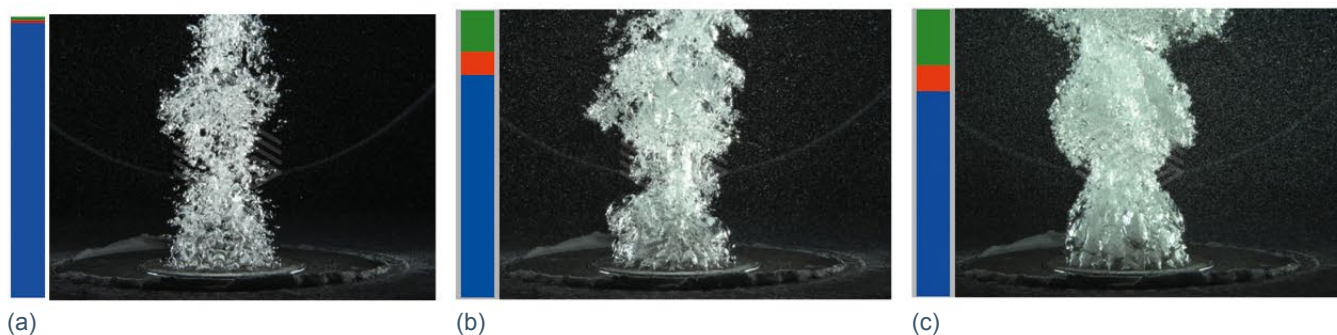
Investigations carried out in parallel with a high-speed camera at flow rates of 30 l/min, 250 l/min, and 500 l/min show that the bubble size and shape at the plug surface stays more or less the same over the whole flow range and that there is hardly any influence of the flow rate on the bubble size (Figure 5). The coloured bars left to the pictures illustrate the respective portion of low (blue), medium (red), and high frequencies (green) in the vibration spectrum at the given flow rate.

**Figure 4.**

Development of the bubble index  $BI$  versus the gas flow rate for a slot plug.

**Figure 5.**

Bubble sizes and shapes of a slot plug at (a) 30 l/min, (b) 250 l/min, and (c) 500 l/min.



### Large porous plugs

A typical graph of a large porous plug showing the variation of the bubble index **BI** versus the flow rate is given in Figure 6. Large porous plugs show a very different bubble index pattern compared to slot plugs. The predominant vibration frequency range is governed by the applied flow rate and varies dramatically over the full flow range. At flow rates up to 200 l/min, about 70–80% of all vibrations were detected in the high frequency range as shown by the green line. Above 200 l/min, the high frequency portion starts to diminish and decreases to almost zero at 500 l/min. The opposite behaviour can be observed for the low frequency portion. At flow rates up to 200 l/min, at maximum 15% of all vibrations are in the low frequency range. Above 200 l/min, the low frequency portion starts to grow and achieves its maximum at about 350 l/min with a share of 60%. Above 350 l/min, the low frequency portion starts to diminish until a share of 45% is reached at 470 l/min; then, a small increase to 50% can be observed again at 500 l/min. The medium frequency range in the vibration pattern stays insignificant with a maximum share of 15% up to a flow rate of 350 l/min. Above 350 l/min, the medium frequency portion starts to increase with rising flow rates and achieves a maximum of about 50% at 470 l/min, staying constant up to 500 l/min.

**Figure 6.**

Development of the bubble index **BI** versus the gas flow rate for a large porous plug.

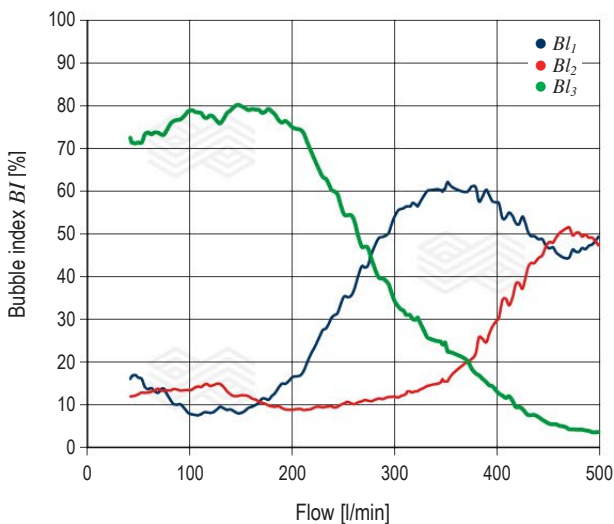


**Figure 7.**

Bubble sizes and shapes of a large porous plug at (a) 50 l/min, (b) 250 l/min, and (c) 500 l/min.



Photos taken with a high-speed camera showing the bubble formation at the plug surface of a large porous plug at 50 l/min, 250 l/min, and 500 l/min are given in Figure 7. A visual, qualitative comparison confirms a shift to larger bubble sizes with increasing flow rates. This is in good agreement with the vibration measurements of the bubble index, given to the left of each picture.

### Small porous plug

A typical graph of a small porous plug showing the variation of the bubble index **BI** versus the flow rate is given in Figure 8. Again, the blue line depicts the **BI** for low frequencies, which are typical for larger bubbles, the green line represents the **BI** for high frequencies, which are typical for smaller bubbles, and the **BI** for the medium frequency range representing midsized bubbles is given in red. Small porous plugs generate a bubble index pattern very similar to large porous plugs. However, characteristic shifts of the vibration pattern in regard to the flow rates can be observed. Photos taken by a high-speed camera show a very similar evolution of bubble size and shape as the large porous plug demonstrated in Figure 9.

**Figure 8.**

Development of the bubble index **BI** versus the gas flow rate for a small porous plug.

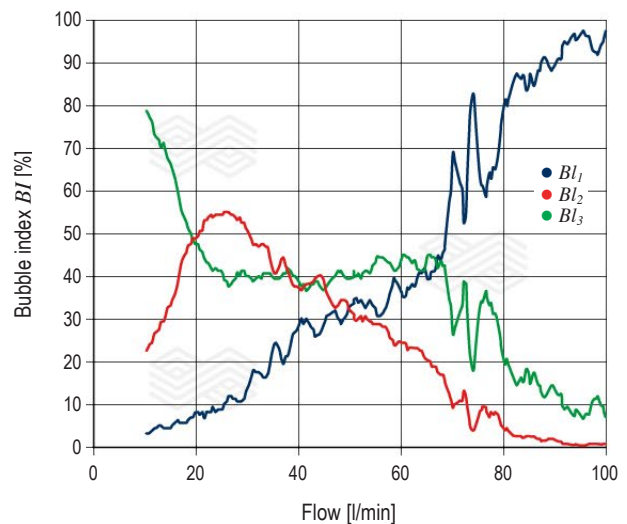


**Figure 9.**

Bubble sizes and shapes of a small porous plug at (a) 2 l/min, (b) 25 l/min, and (c) 70 l/min.



### Summary

The investigations showed that vibrations which are generated by gas purging at the plug-to-water interface and detected at the connecting pipe of the purging plug correlate very well to the gas bubble development at the plug to water interface. Correlating frequency data with high-speed camera photos enable the following conclusions for the investigated plugs in the applied flow range. Slot plugs show only a small dependency of the bubble size on the applied flow rate. They generate mostly large bubbles and only minor amounts of smaller and medium-sized bubbles. Especially at low flow rates, hardly any small bubbles are present. With increasing flow rates, minor amounts of medium and large-sized bubbles start to form. The overall purging characteristics remain almost constant over the entire flow range. Contrary to this behaviour, porous plugs show a strong dependency of the bubble size on the applied flow rate. At low flow rates, almost all bubbles are small and up to a certain limit increasing flow rates generate more but not larger bubbles. Above this limit, at medium flow rates, the number of small bubbles starts to diminish and the share of large bubbles grows. At high flow rates, almost all bubbles are large or medium-sized bubbles. No small bubbles are left. Investigations on the influence of porous plug size on the bubble regime have revealed a clear influence.

Porous plugs with large plug-to-water interfaces remain in the small-bubble regime longer than porous plugs with small plug-to-water interfaces.

### Conclusion

Vibration investigations on purging plugs in a water model enable a quantitative description and differentiation/evaluation of plug types and purging characteristics. Considerable differences between slot plugs and porous plugs were found. Slot plugs mainly generate a small number of large bubbles, which makes them not the best choice for soft purging whereas porous plugs generate a high number of small bubbles, which makes them ideal for soft purging. By increasing the size of the porous plug, the number of small bubbles can be further increased. These findings show a very good agreement with prior work [2].

The next step is an extension of these vibration investigations to steel ladles to find out if this vibration method can also be used under real steel mill conditions. Another promising application of this vibration method is the product development of more effective purging plugs as new plug designs and their characteristics can be evaluated and compared to standard plug designs.

### References

- [1] Stolte, G. Secondary Metallurgy, Fundamentals, Processes, Applications. *Stahleisen Communications*. 2002.
- [2] Trummer, B., Fellner, W., Viertauer, A., Kneis, L. and Hackl, G. A Water Modelling Comparison of Hybrid Plug, Slot Plug and Porous Plug Designs. *RHI Bulletin*. 2016, No. 1, 35–38.
- [3] Nadif, M., Orue, L., Lachmund, H., Abdullah, H. and Rössler, R. Online Control of Desulphurisation and Degassing Through Ladle Bubbling Under Vacuum (ONDECO) Research Fund for Coal and Steel, European Commission, 2012.
- [4] Yenus, J., Brooks, G. and Dunn, M. Principal Component Analysis of Vibration Signal in Ladle Metallurgy. Presented at the AISTech, Pittsburgh, USA, May 2016, 1245–1253.
- [5] Fischer, A., Krüger, K. and Weinberg, M. Bewertung der Behandlung von Stahlschmelzen mithilfe von Schallsensoren, *Stahl und Eisen*. 2017, 137, 1245–1253.
- [6] POSCO Corporation, Method for Predicting Residual Length of Porous Plug in Ladle. Korean Patent KR2003054638B, 2003.
- [7] [http://www.nuprocorp.com/pdf\\_file/TruStir\\_Brochure\\_0505.pdf](http://www.nuprocorp.com/pdf_file/TruStir_Brochure_0505.pdf); accessed 11.09.2019.
- [8] Hammerer, W., Raidl, G. and Barthel, H. Gasspülsteine für Stahlpfannen. *Radex-Rundschau*. 1992, 4, 217–226.
- [9] Manhart, C. Gas Purging Plug, Gas Purging System. Pending Patent WO2019/145522A1, 2018
- [10] Wong, M.W. Discrete Fourier Analysis, Springer, Basel, 2011.

### Authors

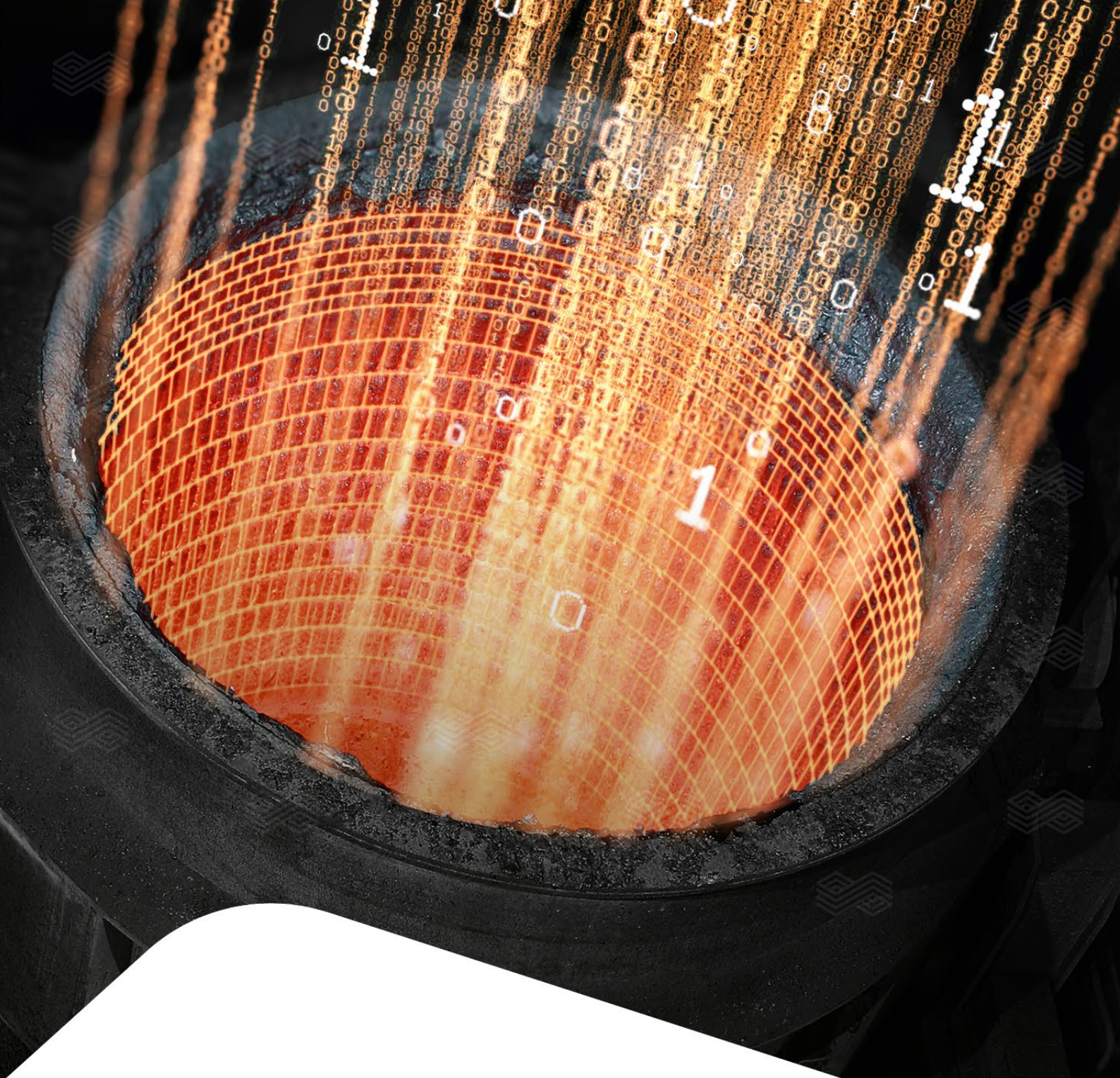
Bernd Trummer, RHI Magnesita, Vienna, Austria.

Christian Manhart, RHI Magnesita, Technology Center, Leoben, Austria.

Wolfgang Fellner, RHI Magnesita, Technology Center, Leoben, Austria.

**Corresponding author:** Bernd Trummer, bernd.trummer@rhimagnesita.com





## Lifetime prediction with the power of AI Automated Process Optimization (APO)

APO, our unique and patented automated process optimization, uses artificial intelligence to calculate a digital twin of your refractories in order to make refractory lifetime predictable. Meaning: Increased safety, optimized production, and fewer production losses.

Curious to experience APO in more detail?  
Then contact us to receive a free online live presentation carried out by our experts!  
Visit [rhimagresita.com/apo-wear-lifetime-prediction-with-the-power-of-ai/](https://rhimagresita.com/apo-wear-lifetime-prediction-with-the-power-of-ai/)

Follow us



RHI MAGNESITA

Guenter Unterreiter, Daniel R. Kreuzer, Bernd Lorenzoni, Hans U. Marschall, Robert Machhammer and Gernot Hackl

# Compressive Creep Measurements of Fired Magnesia Bricks at Elevated Temperatures Including Creep Law Parameter Identification and Evaluation by Finite Element Analysis

Creep behavior is very important for the selection of refractory materials. This paper presents a methodology to measure the compressive creep behavior of fired magnesia materials at elevated temperatures. The measurements were carried out at 1150–1500 °C and under compression loads from 1–8 MPa. Creep strain was calculated from the measured total strain data. The obtained creep deformations of the experimental investigations were subjected to detailed analysis to identify the Norton-Bailey creep law parameters. The modulus of elasticity was determined in advance to simplify the inverse estimation process for finding the Norton-Bailey creep parameters. In the next step, an extended material model including creep was used in a finite element analysis (FEA) and the creep testing procedure was reproduced numerically. Within the investigated temperature and load range, the creep deformations calculated by FEA demonstrated a good agreement with the results of the experimental investigations. The consideration of the creep behaviour in the design process will lead to an improved prediction of strains and stresses.

## Introduction

Material selection is a critical stage during engineering of structural components in complex furnaces and refractory linings (Figure 1). Optimized operating conditions, greater output, and efficiencies push refractories to their physical limits. Therefore, high-performance refractory products combined with sophisticated material models are needed to predict the in-service performance. Although much information is available on the effect of additives, corrosion process, and thermomechanical behaviour of refractories [2] [3], significantly less data exists on the creep response of refractories at high temperatures.

In material science, creep is defined as the time-dependent deformation of a material due to the combined influence of temperature plus an applied load [4]. If a specimen is loaded with a force at high temperature, a time-dependent strain is observed as illustrated in Figure 2. After a spontaneous elastic strain ( $\epsilon_0$ ), three creep stages occur: The so-called primary (I), secondary (II), and tertiary creep range (III) (see Figure 2) [5].

However, it has to be mentioned that most refractory structures are not subjected to pure creep under constant load. In most cases, the global loads, not considering local stresses for example due to thermal shock, are caused by restrictions of the refractories' thermal expansions due to rigid external structures (e.g., steel shell). In this case, the creep of the material will result in a decrease in load. Once the suppressed thermal expansion is compensated by the creep, there will be no significant load on the material and the creep process will be stopped before reaching the

Figure 1.

Refractory lining of an electric arc furnace for the nonferrous and ferroalloys industry.

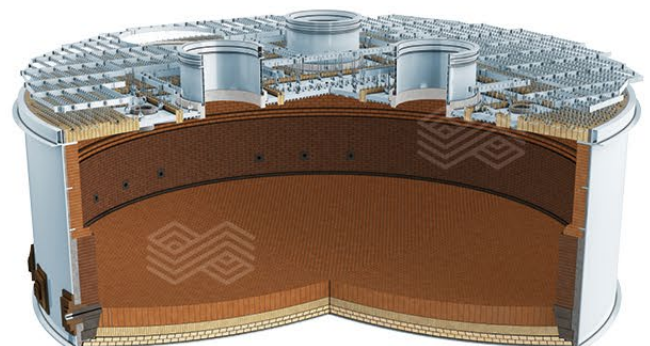
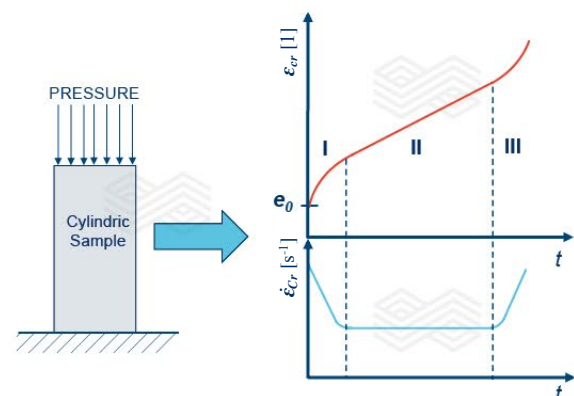


Figure 2.

Typical shape of a three-region creep curve showing creep strain ( $\epsilon_{cr}$ ) and strain rate ( $\dot{\epsilon}_{cr}$ ).



tertiary creep stage, which would cause the collapse of the structure. In some unique cases, for example in a regenerator superstructure, the weight load of the checker bricks in combination with elevated temperatures could cause stresses relevant for creep that will not disappear with increasing deformation. Hence, special care has to be taken when selecting materials for such structures in order to avoid creep-induced failure.

### Methodology for Creep Data Identification

The creep testing device for high-temperature compressive creep application and an efficient methodology to identify the creep law parameters used in this study were developed by the Chair of Ceramics (University of Leoben) in a preliminary scientific work [1].

In order to understand and predict the material behaviour and the behaviour of refractory superstructures in operating furnaces, accurate engineering creep data is needed. The chemical composition of the commercially available brick used in the research is given in Table I.

**Table I.**

Average chemical composition of the magnesia brick under investigation in wt. %.

MgO	Al <sub>2</sub> O <sub>3</sub>	Fe <sub>2</sub> O <sub>3</sub>	CaO	SiO <sub>2</sub>
97.0	0.1	0.2	1.9	0.6

Refractory creep can be adequately described by the Norton-Bailey creep law (Equation 1) [1]. According to the Norton-Bailey strain hardening/softening formulation, the creep strain rate  $\dot{\epsilon}_{cr}$  is a function of temperature ( $T$ ), stress ( $\sigma$ ), and creep strain ( $\epsilon_{cr}$ ):

$$\dot{\epsilon}_{cr} = K(T) \cdot \sigma^n \cdot \epsilon_{cr}^a \quad (1)$$

Exponent  $a$  is negative in the case of strain hardening (primary creep) and positive for strain softening (tertiary creep). Secondary creep occurs if exponent  $a$  is equal to zero. Parameter  $K$  is a temperature function and  $n$  the stress exponent [1]. The tertiary creep contribution is of minor importance for the design, since tertiary creep is followed by failure of the component and should not be reached anyway [5]. In this research, the contribution of tertiary creep was neglected; creep strain is described by primary and secondary creep strain.

The measurement results in this work include the elastic and viscoplastic creep deformation. Hence, the creep strain must be derived from the uniaxial mechanical strain  $\epsilon_{mech}$ , the applied stress  $\sigma$ , and the Young's modulus  $E$  (equation 2).

$$\epsilon_{cr} = \epsilon_{mech} - \frac{\sigma}{E} \quad (2)$$

The total strain  $\epsilon_{tot}$  is composed of the thermal strain  $\epsilon_{th}$ , the elastic strain  $\epsilon_{el}$ , and the creep strain  $\epsilon_{cr}$ . In the case of compression, the mechanical strain and stress are negative.

Hence under compression the absolute value of the creep strain  $\epsilon_{cr}$  reduces the absolute value of the total strain (equation 3).

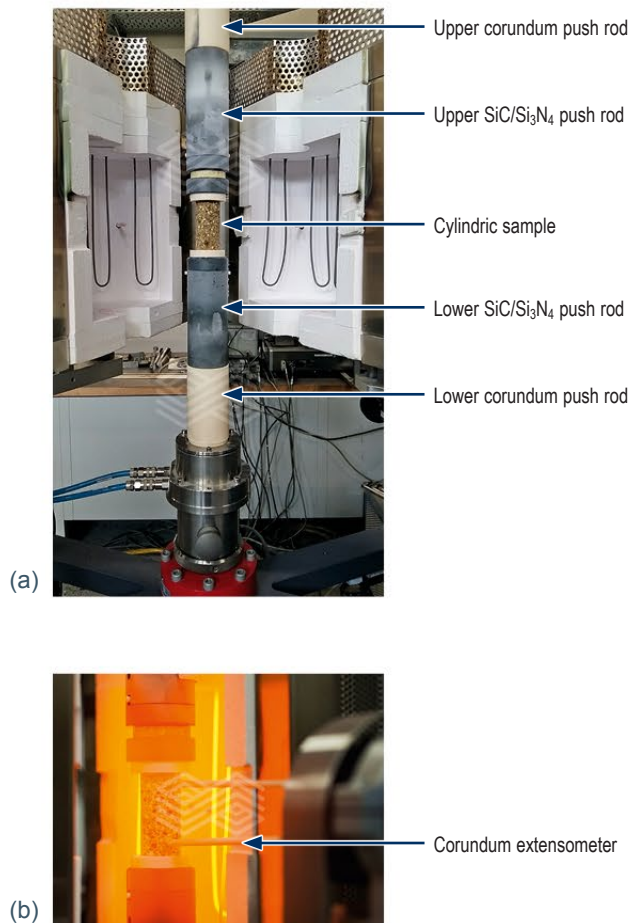
$$\epsilon_{tot} = \epsilon_{th} + \epsilon_{el} + \epsilon_{cr} \quad (3)$$

The exact procedure to identify the parameters  $K$ ,  $n$ , and  $a$  for the Norton-Bailey creep law are described in [1]. The main part of the high-temperature compressive creep testing device, developed by the Chair of Ceramics (University of Leoben), is an electric furnace which is equipped with molybdenum disilicide heating elements, push rods, and corundum extensometers. An inside view of the furnace is shown in Figure 3.

Two platinum-rhodium thermocouples were used to measure the temperatures. The first one was near the specimen to monitor its temperature and the second one was close to the heating elements to control the furnace temperature. The load was applied by a spindle and measured by a load cell. The deformation was measured by two pairs of corundum extensometers with an initial leg distance of 50 mm; these pairs were placed in front and at the back side of the sample. The total strain data measured by each of these two extensometer pairs were recorded and the average values were used for further calculations.

**Figure 3.**

Internal views of the high-temperature compressive creep testing device. (a) Cold state and (b) during heating.



For the creep tests, cylindrical samples with a diameter of 35 mm and a height of 70 mm were used (Figure 4); a preload of 100 N was applied axially to fix the sample. The height/diameter ratio of 2 is suitable for deformation measurements in a zone of the specimen which is not affected by friction of the cylinder's front surfaces [1]. The furnace was heated up to a defined temperature at 10 K/min, followed by a dwell time of 30 minutes to reach isothermal conditions in the cylinder. Afterwards, the two extensometer pairs were attached to the specimen's surfaces; then a defined load was applied by lifting the lower crosshead. During measuring, this load was kept constant for the entire testing period of 5 hours. The measurements were carried out at 1350 °C, 1425 °C, and 1500 °C. The recording of the extensometer data started from the beginning of the loading procedure. As mentioned previously, the measurement results include the elastic and creep information. After the experimental test and its evaluation, a FEA was conducted to verify and validate the advanced creep material model. For this purpose, a 2D axisymmetric model was used. The height of the cylinder in the model was 50 mm, representing the initial leg distance of the extensometer tips. For meshing the cylinder, 3560 linear quadrilateral elements of type RAX2 were used. The force data measured by the load cell in the creep testing device were used as boundary conditions for modelling the compression.

## Results

The two extensometer pairs recorded the deformation caused by compression. Based on these data, a total strain/time curve under constant load and temperature was obtained. It is worth mentioning that the Young's modulus and the Poisson ratio were kept constant over the whole temperature range of 1350–1500 °C in order to simplify the complex inverse parameter estimation. In a further research study, a parameter calibration could be used to determine the Young's modulus based on the creep data and

parameters found in this study. The creep of the investigated material was still in the primary stage since the values of  $a$  were negative (Table II) for all tested temperatures and loads.

For defined temperatures different compression loads were used; these led to characteristic total strain/time curves (Figure 5).

The creep curves were utilized for the determination of the creep parameters. Therefore, a damped least square method (Levenberg-Marquardt) (for further details see [1]) was carried out to inversely estimate the corresponding Norton-Bailey creep law parameters  $K$ ,  $n$ , and  $a$ , which are listed in Table II.

**Table II.**

Norton-Bailey creep law parameters of a fired magnesia brick at different temperatures.

T [°C]	$K$ [MPa <sup>n</sup> s <sup>-1</sup> ]	$n$	$a$
1350	$9.11 \times 10^{-14}$	4.60	-1.07
1425	$5.52 \times 10^{-11}$	1.55	-1.24
1500	$8.98 \times 10^{-10}$	1.39	-0.75

A comparison of the calculated deformation based on either Norton-Bailey or a linear elastic approach was performed; Figure 6 shows the total strain data (1350 °C, 8 MPa). In both configurations of the simulation the same load of 8 MPa was applied; using the Norton-Bailey material law a vertical displacement of 420 µm was measured which led to a total strain of  $8.28 \times 10^{-3}$ . Based on the linear elastic approach, the same load caused a vertical displacement of 8 µm resulting in a total strain of  $0.16 \times 10^{-3}$ . On the other hand, using a linear elastic material model, a displacement due to thermal expansion of 8 µm caused a compressive stress of 8 MPa.

**Figure 4.**

(a) Cylindric specimen for compressive creep test and (b) schematic overview of the 2D axisymmetric FEM model for the virtual creep test procedure.

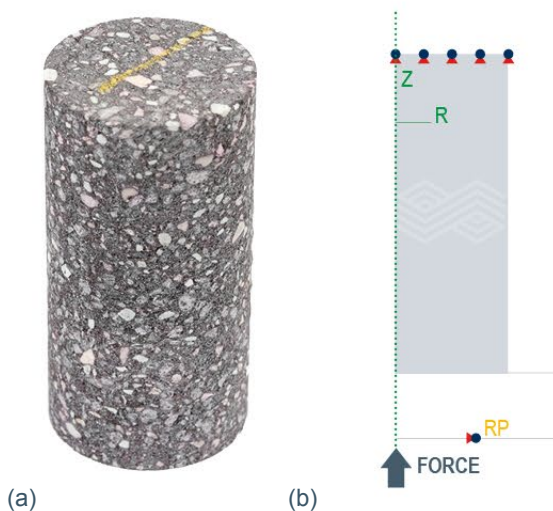
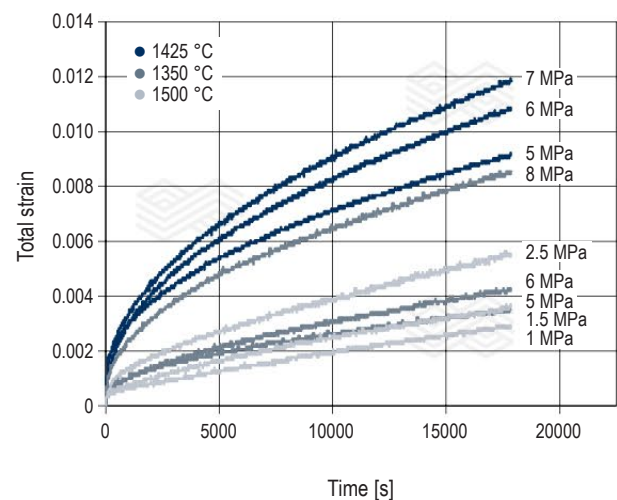


**Figure 5.**

Comparison of total strain/time curves of a fired magnesia brick from experiments at 1350 °C, 1425 °C, and 1500 °C and with varying compressive loads between 1–8 MPa.



Total strain curves for a defined temperature versus testing time derived experimentally and through FEA simulation are shown in Figure 6, Figure 8, and Figure 9. As depicted in Figure 6, the material showed distinctive creep behaviour at 1350 °C. The creep parameters which were found for 1350 °C cover the whole load range of 5, 6, and 8 MPa, resulting in a good agreement of the experimental and the simulated 8 MPa curve.

The curves generated for 5 and 6 MPa have a similar progression in the first 2000 s. As shown in Figure 7, even the 5 MPa curve shows a higher total strain than the 6 MPa curve. This can be explained by material inhomogeneities and the creep behaviour of the material at the relatively low temperature in combination with the precision of the testing device. Hence, this caused uncertainties for the inverse estimation procedure of the creep parameters resulting in aberrations between simulated and experimental curves seen in Figure 8.

The measured total strain curves for 1425 °C and 1500 °C (Figure 9 and Figure 10) show a satisfactory agreement over the whole load range with the simulated curves.

**Figure 6.** Comparison of total strain/time curves of a fired magnesia brick obtained from experiment and numerical simulation using Norton-Bailey creep law or a linear elastic approach at 1350 °C and 8 MPa compressive load.

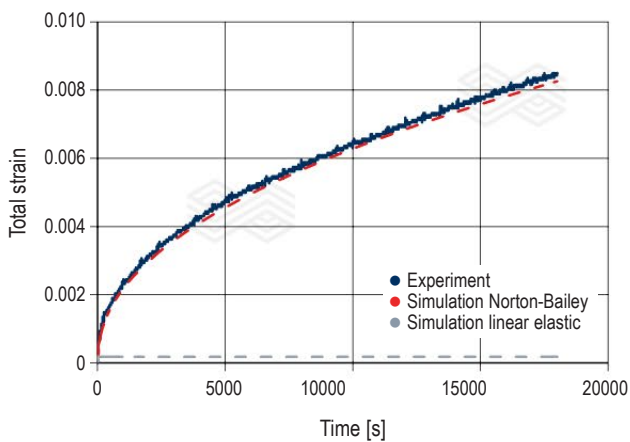


**Figure 7.** Comparison of total strain/time of a fired magnesia brick from experiments at 1350 °C.

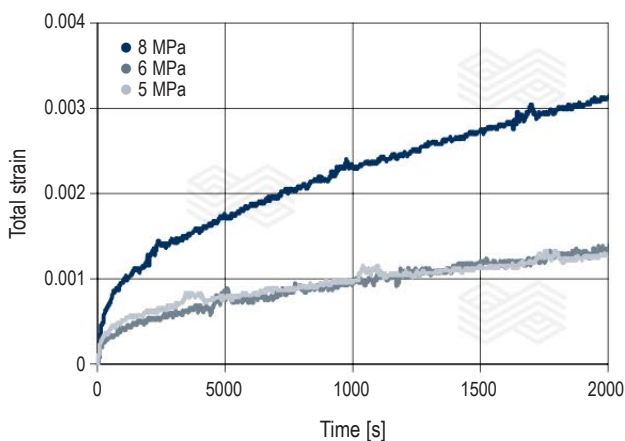


**Figure 8.** Comparison of total strain/time curves of a fired magnesia brick from experiment and numerical simulation using Norton-Bailey creep law at 1350 °C and 5, 6, 8 MPa compressive load.

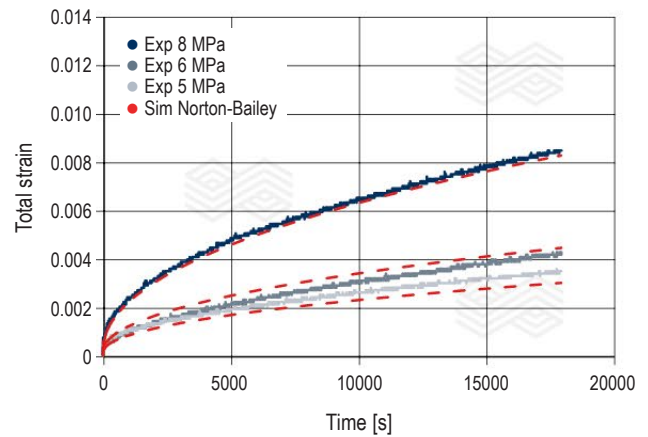


**Figure 9.** Comparison of total strain/time curves of a fired magnesia brick from experiment and numerical simulation using Norton-Bailey creep law at 1425 °C and 5, 6, 7 MPa compressive load.

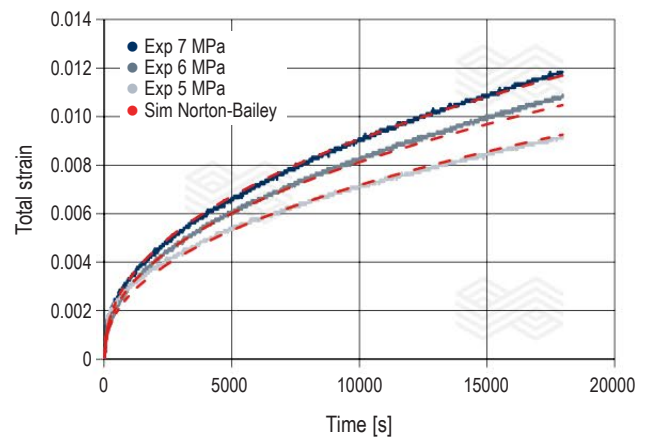
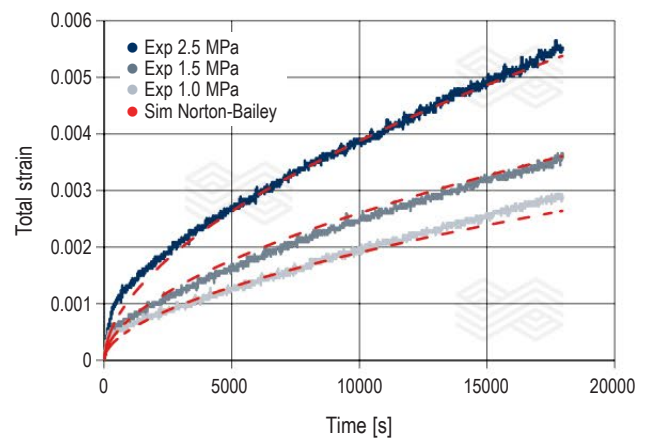


**Figure 10.** Comparison of total strain/time curves of a fired magnesia brick from experiment and numerical simulation using Norton-Bailey creep law at 1500 °C and 1.0, 1.5, 2.5 MPa compressive load.



---

## Conclusions

The advanced high-temperature compressive creep testing device can be used to characterize the creep behaviour of refractory materials at elevated loads and temperatures. The obtained creep deformations of the experimental investigations were subjected to detailed analysis and mathematical treatment. An iterative inverse method was used to determine the three parameters for the Norton-Bailey creep law from the strain data. The experimental and simulated total strain curves for a defined temperature were compared and showed very good agreement. In a further research study, a parameter calibration could be used to determine the Young's modulus based on the creep data and parameters found in this study. Within the investigated temperature and load range, the creep deformations calculated by FEA have demonstrated a good agreement with the results of the experimental investigations. The implementation of the creep model will lead to a significant improvement during the design process and refractory engineering. Furthermore, it will improve the prediction of thermomechanical stresses and strains as well as predicting the in-service behaviour of refractory linings.

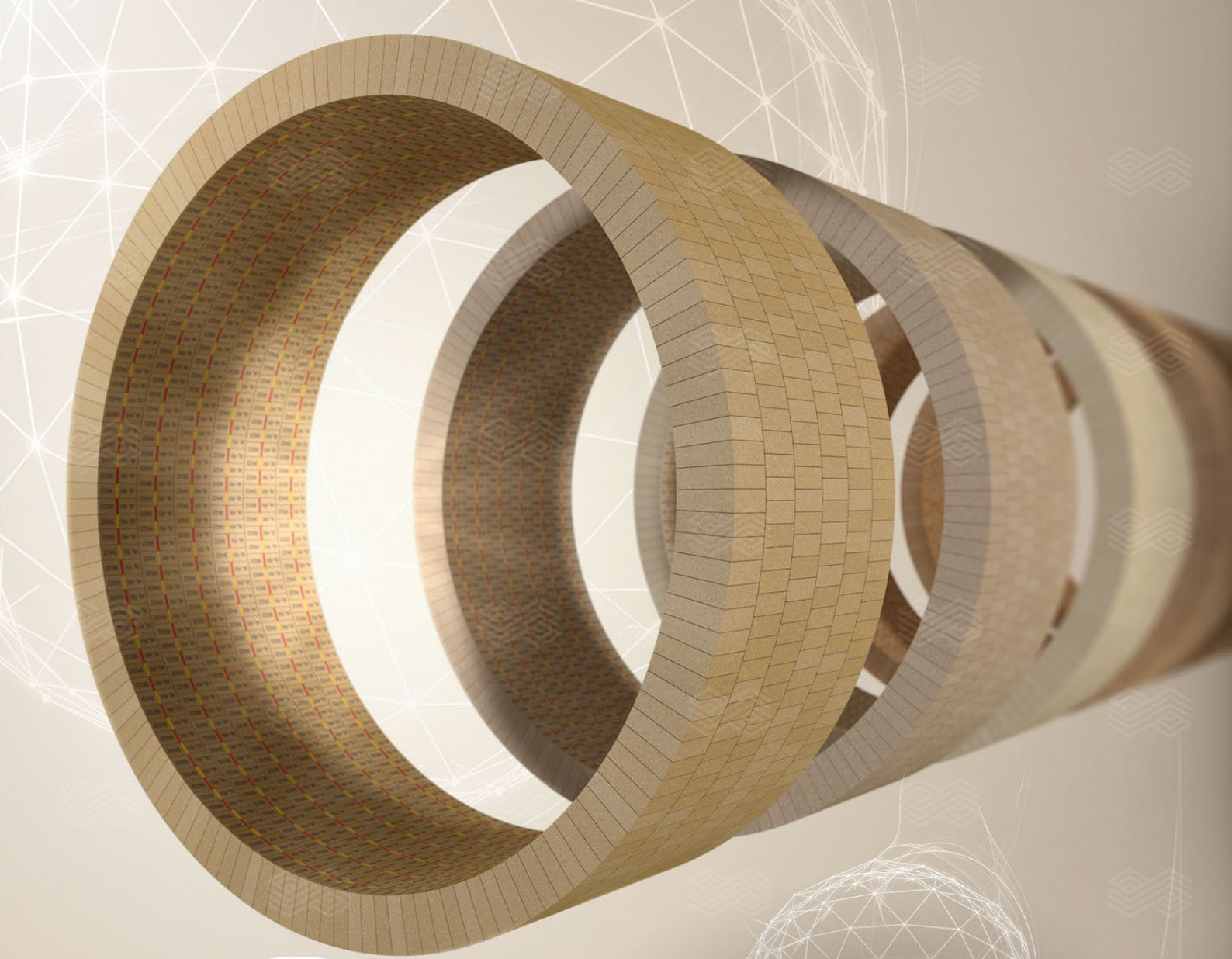
## References

- [1] Jin, S., Harmuth, H. and Gruber, D. Compressive creep testing of refractories at elevated loads – Device, material law and evaluation technique. *Journal of the European Ceramic Society*. 2014, 34, 4037–4042.
- [2] Afshar, S. and Allaire C. The corrosion of refractories by molten aluminium. *JOM*. 1996, 48, 5, 23–27.
- [3] Allahevrdi, M., Afshar, S. and Allaire, C. Additives and the corrosion resistance of aluminosilicate refractories in molten Al-5Mg. *JOM*, 1998, 50, 2, 30–34.
- [4] Richerson, D.W. *Modern Ceramic Engineering: Properties, Processing and Use in Design*. Marcel Dekker, Inc., New York, 1992, 834.
- [5] Munz, D. and Fett, T. *Ceramics Mechanical Properties, Failure Behaviour, Material Selection*. Berlin, Heidelberg New York, Springer, 2001, 227–229.

## Authors

Guenter Unterreiter, RHI Magnesita, Technology Center, Leoben, Austria.  
Daniel Rene Kreuzer, RHI Magnesita, Technology and Support, Vienna, Austria.  
Bernd Lorenzoni, RHI Magnesita, Technology Center, Leoben, Austria.  
Hans U. Marschall, RHI Magnesita, Technology Center, Leoben, Austria.  
Gernot Hackl, RHI Magnesita, Technology Center, Leoben, Austria.  
Robert Machhammer, RHI Magnesita, Technology Center, Leoben, Austria.  
**Corresponding author:** Guenter Unterreiter, guenter.unterreiter@rhimagnesita.com





**ANKRAL X-SERIES**

spinosphere technology by RHI Magnesita

## Pushing refractory performance into new spheres

With the new spinosphere technology you don't have to compromise any longer. Benefit from previously unobtainable brick properties. The novel spinel reduces the alumina content by up to 70%, maximizing flexibility without impairing hot properties and clinker melt resistance.

ANKRAL X-Series — improved performance for challenging conditions.

Curious to find out more details?  
Visit [rhimagresita.com/spinosphere](https://rhimagresita.com/spinosphere)

Follow us



RHI MAGNESITA

Daniela Fonseca, Graziella Pacheco, Wagner Moulin Silva, Geraldo Gonçalves and Rainer Neuböck

# Development and Applicability of a New Corrosion Test to Quantify Refractory Wear Due to Gaseous Sulphur Oxides Action

Degradation by sulphur gases is an important lining wear mechanism in the copper industry.  $\text{SO}_2/\text{SO}_3$  gases infiltrate into the pores of the basic refractory bricks, combine with their raw materials and significantly modify the bricks' structure. This study presents a comparison of the corrosion resistance of different refractories against sulphur attack using a simple, low-cost, and quantitative method. The novel test method provides results that agree with what is commonly observed during operation and in previous postmortem studies. This tool is very appropriate for the selection of refractory grades for the copper industry and prediction of their performance.

## Introduction

Oxidation of matte sulphides during copper production leads to the formation of sulphur oxides, which infiltrate into the pores of the refractory lining and react with the basic oxides below 1000 °C to form sulphates. This reaction is accompanied by an expressive theoretical volume increase, consequent densification of the refractory microstructure, and weakening of the brick bond [1]. Thus, corrosion by  $\text{SO}_2/\text{SO}_3$  gases is an important wear mechanism in the nonferrous industry and should be considered when defining refractories for this application. Previous studies on the corrosion resistance of MgO-containing materials against sulphur oxides include expensive and complex testing methods. [2–5]. The current study is based on a novel test method to assess alkali infiltration [6] and aims to provide an evaluation of the corrosion resistance of refractories by  $\text{SO}_2/\text{SO}_3$  gases in a simple and quantitative manner. A case study is provided to illustrate the damage caused by sulphur oxides in refractory linings.

## Case Study

After a campaign of 1.5 years, high wear was identified in the upper shaft of a copper ISASMELT furnace. The brick used was a direct bonded magnesia-chromite brick type MCr 50 (ISO 10081-2) shown in Figure 1. The hot face was significantly altered by slag. The macroscopically unaltered cold face was analysed by sulphur elemental analysis (DIN 51085:2015-01) and scanning electron microscopy with coupled energy dispersive spectroscopy (SEM-EDX). The sulphur content in the cold face was only 0.6%, but the microstructure showed severe alteration, with the formation of calcium sulphate (Figure 2). Many magnesia grains were rimmed with remains of magnesium sulphate decomposition.

The brick studied in this case was insulated during use and this may be the cause of the observed decomposition of the magnesium sulphate and consequent low amounts of sulphur detected in the cold face. Apparently, magnesium and calcium sulphates are formed during operation, but the high temperatures in the upper zone, where post-oxidation of CO and sulphur-containing gases occurs, is enough to promote the decomposition of the magnesium sulphate phases. Calcium sulphate, on the other hand, only decomposes or melts at temperatures above 1400 °C [7]. Sulphur attack and consequent modification of the brick's structure was considered the main wear mechanism in this study.

## Experimental Procedure

Seven commercial refractory bricks were chosen for comparison and their description is provided in Table I. An alumina-silica-based refractory was used to manufacture a box (270 x 200 x 70 mm) in which the test would take place. The box could only fit eight specimens; therefore, this evaluation was split into two different tests to assess all seven compositions in duplicate. The brick A5 was used as a reference in both tests to evaluate the reproducibility of this method.

**Figure 1.**

**Brick taken from an ISASMELT furnace, showing matte infiltration and spalling in the hot face.**



**Table I.**

Refractory grades used in the study.

Used in test #	Sample abbreviation	Description
1	MKD	Direct bonded magnesia-chromite grade based on dead burned magnesia and chromite (MCr60, ISO 10081-2)
1	MKF	Magnesia-chromite grade based on fused magnesia-chromite grains (MCr60, ISO 10081-2)
1	A10	Chromium corundum grade based on fused alumina and about 10% Cr <sub>2</sub> O <sub>3</sub>
1 & 2	A5	Chromium corundum grade based on fused alumina and about 5% Cr <sub>2</sub> O <sub>3</sub>
2	PM	Pure magnesia grade based on dead burned magnesia
2	MSI	Semi-rebonded magnesia-chromite grade based on fused MgO and chromite with magnesium sulphate solution impregnation (MCr60, ISO 10081-2)
2	MSN	Semi-rebonded magnesia-chromite grade based on fused MgO and chromite, no impregnation (MCr60, ISO 10081-2)

Both tests were performed according to the procedure described below and Figure 3 illustrates the specimen configuration after firing.

- The box's interior was covered with about 260 g of fine aluminium sulphate (supplied by Bauminas Química).
- Four cubes (30 mm x 30 mm x 30 mm) were cut from each brick.
- Two cubes were sent for bulk density (BD) and apparent porosity (AP) measurement according to the ABNT NBR 6220 standard using petrol kerosene.
- The other two cubes of each grade were placed inside the box, on top of an alumina-based refractory plate.
- The box was closed using a high-alumina mortar to fix the lid and fired at 900 °C for 12 hours (heating rate: 100 °C/h).
- After the test, the cubes were sent for BD and AP testing using petrol kerosene (ABNT NBR 6220 standard). The same cubes were dried at 120 °C for 6 hours and afterwards sent for the following tests: Loss on ignition, X-ray fluorescence (XRF), X-ray diffraction (XRD), and humidity.
- In addition, the aluminium sulphate was analyzed before and after the test to determine the extent of its decomposition.

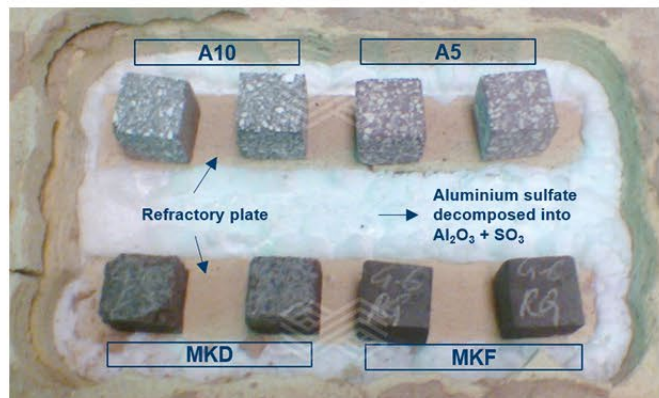
The resistance against corrosion by sulphur oxides was measured considering the infiltrated sulphur amount and the change in the bulk density (BD) and apparent porosity (AP) calculated in (1) and (2).

$$\text{Change in BD [\%]} = \frac{BD_{\text{after}} - BD_{\text{before}}}{BD_{\text{before}}} \times 100 \quad (1)$$

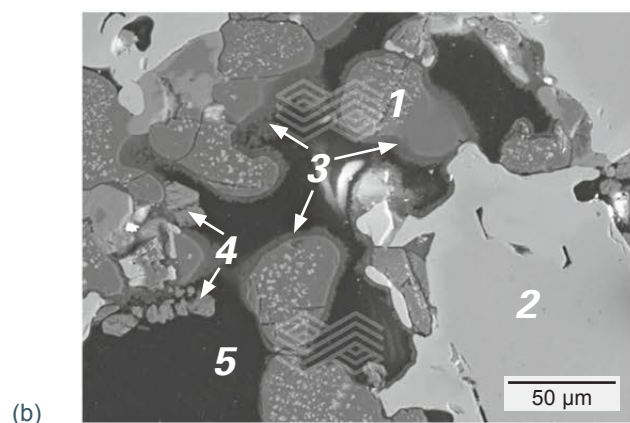
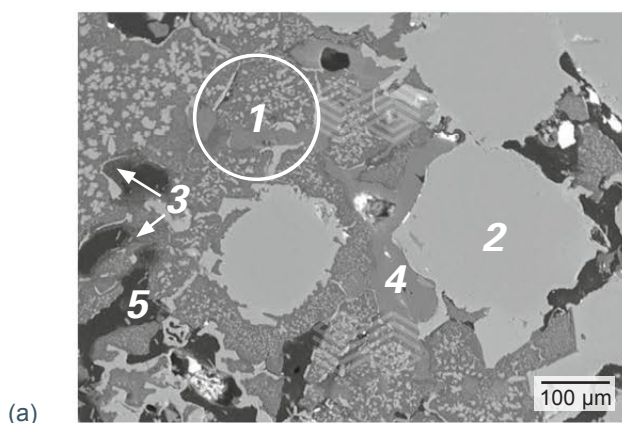
$$\text{Change in AP [\%]} = \frac{AP_{\text{after}} - AP_{\text{before}}}{AP_{\text{before}}} \times 100 \quad (2)$$

**Figure 3.**

Specimen configuration from the first test after firing.

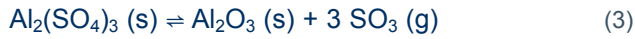
**Figure 2.**

(a) SEM-EDX analysis of hot face (Area "1" in Figure 1) and (b) SEM-EDX analysis of cold face (Area "2" in Figure 1). (1) corroded magnesia, (2) chromite, (3) magnesia rings formed by the decomposition of magnesium sulphate, (4) calcium sulphate, and (5) pore.



## Results and Discussion

Aluminium sulphate was chosen in this study due to its decomposition temperature and relative stability. This compound decomposes as described in (3) at about 1100 K (827 °C) and is one of the least stable sulphates [7]. Sulphur trioxide is not stable at temperatures above 700 °C and spontaneously forms sulphur dioxide and oxygen [8].



Magnesium sulphate decomposition occurs spontaneously in the absence of any reducing agent at 1080 °C [8].

Therefore, at the test temperature (900 °C), the formation of this compound is thermodynamically favoured, as opposed to its decomposition (4).



Figures 4 and 5 present the specimens after the tests and the results obtained in each test are shown in Table II. It was generally observed that the bulk density increased (positive values for the calculated change) and the apparent porosity decreased (negative values for the calculated change), which suggests that the pores of the refractory samples were partially occupied by an additional substance after the tests.

**Table II.**

Physical and chemical test results of each brick sample tested.

	First Test				Second Test			
	MKD	MKF	A10	A5	A5	PM	MSI	MSN
<b>Physical test results</b>								
Change in BD [%]	3.5	1.8	0.6	0.4	0.5	1.8	-0.3	2.3
Change in AP [%]	-30.4	-26.2	-3.7	-1.9	-2.5	-58.4	-5.9	-25.4
<b>Chemical test results</b>								
Humidity [%]	0.6	0.3	0.1	0.1	0.0	0.5	0.8	0.3
LOI [%]	0.6	0.4	0.1	0.0	0.0	0.5	0.7	0.3
SiO <sub>2</sub> [%]	1.2	1.1	1.3	6.7	6.9	0.3	0.8	1.4
TiO <sub>2</sub> [%]	0.2	0.1	0.03	1.8	1.8	0.0	0.1	0.1
Al <sub>2</sub> O <sub>3</sub> [%]	6.1	5.4	91.2	88.4	88.0	0.1	4.5	5.8
Cr <sub>2</sub> O <sub>3</sub> [%]	13.9	17.6	4.4	2.2	2.3	0.1	9.5	11.6
Fe <sub>2</sub> O <sub>3</sub> [%]	7.2	8.0	0.06	0.6	0.6	0.5	6.8	8.5
MgO [%]	68.5	65.4	0.0	0.0	0.0	96.0	74.4	69.6
SO <sub>3</sub> [%]	2.3	1.4	0.03	0.02	0.02	2.1	3.1	2.0

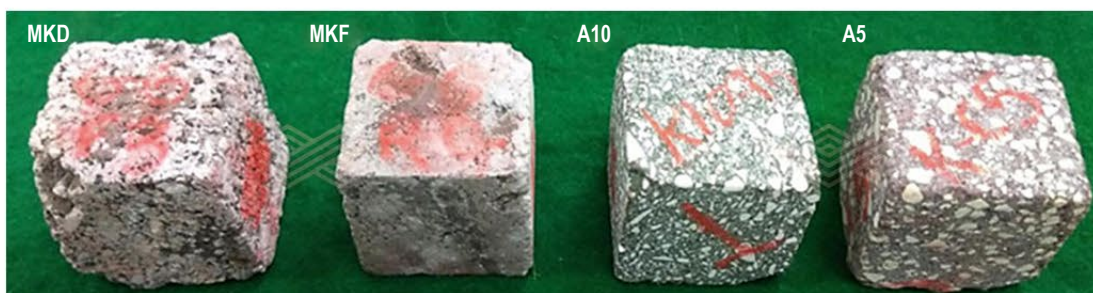
**Figure 4.**

Specimens after the first test.



**Figure 5.**

Specimens after the second test.



Despite the very small sample size used in this study, the considerable change in physical properties before and after the test for some samples was considered relevant due to the low experimental error in BD and AP. However, due to the nonhomogeneous structure of refractory materials, the use of a larger sample size would bring more confidence to these results. Variations of up to 1% in BD and 5% in AP were considered intrinsic to the testing method and were not attributed to the present corrosion test.

After the tests, the chromium corundum specimens (A5 and A10) remained intact, with almost no change in properties, mainly due to the low reactivity of alumina in the presence of sulphur oxides at the test temperature. Composition A5

showed similar results in both tests, which indicates the reproducibility of this method. The bricks containing sintered MgO (MKD and PM) showed the largest change in bulk density and porosity and the highest SO<sub>3</sub> content, which indicates the lowest corrosion resistance due to high raw material reactivity.

The X-ray diffraction profiles in Figures 6 and 7 confirm the presence of MgSO<sub>4</sub> and MgSO<sub>4</sub>·6H<sub>2</sub>O inside the pores in all basic brick specimens according to (4). Magnesium sulphate is highly hygroscopic and is most likely to hydrate at room temperature [8]. The amount of water that it attracts and, consequently, the type of hydrate that will be formed depends on the ambient relative humidity.

**Figure 6.**

Comparison of X-ray diffraction profiles of the samples used in test 1. MS: Magnesium sulphate; SH: Magnesium sulphate hydrate.

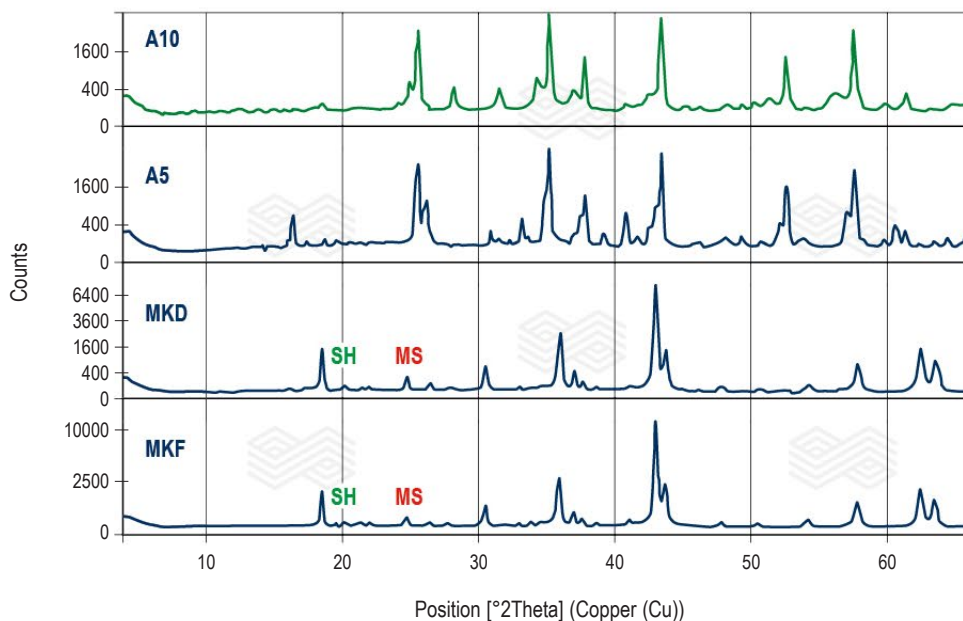
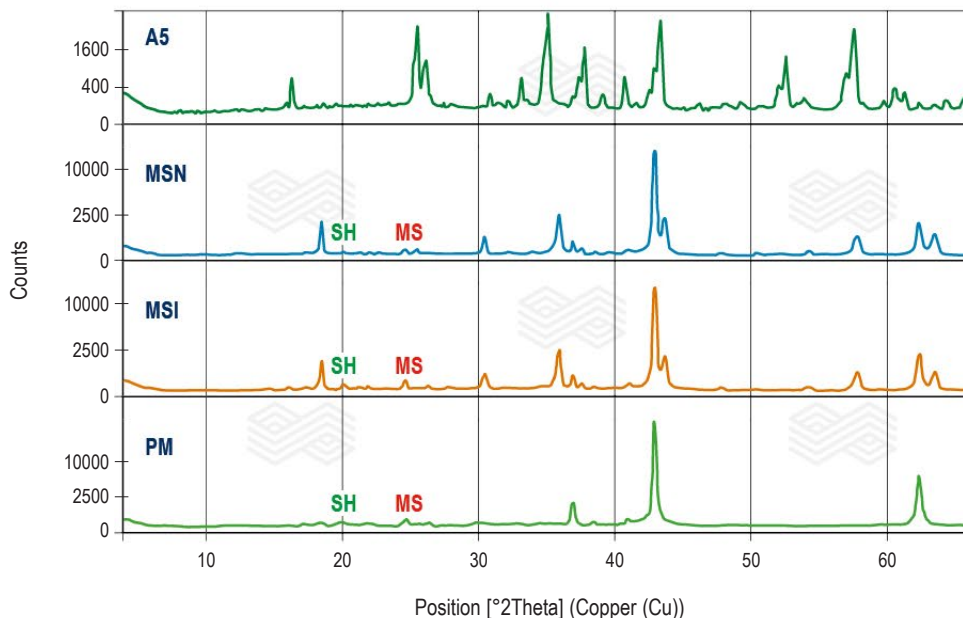


**Figure 7.**

Comparison of X-ray diffraction profiles of the samples used in test 2. MS: Magnesium sulphate; SH: Magnesium sulphate hydrate.



The microstructure of the samples MKD and MKF was evaluated after the test and the microscopic images of polished sections are presented below in Figures 8a and 9a. The typical (nonaltered) microstructure of each brick is presented beside it for comparison in Figures 8b and 9b. The microstructure of MKD after the test (Figure 8a) had large black spots and what seemed like a lack of fines up to 7 mm from the surface. This aspect is similar to the findings in previous postmortem studies involving sulphate corrosion, such as the microstructure image in Figure 2b. The black spots were probably due to the formation of magnesium sulphate hydrate, which does not adhere to the resin used for sample preparation. MKF showed slightly higher resistance to sulphur attack compared to MKD because it was made of fused magnesia grains and had a lower amount of free MgO (Figure 9a). The microstructure was also affected, however only up to 3 mm from the specimen's surface.

In the second test, PM showed by far the highest decrease in apparent porosity, although the  $\text{SO}_3$  content was similar to the magnesia-chromite specimens. The composition MS was tested with (MSI) and without (MSN) previous impregnation with magnesium sulphate solution to evaluate the effect of this production step on its corrosion resistance. The amount of  $\text{SO}_3$  in MSI (Table II) cannot be used to evaluate corrosion because of the presence of sulphate prior to the corrosion test.

The physical test results suggest that MSI showed higher resistance to sulphate attack compared to the same grade not impregnated (MSN). The reason might be the initial very low apparent porosity (9.7%) and the fact that the sulphate present in its pores acted as a barrier for the reaction between MgO and the sulphur oxide gases. If during operation the temperature rises above 1080 °C and then lowers again, the magnesium sulphate is most likely decomposed, and the impregnation may have no effect on the refractory's sulphur oxide corrosion resistance.

The aluminium sulphate powder in the box was analysed after the first test and the results showed a decrease in the  $\text{SO}_3$  amount from 41% (as received) to 2.9% and the solid compound that was left had about 95%  $\text{Al}_2\text{O}_3$ . This indicates that the reaction according to (3) occurred in the direction of aluminium sulphate decomposition and the amount of  $\text{SO}_2/\text{SO}_3$  produced was enough to react with the refractory components and compare the level of alteration of each recipe after the test.

Although the filling-up of pores by magnesium sulphate does not prove refractory degradation, it indicates the reactivity of each composition when in contact with sulphur oxide gases. Further tests using a larger sample size will be performed in the future to fully validate the proposed technique.

**Figure 8.**

**MKD microstructure: (a) surface after the first test and (b) original.**

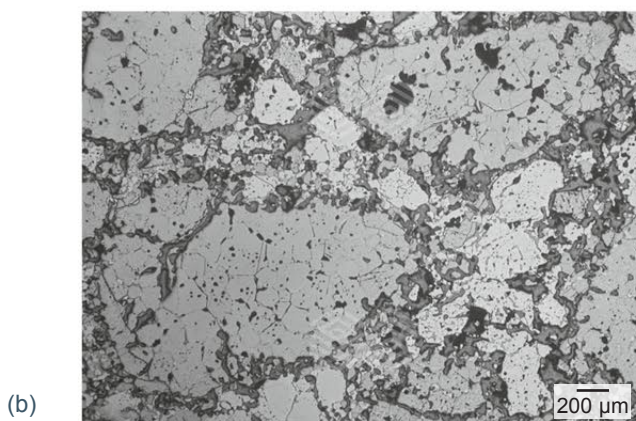
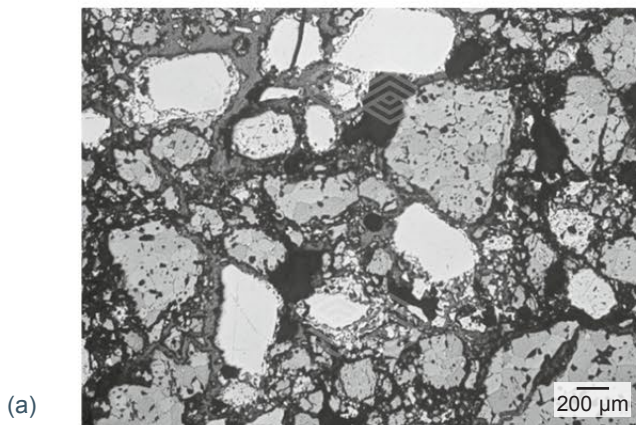
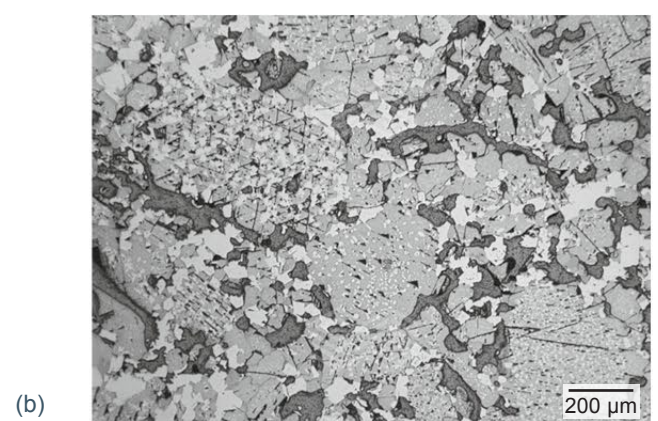
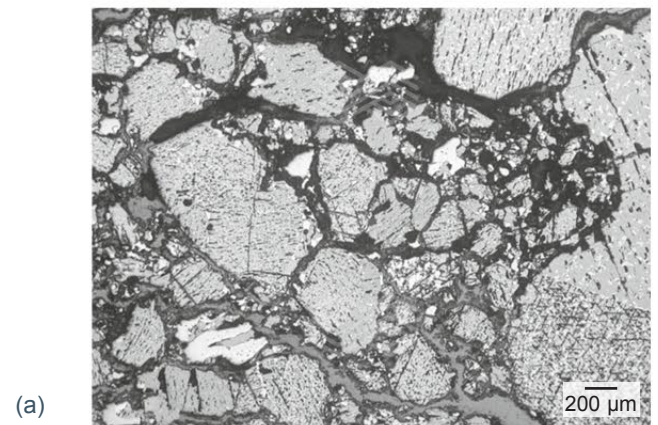


**Figure 9.**

**MKF microstructure: (a) surface after the first test and (b) original.**



## Results/Conclusion

A novel test was developed to evaluate refractory resistance against corrosion by sulphur oxides in a simple and quantitative manner. The two refractory grades based on sintered magnesia showed the lowest resistance against corrosion by sulphur oxides. The grades containing fused magnesia or fused magnesia chromite showed slightly higher resistance. The previous impregnation with magnesium sulphate solution provided improved results when comparing the same brick with and without impregnation. Chromium corundum grades had negligible change in properties after the test, which indicates high corrosion resistance. The alteration observed in the microstructure of the basic brick specimens after the test was similar to images obtained in previous postmortem studies. Thus, the corrosion resistance against sulphur oxides test developed in this study had meaningful results and can be used to compare different refractory bricks regarding this property.

## References

- [1] Malfiet, A., et al. Degradation mechanisms and use of refractory linings in copper production processes: A critical review. *Journal of the European Ceramic Society*. 2014, 34, 3, 849–876.
- [2] Gerle, A., Podwórny, J., Wojsa, J. and Zelik, W. High temperature gaseous corrosion resistance of MgO-containing refractories – A comparative study. *Ceramics International*. 2016, 42, 15805–15810.
- [3] Fotoyi, N. and Eric, R. Interaction of MgO-MgR<sub>2</sub>O<sub>4</sub> (R: Al, Cr, Fe) refractories with SO<sub>2</sub>-containing gases. *Southern African Pyrometallurgy*. 2011, 373–388.
- [4] Fotoyi, N. M.Sc. Thesis, Gas-refractory interactions of basic refractories with sulfur-bearing gases produced in converter furnaces during extraction of platinum group metals in non-ferrous industry. University of the Witwatersrand, Johannesburg, South Africa, 2009.
- [5] Podwórny, J., Piotrowski, J. and Wojsa, J. Investigations into kinetics and mechanism of gas-solid state processes in MgO-MgR<sub>2</sub>O<sub>4</sub> (R: Al, Cr, Fe) spinels-SO<sub>2</sub>-O<sub>2</sub> system. *Ceramics International*. 2008, 34, 1587–1593.
- [6] Pacheco, G. and Fonseca, D. How to deal with alkali infiltration in mag-spinel bricks used in cement rotary kilns? Presented at the 54<sup>th</sup> Annual St. Louis Section / Refractory Ceramics Division Symposium on Refractories, St. Louis, MO, 2018.
- [7] Stern, K. and Weise, E. High Temperature Properties and Decomposition of Inorganic Salts – Part 1: Sulfates. *National Standard Reference Data Series*. Washington DC, 1966.
- [8] Scheidema, M. and Taskinen, P. Decomposition thermodynamics of magnesium sulfate. *Industrial Engineering and Chemical Research*. 2011, 50, 9550–9556.

## Reprint permission

“Development and Applicability of a New Corrosion Test to Quantify Refractory Wear Due to Gaseous Sulphur Oxides Action,” Published in Proceedings of the 58<sup>th</sup> Conference of Metallurgists Hosting Copper 2019. Reprinted with permission of the Canadian Institute of Mining, Metallurgy and Petroleum.

## Authors

Daniela Fonseca, RHI Magnesita, Rotterdam, Netherlands.

Graziella Pacheco, RHI Magnesita, Technology Center, Contagem, Brazil.

Wagner Moulin Silva, RHI Magnesita, Vienna, Austria.

Geraldo Gonçalves, RHI Magnesita, Technology Center, Contagem, Brazil.

Rainer Neuböck, Technology Center, Leoben, Austria.

**Corresponding author:** Daniela Fonseca, [daniela.fonseca@rhimagnesita.com](mailto:daniela.fonseca@rhimagnesita.com)





**Table II.**

Chemical compositions of the synthetic slag after fusion. B2 indicates the CaO/SiO<sub>2</sub> ratio and B3 the CaO/(SiO<sub>2</sub> + Al<sub>2</sub>O<sub>3</sub>). The theoretical saturation (sat.) was calculated using FactSage 7.1.

Slag	FeO	MnO	CaO	Al <sub>2</sub> O <sub>3</sub>	SiO <sub>2</sub>	MgO	B2	B3	MgO sat. theoretical (FactSage)	MgO target slag
	[wt.%]	[wt.%]	[wt.%]	[wt.%]	[wt.%]	[wt.%]			[wt.%]	[wt.%]
Synthetic	20.5	3.5	32.5	34.5	4.3	1.1	7.6	0.8	11	7

The crushed and sieved MgO carriers, with a grain size of 1–1.6 mm, were charged into the molten slag, via a ceramic feeding tube, 20 minutes after the desired temperature in the inner zone of the furnace had been reached to ensure thermal uniformity throughout the furnace. The tube was introduced into the heating zone of the furnace and placed a few centimetres above the crucible.

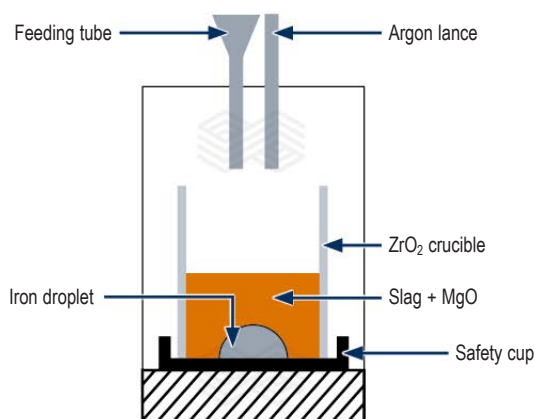
The dissolution test was carried out for a defined holding time, ranging from 10–30 minutes. After the desired dwell time, the crucible with the molten slag was taken out of the furnace and quenched with liquid nitrogen. Subsequently, the sample was cut and polished samples were prepared for microscopic and EDX analysis. The sample cutting and preparations were performed in a water-free environment.

The MgO saturation limit was calculated using FactSage 7.1, to enable the appropriate amounts of MgO-containing raw materials to be determined (see Table II). Since MgO addition above the saturation limit would have led to the precipitation of solid MgO, it was decided to limit the MgO content in the slag to approximately 30 wt.% lower than the calculated saturation value. Additionally, several tests were conducted with a higher amount of MgO than the calculated saturation point to generate an over-saturated slag and enable observation of the undissolved or partly dissolved particles for comparison.

Based on the results of the chemical analyses and MgO concentration in the melt, an assessment of the dissolution behaviour of the MgO-containing raw material was conducted. The mineralogical observations, including the presence of solid MgO particles, provided a further understanding of the dissolution process.

**Figure 2.**

Experimental setup.



## Results and Discussion

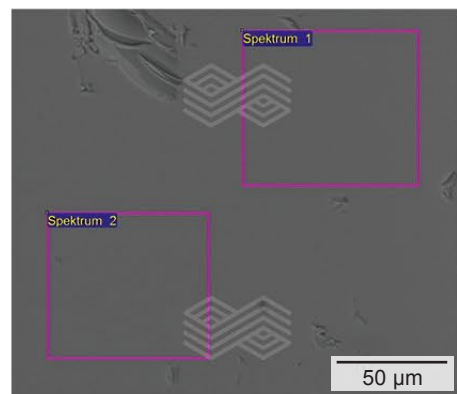
The dissolution behaviour of caustic magnesia and fused magnesia in the synthetic metallurgical slag was compared and the experimental results of these two MgO raw materials are presented below in detail.

A scanning electron micrograph (SEM) of the synthetic slag without any MgO addition is shown in Figure 3, with the areas analysed by EDX indicated. This reference sample enabled the differences between the slag chemical composition before adding the MgO carrier to be compared to the chemistry after the MgO carrier dissolution.

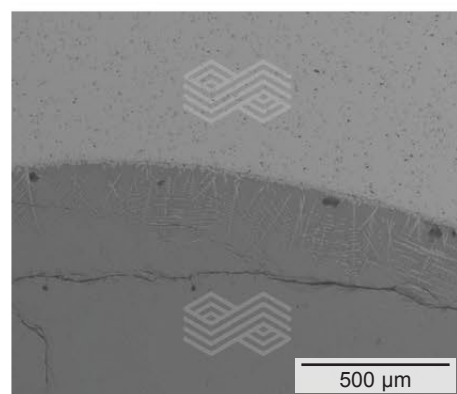
The slag matrix was relatively homogeneous throughout the sample (Figure 3a), apart from in the vicinity of the crucible wall where small CaZrO<sub>3</sub> dendrites had formed due to a reaction between the crucible and slag (Figure 3b).

**Figure 3.**

SEMs of synthetic slag without MgO addition. (a) slag matrix and (b) slag-crucible interface.



(a)



(b)

However, for the detailed analyses of the dissolution behaviour of the MgO-containing raw materials, the zirconium content was neglected. A comparison of results showed small analytical deviations between the XRF and EDX analyses (Table III). The EDX spectra shown represent an average result of all the measurements made. Regarding the synthetic slag, industrial raw materials were used for the preparation and this resulted in an approximately 1 wt.% MgO content in the original slag, mainly stemming from the calcined lime.

**Table III.**

Comparison of EDX and XRF analysis results of the synthetic slag without MgO addition.

Analysing method	MgO [wt.%]	Al <sub>2</sub> O <sub>3</sub> [wt.%]	SiO <sub>2</sub> [wt.%]	CaO [wt.%]	MnO [wt.%]	FeO [wt.%]	Total [wt.%]
EDX	1.0	37.8	5.5	32.7	3.4	19.6	100
XRF	1.1–1.2	34.3–34.7	4.3–4.4	32.5–33.0	3.4–3.7	20.0–20.7	100

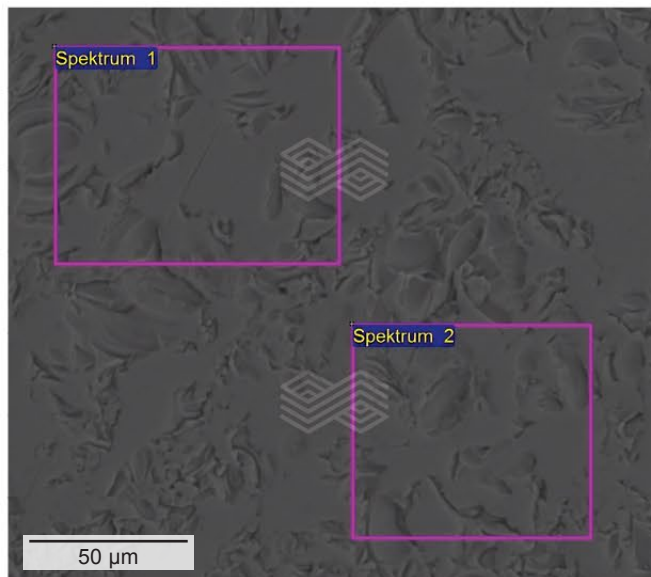
**Table IV.**

EDX analysis results of the synthetic slag heated with caustic magnesia, showing the average results of obtained spectra. Holding time 10 minutes.

Spectra	MgO [wt.%]	Al <sub>2</sub> O <sub>3</sub> [wt.%]	SiO <sub>2</sub> [wt.%]	CaO [wt.%]	MnO [wt.%]	FeO [wt.%]	Sum [wt.%]	Area
Average 1–2	8.4	34.9	5.1	28.2	3.3	20.1	100	Slag

**Figure 4.**

SEM of the synthetic slag heated with caustic magnesia. Holding time 10 minutes.



The results of caustic magnesia dissolution in the synthetic slag are shown in Figure 4. The caustic magnesia was completely dissolved in the slag after only 10 minutes holding time and no MgO particles could be identified in the entire sample in the SEMs. Based on the EDX analysis, the amount of MgO in the melt was as high as 8.4 wt.% (Table IV), which agreed with the target MgO content in the slag of 7 wt.% (Table V) and the MgO originating from the synthetic slag.

**Table V.**

MgO content in the synthetic slag heated with caustic magnesia (average of all EDX results). Holding time 10 minutes.

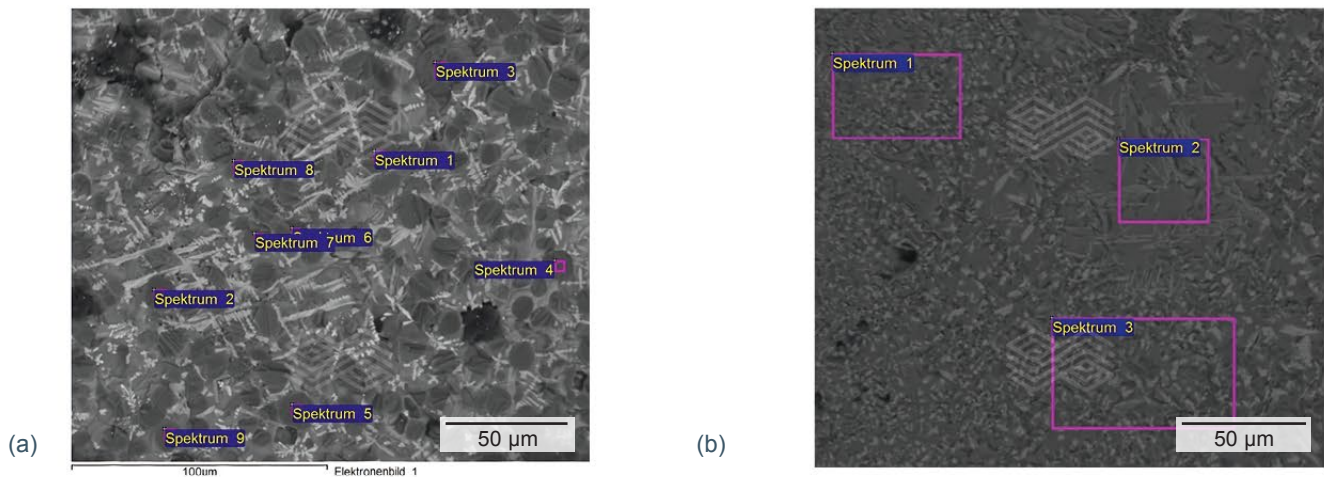
MgO added [wt.%]	MgO slag [wt.%]	MgO Sat. theoretical [wt.%]
7	8	11

To further evaluate the test results, a sample of synthetic slag over-saturated with caustic magnesia was also produced (Figure 5 and Table VI). SEMs showed multiple undissolved round particles were distributed throughout the slag, having a high MgO content (Figure 5a). The average EDX results of multiple undissolved particles (spectrum 1–9) are provided in Table VI. In addition, the slag matrix was examined in detail (Figure 5b). The over-saturated slag structure had obvious differences compared to the slag after the addition of caustic magnesia below the saturation point, namely undissolved MgO particles with some FeO pick up. These results supported the conclusion that the caustic magnesia was fully dissolved after 10 minutes when 7 wt.% was added.

It is also noteworthy that in the over-saturated slag, the maximum average amount of MgO detected by EDX was 17 wt.% (Table VII). This was the result of undissolved periclase particles being present in the majority of the sample and the presence of only a few areas where the periclase was fully dissolved.

**Figure 5.**

SEMs of synthetic slag over-saturated with caustic magnesia. (a) undissolved MgO particles and (b) slag matrix. Holding time 10 minutes.

**Table VI.**

EDX analysis results of the synthetic slag heated with caustic magnesia, showing the average results of obtained spectra. Holding time 10 minutes.

Spectra	MgO [wt.%]	Al <sub>2</sub> O <sub>3</sub> [wt.%]	SiO <sub>2</sub> [wt.%]	CaO [wt.%]	MnO [wt.%]	FeO [wt.%]	Sum [wt.%]	Area
Average 1–9	77.5	9.1	0.9	3.2	1.8	7.5	100	MgO
Average 1–3	16.5	40.5	5.5	24.5	2.0	11.0	100	Slag

**Table VII.**

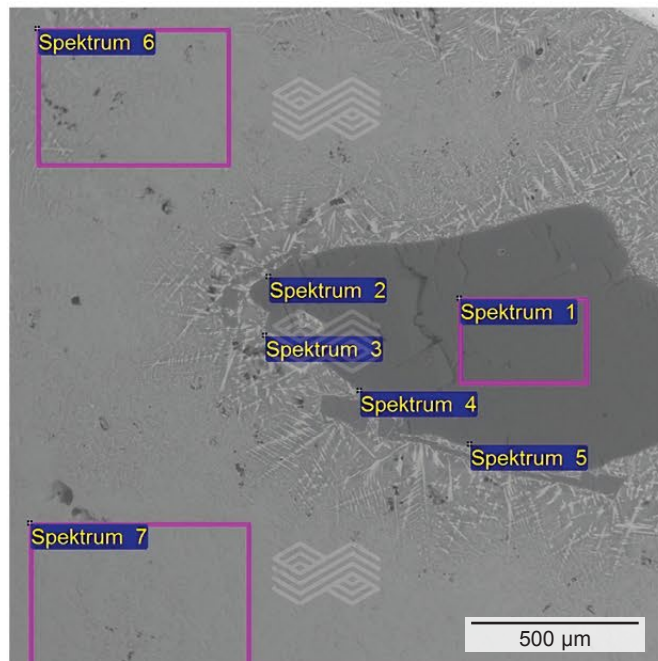
MgO content in the synthetic slag matrix over-saturated with caustic magnesia (average of all EDX results). Holding time 10 minutes.

MgO added [wt.%]	MgO slag [wt.%]	MgO Sat. theoretical [wt.%]
20	17	11

The results of fused magnesia dissolution in the synthetic slag are shown in Figure 6. Due to the refractory behaviour of this raw material, the holding time was extended to 20 minutes. During the post-heating evaluation, multiple fused magnesia particles were identified in the sample. The EDX spectra obtained from a particle indicated a high MgO concentration and a low content of other elements including iron. At steelmaking temperatures, iron oxide (Fe<sup>2+</sup>) reacts rapidly with MgO, forming a magnesiowuestite solid solution phase around the particle, which has a lower melting temperature than the MgO particle and enhances assimilation into the slag.

**Figure 6.**

SEM of synthetic slag heated with fused magnesia. Holding time 20 minutes.



Based on the matrix analysis, the average MgO concentration in the bulk slag did not exceed 4 wt.% (Table VIII), which is lower than the desired MgO content of 7 wt.% (Table IX). Microscopically, it could be clearly seen that the fused magnesia had not dissolved completely within the holding time, although it was 10 minutes longer than in the test with caustic magnesia.

Additional heating tests with sintered magnesia, raw dolomite, and raw magnesite were performed with the synthetic slag and the results are summarized in Table X. In this comparative analysis it was found that caustic magnesia and raw magnesite dissolved completely in the synthetic slag within 10 minutes. In contrast, the fused and sintered MgO-containing materials showed unsatisfactory dissolution performance even after a holding time of 20 minutes. Furthermore, the MgO concentration in the slag samples was significantly lower than desired.

The comparison of raw magnesite and raw dolomite indicated that other effects also play an important role with respect to the dissolution behaviour, namely concurrent CaO dissolution into the slag reduced the MgO solubility from the raw dolomite. In this study the influence of the MgO-carrier particle size on the kinetics of dissolution was not investigated and would be very relevant for the future since it might be expected that the larger sized aggregates, typically used for slag conditioning in steel plants, behave differently as other effects start to become important (e.g., insulating and infiltration behaviour of the highly porous material). Using this novel experimental set up the dissolution of commercially available aggregates can be examined in a wide range of slag types at a microscopic level to determine if undissolved MgO can be identified using EDX, and this would provide more accurate data than using XRF chemical analysis alone.

**Table VIII.**

EDX analysis results of synthetic slag heated with fused magnesia, showing the average results of obtained spectra. Holding time 20 minutes.

Spectra	MgO [wt.%]	Al <sub>2</sub> O <sub>3</sub> [wt.%]	SiO <sub>2</sub> [wt.%]	CaO [wt.%]	MnO [wt.%]	FeO [wt.%]	Sum [wt.%]	Area
Average 1–5	95.9	1.5	0.5	1.3	0.0	0.8	100	Particle
Average 6–7	4.0	9.2	14.7	33.3	4.0	34.8	100	Slag

**Table IX.**

MgO content in synthetic slag heated with fused magnesia (average of all EDX results). Holding time 20 minutes.

MgO added [wt.%]	MgO slag [wt.%]	MgO Sat. theoretical [wt.%]
7	4	11

**Table X.**

Results of dissolution tests with synthetic slag and various MgO-containing raw materials. MgO concentrations in the slag are an average of multiple EDX analyses.

MgO carrier	Holding time [min]	MgO added [wt.%]	MgO slag [wt.%]	MgO Sat. theoretical [wt.%]	Microscopy results
Caustic magnesia	10	7	7	11	Dissolved
Caustic magnesia	20	7	8	11	Dissolved
Caustic magnesia	30	7	9	11	Dissolved
Caustic magnesia	10	20	17	11	Over-saturated
Sintered magnesia	20	7	5	11	Partly dissolved
Fused magnesia	20	7	4	11	Partly dissolved
Raw dolomite	10	7	4	11	Partly dissolved
Raw dolomite	20	7	4	11	Partly dissolved
Raw dolomite	30	7	4	11	Partly dissolved
Raw dolomite	10	20	12	11	Over-saturated
Raw magnesite	10	7	7	11	Dissolved

## Conclusions

This paper describes the dissolution behaviour of different MgO carriers investigated through static laboratory tests at 1600 °C in a high-temperature vertical tube furnace. Polished samples of slags heated with various MgO-containing raw materials were prepared and scanning electron microscopy as well as EDX analysis was used to evaluate the samples. Based on the results of the microscopy and the MgO concentration in the melt, the dissolution behaviour of different MgO carriers was assessed. The results of dissolution tests revealed that compared to the fast dissolution of the caustic MgO sample, fused MgO demonstrated a rather slow dissolution behaviour.

The investigation also showed that to evaluate MgO dissolution approaching the saturation point, the combination of scanning electron microscopy and EDX provides a superior evaluation than XRF analysis alone, since it enables undissolved particles to be identified. However, it must be noted that the laboratory trials were conducted under static test conditions and the dynamics of a real steelmaking process would promote the dissolution behaviour of MgO carriers.

## References

- [1] Pötschke, J. and Routschka, G. Handbook of Refractory Materials. Vulkan Verlag. 2012, ISBN 9783802731624.
- [2] Lopez, F., Souza, P., Garzon, M., Souza de, D. and Dettogne, R. Development and application of a slag model for increasing ladle life at integrated steel mill. *RHI Magnesita Bulletin*. 2018, No. 1, 48–52.
- [3] Pretorius, E. B. and Carlisle, R. C. Foamy slag fundamentals and their practical application to electric furnace steelmaking. 56<sup>th</sup> EAF Conference. 1998, 275–292.
- [4] Pretorius, E. Fundamentals of EAF and ladle slags and ladle refining principles. Baker Refractories.
- [5] Reisinger, P., Preßlinger, H., Hiebler, H. and Zednicek, W. MgO Löslichkeit in Stahlwerksschlacken. *BHM*. 1999, 144, 5, 196–203.
- [6] Reisinger, P. Auswirkungen einer geänderten Schlackenführung auf die Pfannenwirtschaft und die Feuerfestkosten. Doctoral thesis. 1997.
- [7] Deng, T. Study on the dissolution of lime and dolomite in converter slag. Doctoral thesis. Royal Institute of Technology. 2012, 13–42.
- [8] Fruehan, R., Li, Y. and Brabie, L. Dissolution of magnesite and dolomite in simulated EAF slags. ISS Tech Conference. 2003, 799–812.
- [9] Dogan, N., Brooks, G. and Rhamdhani, M. Kinetics of flux dissolution in oxygen steelmaking. *ISIJ Int.*, 2009, No. 49, 1474.
- [10] Deng, T., Gran, J. and Sichen, D. Dissolution of lime in synthetic SiO<sub>2</sub>-FeO-CaO-SiO<sub>2</sub>-FeO slags. *Steel Research Int.*, 2010, No. 81, 347.
- [11] Maruoka, N., Ishikawa, A., Shibata, H. and Kitamura S.-y. Competitive dissolution of MgO from flux and refractory. Proc. of the 12<sup>th</sup> Unified International Technical Conference on Refractories. 2011, CD-ROM.
- [12] Fuxiang, H., Maruoka, N., Ishikawa, A., Jiang, L. and Kitamura, S.-y. Dissolution rates of solid oxides into molten slags. Proc. of the 12<sup>th</sup> Unified International Technical Conference on Refractories. 2013, CD-ROM.
- [13] Umakoshi, M., Mori, K. and Kawai, K. Dissolution rate of burnt dolomite in molten CaO-FeO-SiO<sub>2</sub> slags. *Trans. Iron Steel Inst. Jpn.*, 1984, No. 24, 532.
- [14] Cheremisina, E., Schenk, J., Nocke, L., Paul, A. and Wimmer, G. Influence of magnesium oxide content on kinetics of lime dissolution in steelmaking slags. *ISIJ Int.*, 2016, No. 57, 304–313.
- [15] Cheremisina, E., Schenk, J., Viertauer, A., Nilica, R. and Roessler, R. Internal report MgO dissolution project I. 2017, 8–34.
- [16] Cheremisina, E., Schenk, J., Viertauer, A., Nilica, R. and Roessler, R. Dissolution rate of various MgO materials in steel and secondary metallurgy slags. AISTech conference proceedings. 2018, 1103–1115.
- [17] Cheremisina, E. Dissolution kinetics of CaO and MgO in steelmaking slags. Doctoral thesis. Montanuniversität Leoben. 2016.
- [18] Cheremisina, E., Schenk, J., Nocke, L., Paul, A. and Wimmer, G. Kinetics and mechanisms of dolime dissolution in steelmaking slag. *Metall. Mater. Trans. B*. 2019, 50. No. 3, 1269–1276.

## Authors

Elizaveta Cheremisina, K1-MET, Leoben, Austria.

Johannes Schenk, Montanuniversität Leoben, Austria.

Andreas Viertauer, RHI Magnesita, Vienna, Austria.

Roland Nilica, RHI Magnesita, Technology Center, Leoben, Austria.

Roman Rössler, voestalpine Stahl, Linz, Austria.

**Corresponding author:** Elizaveta Cheremisina, Elizaveta.cheremisina@k1-met.com



Bernd Lorenzoni

# Bulk Density Determination of Granular Refractory Materials

## Introduction

Bulk density is an important parameter of granular raw materials that are used to produce refractory products. This article is focused on the measuring methods used to determine the bulk density of these materials. The advantages and disadvantages of typically used standard methods are discussed, and a new measurement technique with the potential to overcome the drawbacks of the established methods is introduced.

## Definition of Granular Material Bulk Density

For the production of refractory products, it is important to use raw materials with an accurately determined bulk density to achieve the desired physical properties. For example, the thermal conductivity of a product can be influenced by choosing raw materials with different bulk densities. Generally, bulk density ( $\rho_b$ ) is defined as the ratio of the mass of a dry porous material ( $m$ ) to its bulk volume ( $V_b$ ), often expressed in grams per cubic centimetre or kilograms per cubic metre [1]:

$$\rho_b = \frac{m}{V_b} \quad (1)$$

Therefore, independent of the chosen measuring method, the mass of the dried grains and their bulk volume must be determined. The bulk volume is defined as the sum of the volumes of the solid material, the open pores, and the closed pores in a porous body [1]. The importance of this definition will become apparent later in the article.

## Standardized Methods to Measure Grain Bulk Density

In general, the material for the measurements should have a grain size between 2 mm and 6.7 mm, with minor deviations depending on the specific method. Any dust or loose particles adhering to the grains must be removed by washing or, with materials sensitive to water, by air blowing. In addition, the material needs to be completely dried before starting the test. The sample weight ranges from 50–200 g. While all the methods have in common that the first measuring step is to weigh the dried sample, either to the nearest 0.1 g or 0.01 g, subsequent determination of the volume is performed in quite different ways. The most important technical details to understand the principles of the different measurement methods described in established standards are explained in the following sections.

## DIN EN 993-17

The DIN EN 993-17 standard recommends a test sample mass of 100 g for homogeneous materials and the test sample is weighed to the nearest 0.1 g on an analytical balance [2]. To determine the bulk volume of the test sample, a vacuum pycnometer is used. The sample is transferred into the pycnometer, which is then filled with mercury (Hg) while a vacuum is applied. When performed according to the description in the standard, this results in an average pressure on the grains of about 26.5 kPa. The bulk volume of the test sample can be calculated by equation 2:

$$V_b = \frac{m_G + m_p - m_T}{\rho} \quad (2)$$

Where  $m_G$  is the mass of the pycnometer filled with mercury,  $m_p$  is the mass of the test sample,  $m_T$  is the mass of the pycnometer filled with mercury and the test sample, and  $\rho$  is the density of mercury at the measurement temperature. If the room temperature varies by more than 2 °C during the measurements, this must also be taken into consideration.

As with all the following standards, having determined the  $V_b$ , the bulk density can be calculated using a formula equivalent to the defined equation 1.

## DIN EN 993-18

For measurements according to DIN 993-18 at least triplicate samples should be tested, each with a recommended mass of approximately 200 g (this can be reduced to approximately 100 g for homogeneous samples) [3]. These samples are weighed to the nearest 0.01 g on an analytical balance. The first step for the bulk volume measurement is sample impregnation; therefore, the samples are placed in crucibles in an air-tight vessel. The vessel is then evacuated until a pressure of not more than 2.5 kPa has been reached. This vacuum must be maintained for at least 15 minutes before water is progressively introduced into the vessel so that after approximately 3 minutes the grains are covered by about 20 mm. The reduced pressure is then maintained for 30 minutes. Subsequently, the vessel is opened and the grains are transferred into a crucible suspended by a thin thread from the balance load pan suspension point and weighed while completely immersed in water. The test sample is then placed on a wet cotton towel, blotted until the wet sheen on the grains has been removed, and then reweighed.

The procedure described in this standard can be simplified by taring the balance at certain points. The bulk volume of the grains is given by equation 3:

$$V_b = \frac{m_a - m_i}{\rho} \quad (3)$$

Where  $m_a$  is the apparent mass of the immersed sample,  $m_i$  is the mass of the impregnated sample, and  $\rho$  is the true density of water at the test temperature.

### ISO 8840

Two methods are described in ISO 8840 [4]. One is similar to the mercury method in DIN EN 993-17 and the second is called the arrested water absorption method where the weighed test sample is placed in a beaker and then covered with water for at least 2 minutes. A 100 ml burette is also filled with water to a level between the 20–25 ml marks. A cotton towel is saturated with water and then wrung out by hand. The test sample is transferred to the towel and blotted with the towel until the wet sheen on the grains has disappeared. The grains are then poured into the burette and the final level is used to determine the bulk volume of the grains.

### ABNT NBR 8592

The ABNT NBR 8592 standard also describes two methods to measure grain bulk density for a grain size defined as between 2–4 mm [5]. For the first method, the sample weight should be approximately 50 g and the impregnation step is performed by boiling the grains in water for 5 minutes, or if the material is sensitive to water, kerosene is used. After cooling the sample down to room temperature, the grains are placed on a wet towel and the excess liquid is removed by blotting the sample. Then the sample is transferred into a burette filled with water, or kerosene, and the amount of displaced liquid corresponds to the bulk volume of the sample. For the second method, a 60–90 g sample is recommended. After measuring the dry weight, the grains are also boiled for 5 minutes to impregnate them and after cooling, the excess liquid is removed by blotting. However, the subsequent steps of the procedure are very similar to the those described in DIN EN 993-18 [3].

### ASTM C357

The main difference between ASTM C357 and the aforementioned arrested water absorption method is that the grains are impregnated by boiling them for 1 hour while completely covered with water [6]. In addition, the burette is smaller (i.e., 50 ml) and a Le Chatelier Specific Gravity Bottle can also be used.

### Reasons for Differing Results

There are several factors that can affect the outcome of grain bulk density measurements. For example, the room temperature should not change too much or be out of certain ranges during the measuring process, otherwise it must be considered in the calculation. Furthermore, the grain size distribution influences the outcome of the measurements because when grains are fractured, formerly closed pores can be opened that then fill with liquid during the impregnation process. Generally, the different methods to impregnate the grains can lead to differing results.

Beginning in 2018, many of the aforementioned methods were tested at the RHI Magnesita's Technology Center Leoben (Austria). During this evaluation it became apparent that the most influencing factor, regarding the repeatability and reproducibility, was the measuring step for the grain volume, not only for different methods, but also when different operators were using the same method. Most of the methods include a process step where excess water is removed from the surface of the grains by blotting; however, there is no precise way to define how wet the towel should be for this step. Additionally, the decision when the wet sheen of the grains is removed is subjective and differs from operator to operator. If liquid is left on the surface, a higher volume is measured and so the grain bulk density appears lower. If the liquid on the surface is removed well, more liquid can be sucked out of the open pores, thereby the volume seems to be smaller and so a higher grain bulk density is calculated.

In addition to these practical problems there is also a theoretical consideration. According to ISO 5017 [1], the bulk volume is defined as the sum of the volumes of the solid material, the open pores, and the closed pores in a porous body, but the roughness of the surface limits the accuracy of this definition and, as a result, that of the bulk density. Furthermore, the concept of bulk density becomes less precise when the sample volume diminishes below certain limits or when its texture (i.e., size of the pores and grains) is too coarse [1]. The consequence of this definition problem is simple but has a severe impact, namely that an absolute value for bulk density does not exist and the results gained using different methods are always relative. However, it is also important to mention that within one method these relative values are nevertheless useful as long as the measurement uncertainty is not too large.

## Advantage and Disadvantage of the Hg Method

The main advantage of the mercury method is that it does not include a subjective step, like the other methods described in this article, because the grain volume is determined by the amount of mercury displaced by the grains at a defined pressure. This is probably the prime reason for the good repeatability and reproducibility of this method. While it doesn't automatically mean that this method provides the "true value", as surface structure and pores also affect the outcome of the measurements, it is reasonable to say that as long as the mercury pressure is always kept at the same level, the influences can be considered "constant". However, the overwhelming disadvantage of this method is the mercury itself, since it is a critical substance regarding health and safety and in the near future its use might be prohibited in an increasing number of countries.

## The Centrifuge Method

During investigation of the different methods in Leoben, it became obvious that all the evaluated standard methods had significant drawbacks. On the one hand, the operator influence on the outcome was not negligible, and on the other hand, a critical substance had to be used. Therefore, a development project was started to find a better way to measure the bulk density of granular materials. Based on the experiences with the other methods, eight main targets for a new method were defined:

- Repeatability and reproducibility within the range of the Hg method.
- Minimize operator influence on the result.
- Easy operation and robust setup.
- Comparable results to those gained with other methods.
- Affordable equipment.
- Time required for measurement within a reasonable range.
- Fulfil general requirements for standardization.
- Customer acceptance.

The starting point for the new development was the method described in DIN EN 993-18. Additionally, at RHI Magnesita's Drogheda plant (Ireland), a promising way to remove the excess surface water from grains had been developed and implemented, namely the use of a centrifuge instead of a wet towel.

## References

- [1] ISO 5017:1998 Dense shaped refractory products – Determination of bulk density, apparent porosity and true porosity.
- [2] DIN EN 993-17:1998 Determination of bulk density of granular materials by the mercury method with vacuum.
- [3] DIN EN 993-18:2002 Determination of bulk density of granular materials by the water method with vacuum.
- [4] ISO 8840:1987 Refractory materials – Determination of bulk density of granular materials.
- [5] ABNT NBR 8592:2012 Dense granulated refractory materials – Determination of bulk density, water absorption and apparent porosity.
- [6] ASTM C357 – 07 Standard Test Method for Bulk Density of Granular Refractory Materials.

## Author

Bernd Lorenzoni, RHI Magnesita GmbH, Technology Center, Leoben, Austria.  
**Corresponding author:** Bernd Lorenzoni, bernd.lorenzoni@rhimagnesita.com

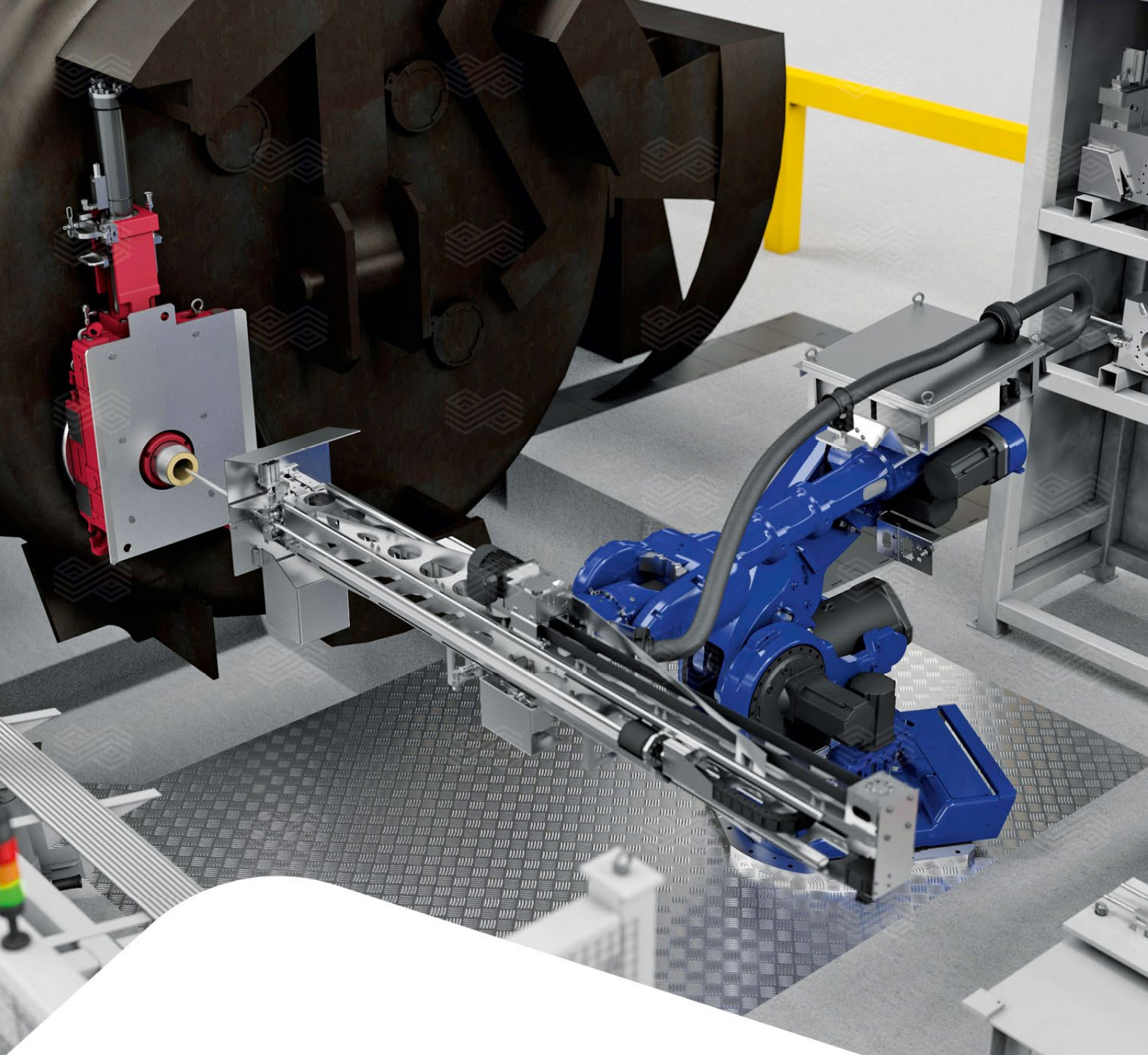
Based on the Drogheda device, an improved centrifuge was designed and constructed in Leoben (Figure 1) and the advantages became immediately evident. Tests with different refractory raw materials showed that the repeatability for all tested materials was at the same level as the mercury method. Furthermore, as the spinning parameters (i.e., time and speed) are kept constant and controlled electronically, the operator influence during the "drying step" is almost completely excluded. This also makes performing the test easier for the operator. In addition, the time required for the measurement is less than the time required for the DIN EN 993-18 standard procedure.

## Outlook

To date, the centrifuge method is looking very promising. Several devices have already been built and sent to different plants within the RHI Magnesita Group and external partners for further testing. Investigations regarding the optimal spinning parameters that should ultimately be used are still ongoing and for this reason no actual measurement results have been included in this article. The implementation process for including this novel centrifuge method in DIN EN 993-18 has already been initiated.

**Figure 1.**  
 Prototype centrifuge built at the Technology Center Leoben.





## Tailor-made ladle-to-mould solutions INTERSTOP Robotics

In order to make steel production safe and economical while maintaining the highest quality standards, we provide our customers with a modular scope of supply, focusing on the core business of systems technology.

For ladle gate systems, INTERSTOP offers solutions in the ladle preparation area and on the CCM floor that allow for manual and robotic operation. The full package contains the latest slide gate technology, fully equipped with casting cylinder and media coupling, all being operated by customized robotic systems.

Curious to find out more details?  
Visit [rhimagnesia.com/interstop/automation-robotic](https://rhimagnesia.com/interstop/automation-robotic)

Follow us



# bulletin

2020

**Copyright notice:**

The texts, photographs and graphic design contained in this publication are protected by copyright. Unless indicated otherwise, the related rights of use, especially the rights of reproduction, dissemination, provision and editing, are held exclusively by RHI Magnesita N.V. Usage of this publication shall only be permitted for personal information purposes. Any type of use going beyond that, especially reproduction, editing, other usage or commercial use is subject to explicit prior written approval by RHI Magnesita N.V.

